A Thesis

on

Development of a Novel Computational Framework for Non-Newtonian Fluid Flows with Applications to Hemodynamics

submitted in partial fulfillment of the requirements for the degree of

Doctor of Philosophy

by

Mantulal Basumatary

Department of Mechanical Engineering
Indian Institute of Technology Guwahati
Guwahati - 781039, Assam, India
June, 2019

"*Nothing in life is to be feared, it is only to be understood. Now is the time to understand more, so that we may fear less.*"

– Marie Curie

Certificate

This is to certify that **Mr. Mantulal Basumatary**, a Ph.D student in the Department of Mechanical Engineering, Indian Institute of Technology Guwahati, has completed the thesis entitled "**Development of a Novel Computational Framework for Non-Newtonian Fluid Flows with Applications to Hemodynamics**" under our supervision. To the best of our knowledge the work carried out has not been submitted elsewhere for the award of a Ph.D degree. We wish him all the best for his future endeavours.

Dr. Ganesh Natarajan Date:

Associate Professor

Department of Mechanical Engineering

Indian Institute of Technology Guwahati

Guwahati, Assam, Pin - 781039, India

Dr. Vinayak Kulkarni Date:

Associate Professor

Department of Mechanical Engineering

Indian Institute of Technology Guwahati

Guwahati, Assam, Pin - 781039, India

Acknowledgements

First of all, thanks to God for giving me patience and energy through the journey of thesis work.

I would like to thank my supervisors Dr. Ganesh Natarajan, Dr. Vinayak Kulkarni and late Dr. Subhash C. Mishra for their invaluable guidance, help and patience throughout the process of writing this thesis. In particular, I admire the way, Dr. Ganesh Natarajan try to inculcate research skills in me and my colleagues by asking genuine questions and useful discussions.

I am highly thankful to my doctoral committee members: Dr. S. Kanagaraj, Dr. Vinayak Kulkarni and Dr. Vibin Ramakrishnan for their important comments, suggestions and encouragement in carrying out the research work. I am also thankful to the head of the department Dr. Santosha K. Dwivedy, other faculties, officers and staff in the department for their direct and indirect help.

I would like to thank Mr. Suresh Sahu for productive discussions and assistance with the implementation of the non-Newtonian models in the present computational framework. I am also thankful to my labmates and other colleagues as well for their selfless cooperation and motivation.

I am very thankful to the financial support from Ministry of Human Resources and Development and the institute for providing conducive environment to carry out the research, without which this work would not have been possible.

Last but not least, I am highly grateful to my family members for their support and encouragement throughout the course of research work.

Mantulal

Abstract

This thesis is devoted to the development of a novel finite volume flow solver for incompressible non-Newtonian fluid flows and it application to hemodynamics. The study of flow of blood through blood vessels with constrictions and/or expansions using simulations necessitate the use of unstructured meshes owing to the complex geometries involved where one also has to account for the non-linear dependence of viscosity on strain rate. Towards this objective, we present a new framework referred to as the hybrid staggered/non-staggered framework for incompressible flows. We incorporate both power-law and five-parameter Carreau family of models in the framework, the latter with a view to simulate blood flows. This framework combines ideas from staggered and collocated finite volume approaches and solves for the normal velocities at the faces and for the pressure at the cell centers. Consequently, one obtains a unique framework that inherits the advantages of both frameworks and results in a flow solver that satisfies the discrete incompressibility constraint at all times (without any special treatment) which is easily implemented even on unstructured meshes. The latter advantage stems from the collocated-like treatment of the convective and viscous fluxes although the momentum equation is solved for the normal velocity at the cell faces. Consequently, a critical aspect of this framework is an accurate and efficient strategy to reconstruct the cell-center velocities from the scalar face-normal velocity. We show that a simple vector interpolation based on Green-Gauss theorem is first order accurate for centroidal velocities on unstructured meshes and leads to non-physical solutions. The root cause of spurious numerical solutions is identified to be the inconsistent viscous fluxes and we show that merely refining the mesh does

not mitigate this error. This pertinent problem is resolved by proposing an iterative defect correction strategy which allows the velocities and gradients to be reconstructed to second and first order accuracy respectively. We numerically demonstrate that the use of this strategy is essential to ensure accurate numerical solutions of non-Newtonian flows using the proposed hybrid staggered/non-staggered framework. The framework is shown to be nominally second order accurate both in space and time on arbitrary polygonal meshes and also conserves both mass and momentum discretely on any mesh topology. The numerical framework is thoroughly validated using a number of canonical test problems involving steady and unsteady flows to highlight its versatility and applicability on unstructured grids. This framework is applied to understand the hemodynamics in stenoses and aneurysms with a view to relate flow parameters with clinical parameters and to gain insight into the role of non-Newtonian behaviour on the flow dynamics. Investigations are performed for steady and unsteady flows in idealised double stenoses and aneurysm geometries for physiological Reynolds numbers assuming the flow to be in a laminar regime and the walls to be rigid. Different models of the Carreau family are found to predict the peak wall shear stress (WSS) differently in the case of double stenoses with the Carreau-Yasuda model computing a higher peak WSS in steady flows. It is found that as the constriction ratio increases, the peak WSS increases as well. For the aneurysm geometry, the Newtonian model is seen to predict a higher WSS compared to the non-Newtonian fluid models at the dome region although the shear-thinning power-law fluid exhibits the highest WSS at the neck region. For a given fluid model, increase in aneurysm size was found to lead to increase in WSS at the neck accompanied by a reduction in WSS in the dome. In order to mimic the realistic flow scenarios, unsteady simulations were carried out using pulsatile inlet velocity profiles for both stenoses and aneurysm geometries where the oscillating shear index (OSI) is reported. It is observed that the OSI is relatively quiet low in regions of peak WSS_{mean} at the constricted regions over a period for all the fluid models. A cavity-like flow was observed for the aneurysm geometry at low pulsatility index while for higher pulsatility index showed flow entrainment from parent artery into

the aneurysm dome at different instants of a cycle. In both steady and unsteady simulations, it was observed that the change in constriction ratio (for stenoses) and size (for aneurysms) had a greater impact on the flow dynamics for a given non-Newtonian fluid model. The results from these studies provide insights into the flow dynamics and must be regarded as a first step towards development of an indigenous virtual laboratory for computational hemodynamics that can help devise patient-specific treatment strategies in the future when the framework is extended to three-dimensional flows with fluid-structure interaction.

Contents

List of Figures

List of Tables

Dedicated to my supervisor late Dr. Subhash C. Mishra

Chapter 1

Introduction

Several flow scenarios in practice, both natural and industrial, involve incompressible non-Newtonian flows in complex geometries. Basically, these are fluid flows where the correlation between viscous stress and rate of strain is non-linear in antithesis to the Newtonian fluid. Examples of fluids exhibiting non-Newtonian behaviour are milk, starch, honey, blood and paint and among others. The flow of blood through human arteries is a classical scenario of non-Newtonian incompressible flow through complex geometries and carrying out experimental studies in such scenarios is not viable. The complex and non-linear nature of governing equations for these flows also mean that analytical solutions are not possible either which leaves numerical approaches as the only viable solution approach. The advent of computing techniques over the last forty years has led to emergence of the field of computational fluid dynamics (CFD) that offers a feasible route to investigate and understand complex flow scenarios.

Hemodynamics is the study of blood flow through blood vessels and understanding this in diseased blood vessels could allow correlating flow parameters (obtained from simulations) with clinical parameters that could enable patient-specific treatment. Simulations in hemodynamics therefore necessitate a robust computational framework that can account for the non-linear viscosity dependence pertaining to non-Newtonian fluids and a suitable choice of mathematical models that can accurately model the viscosity variation with strain rates. In the present work, we adopt the finite volume method as the backbone to develop a non-Newtonian flow solver owing to its ability to discretely

conserve mass and momentum while also accommodating unstructured meshes that are necessitated by the complex geometries through which the flow takes place. In the sections to follow, we therefore provide an overview of literature that relate to computational frameworks for incompressible flows with an emphasis on unstructured finite volume methods applied to non-Newtonian fluid flows.

1.1 Non-Newtonian model

A Newtonian model is used to describe a fluid when the slope (see Figure 1.1) remains constant (linear) of a shear stress versus shear rate plot that passes through origin. Blood flows in the region of high shear rate like in aorta (large artery) can be modelled with Newtonian model [1]. On the other hand, if the viscosity is not constant or non-linear then the fluid is modelled using non-Newtonian model. It is well known fact that blood consists of ions, cells, nutrients, platelets that are suspended in plasma and is definitely a non-Newtonian fluid. In the present work, we limit ourselves to the non-Newtonian models where the shear stress varies only with current value of the shear rate (generalised Newtonian fluid) and does not depend on the history of shearing. To

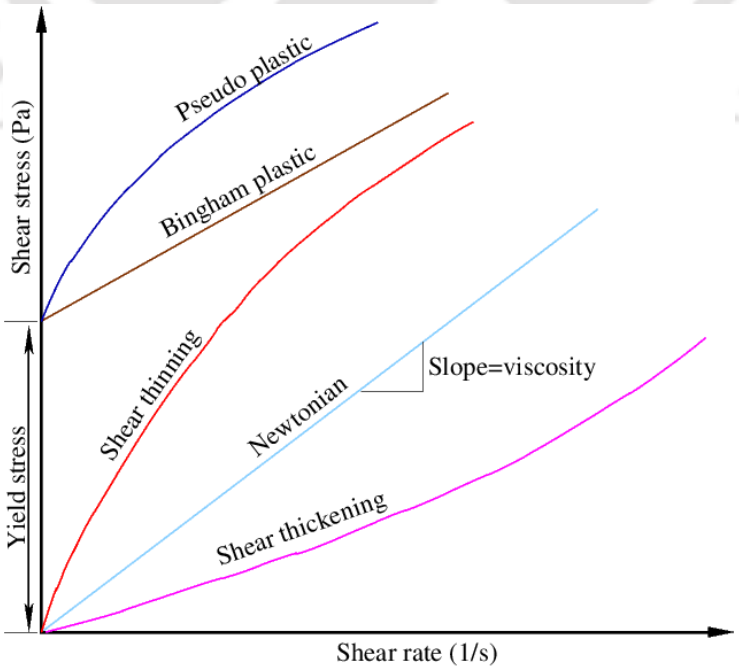

Figure 1.1: Schematic of viscosity variation for different fluid models.

date, there is no universally accepted fluid models to represent the rheology of blood [1]. Nonetheless, Carreau family and shear-thinning power-law are popularly used to model the non-Newtonian behaviour of blood [2–7].

1.2 Numerical approaches for non-Newtonian flows

Despite of the significance of unstructured staggered mesh finite volume framework in the incompressible flow regime, it is rarely exploited for non-Newtonian flows. Generation of structured mesh is cumbersome in complicated domains. Structured mesh/cell (see Figure 1.2(a)) has equal edges (in two-dimension) and one can find the support cells easily to a known cell from the perspective of data storage in a CFD code, which is not the case in unstructured cell as shown in Figure 1.2(b). Unstructured meshes are the natural option for simulations in complex geometries owing to its inherent ability to refine locally and mesh adaptation. A staggered framework on structured meshes

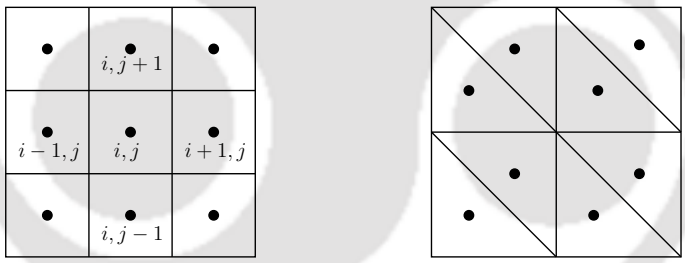

(a) Structured cell (b) Unstructured cell

Figure 1.2: Different mesh layouts: (a) structured and (b) unstructured.

for the simulations of viscoelastic flows is described in [8] where constitutive relation is discretised using a third-order upwind scheme. For the steady flow of aforementioned fluid, Oleveira et al. [9] have presented a finite volume method based numerical solver with non-staggered arrangement of variables those are solved in a segregated manner on non-orthogonal (curvilinear) meshes and it is extended to unsteady flows in [10]. In addition, implementation of generalised Newtonian fluids in the computational framework of [9] can be found in [11] for steady as well as unsteady flows in a planar T-junction. A third order upwind finite volume method based on collocated positioning

of solution variables to avoid the diffusive effects of first order schemes is developed in [12] for the above-mentioned fluids. Steady and unsteady flow across a backward facing step, a representative of stenosis (constriction of an artery) are investigated in [13] using Carreau fluid to model blood flow. In their numerical simulations, the governing equations are solved using commercial CFD package FLUENT (finite volume method with non-staggered mesh). This package has been utilized by Chhabra and co-workers [14–17] to study steady non-Newtonian flows over circular, elliptical, triangular and square cylinders. Nejat et al. [18] develop a second order accurate structured collocated finite volume framework for the non-Newtonian power-law flows using pseudo-compressibility technique. The solution variables are solved implicitly in the coupled manner and its unstructured version can be found in [7] for the generalised Newtonian fluids.

1.3 Collocated versus staggered mesh framework

Non-staggered framework is the most common choice for unstructured meshes among several researchers due to its easier implementation as opposed to its staggered counterpart [19–22]. An issue encountered in collocated positioning of solution variables is that in the incompressible flows it does not satisfy discrete mass conservation exactly. This error in mass conservation is because of added numerical dissipation that leads to decoupling of flow fields. The difficulty of decoupling can be circumvented using the idea of Rhie-Chow [23] interpolation where divergence of velocity field become proportional to fourth derivative of pressure gradient. Nevertheless, it could become prominent in flows associated with high pressure gradients; typical examples are the blood flows through complex geometries aneurysm and stenosis where there are sudden expansion and contraction respectively. It is well known that blood is an incompressible and non-Newtonian fluid whence the correlation between viscous stress and strain rate is non-linear in antithesis to the Newtonian fluid [1–3, 24–26]. Therefore, a robust computational framework is necessitated to solve this class of flows efficiently

while guaranteeing a least error in the discrete mass conservation. Furthermore, it would be difficult to obtain detailed information of flow parameters using experimental investigations of these flows.

Staggered frameworks originally developed by Harlow and Welch [27] are the best option for ensuring mass conservation in the incompressible flow regime. Nevertheless, they are cursed by the pitfalls in implementation due to allocation of solution variables at separate positions and the numerical accuracy connected to the solution techniques. Besides, difficulties could become substantial in non-Newtonian flows whence the viscosity varies with strain rate. In addition, in the curvilinear staggered meshes (applicable to complex geometries) requires transformation of variables that needs discretisation of the Christoffel symbols which is computationally expensive [28, 29]. A first order accurate finite volume method spatial discretisation on unstructured triangular cells is presented by Rida et al. [30] while the velocity and pressure fields are located at the side centers and cell centroid respectively of a triangle. In contrast to [30], Perot and coworkers have developed a staggered unstructured mesh framework where the scalar variable is stored at the cell circumcenters while the vector quantities are placed at the face center [31–33]. This method is only first-order accurate in unstructured meshes, but it is second order in regular meshes. Furthermore, a first order accurate spatial discretisation on unstructured cells is presented in [34, 35] for incompressible as well as compressible flows while the components of the normal momentum are positioned at the center of faces and pressure is stored at the cell centroids. Shashkov et al. [36] discuss development of higher-order staggered framework on non-uniform quadrilateral meshes and propose a polynomial reconstruction approach, which has been extended to triangular grids by Vidović et al. [37–39].

Discretisation of the Navier-Stokes equations on non-staggered grids require information from fictitious nodes outside the computational domain [9]. A hybrid staggered/ non-staggered mesh approach alleviates the drawbacks of non-staggered and staggered meshes by combining the versatility and ease of implementation of a non-staggered framework with the accuracy of a staggered framework [40]. Natarajan and

Sotiropoulos [41] have demonstrated that the lower order accurate numerical schemes on unstructured meshes in the aforementioned numerical framework result in non-physical solutions particularly in the regions with flow separation. The hybrid staggered/ non-staggered framework facilitates the implementation of boundary conditions in flows with complex boundaries in addition to balanced force calculations in the incompressible multiphase flows [42]. Ge et al. [43] have successfully employed the above-mentioned approach with Cartesian and curvilinear meshes for incompressible Newtonian flows using immersed boundary method and an extension to unstructured Cartesian meshes can be found in [44].

1.4 Applications to hemodynamics

Hemodynamics is the study of blood flow in the cardiovascular network. It is important to have better insight of the hemodynamics of stenosis and aneurysm geometries because they are one of the leading cause of human death around the world. A stenosis refers to the abnormal narrowing of blood vessel while an aneurysm may be described as anomalous bulging of it. In-vivo patient specific investigations of such problems are not often possible and one needs to take help of numerical frameworks for better understanding and subsequent recommendations for clinical interventions [45]. Furthermore, it is viable to obtain practical data with the advent of modern medical imaging techniques to get patient-specific geometry required for numerical simulation [46]. It has been reported in [47] that wall shear stress is a clinically important parameter that can provide clue relating to the growth and blockage or rupture of the aforementioned conditions of the cardiovascular system to a medical practitioner. In addition, oscillating shear index (OSI) defined by He and Ku [48] can provide information about the nature of flow (steady or unsteady) relating to focal locations of atheroma in aneurysm and stenosis. Influence of aneurysm and stenosis on flow waveform along with the non-Newtonian behaviour of blood has been mentioned in [49]. Steady hemodynamics of double stenoses has been investigated numerically by Wei et al. [5] using Newtonian

and non-Newtonian (power-law) models. Their results show that there are marked difference between the Newtonian and non-Newtonian models. Similar type of problem in three-dimension has been studied in [6, 50] using Carreau-Yasuda and Newtonian models and have demonstrated the necessity of describing the blood rheology in a more accurate way. Three-dimensional investigations of hemodynamics in stenosis in [51] have indicated that increase in the constriction ratio lead to rise in pressure drop. Nandakumar et al. [52] investigated numerically the steady as well as pulsatile flow of a shear-thinning and Newtonian model for blood through a two-dimensional axisymmetric stenosed channel. Their results have indicated that in steady flow the shear-thinning fluid model has predicted higher peak wall shear stress than Newtonian model. The aforementioned problem has been extended to study blood flow through double stenosis in [53] where they found that peak wall shear stress increases with the length and gap of the stenosis. It has been reported in [47] that Newtonian modelling of blood results in overestimation of wall shear stress inside the aneurysm dome wall. Low wall shear stress on the aneurysm wall indicates a higher chance of growth and rupture of an intracranial aneurysm has been stated in [54–57]. It has been described in [55] the above flow parameter decreases with the increase in aneurysm size. Le et al. [58] has investigated numerically the role of pulsatile flow on the hemodynamics of intracranial aneurysms with low and high pulsatility index. They have reported a cavity-like flow in the dome for low pulsatility flows while at higher pulsatility index, a vortex ring formation inside the aneurysm.

1.5 Aims of the thesis

In light of the literature review carried out, the broad objective of this research is to develop a generic and robust unstructured staggered mesh framework for non-Newtonian flows with application to hemodynamics. The sub-objectives of this research work are detailed below.

1. Development of a novel hybrid staggered/non-staggered framework for incom-

pressible non-Newtonian flows. This framework is a combination of both collocated and staggered frameworks and envisages to combine the merits of both approaches thereby allowing for a robust framework to handle non-Newtonian flows.

2. Devising a novel reconstruction approach to obtain cell-centered velocities from scalar face-normal velocities required for this novel framework using the Green-Gauss method. The necessity of such an approach for incompressible flows in general and non-Newtonian flows in particular will be studied.

3. Comprehensive validation of the computational framework with different non-Newtonian models for canonical problems to assess its accuracy and viability on structured and unstructured meshes.

4. Application of the framework to investigate steady hemodynamics in idealised stenoses and aneurysms to understand the role of different models on wall shear stress and flow dynamics.

5. Application of the framework to understand unsteady non-Newtonian flows through these geometries and the role of pulsatility on the flow characteristics, with aim of relating the flow parameters to clinical indices.

1.6 Organisation of the thesis

The remainder of the thesis is organized as follows. Chapter 2 describes governing equations and their discretisation in the finite volume framework. Chapter 3 presents the formulation of the velocity reconstruction approach while the validations studies using the newly proposed flow solver are described in Chapter 4. Chapters 5 and 6 discuss the application of the framework to steady and unsteady hemodynamics respectively. Chapter 7 summarises the findings from the studies and provides few directions for future research.

Chapter 2

Governing equations and mathematical formulation

In this chapter, we describe the detailed mathematical formulation of the incompressible non-Newtonian fluid flow solver based on the hybrid staggered/non-staggered framework. The specifics of discretisation of the convective and viscous fluxes are also discussed and an overview of the implementation of the boundary conditions is provided.

2.1 Background

The Navier-Stokes equations constitute the governing equations for fluid flow in the continuum regime. It is derived from the fundamental physical laws: Newton's second law of motion and conservation of mass with the constraints that the fluid is continuum, the frame of reference is inertial (non-accelerating) and no reactions takes place in the fluid. The numerical framework proposed in this chapter solves this governing equations with the assumptions: flow is incompressible, single phase, isothermal, laminar and two-dimensional.

2.2 Governing equations

The Navier-Stokes equations for incompressible non-Newtonian flow are,

$$\frac{\partial u_\alpha}{\partial x_\alpha} = 0 \tag{2.1}$$

$$\frac{\partial u_\alpha}{\partial t} + u_\beta \frac{\partial u_\alpha}{\partial x_\beta} = -\frac{\partial p}{\partial x_\alpha} + \frac{\partial \tau_{\alpha\beta}}{\partial x_\beta} \tag{2.2}$$

The above Eqs. (2.1) and (2.2) respectively represent the continuity and momentum equations, where u_α denotes the Cartesian velocity components (with α being index), t is the time, p is the pressure where density is absorbed and $\tau_{\alpha\beta}$ is the stress tensor with α and β denoting running indices. The variables in the governing equations can be normalized using suitable reference quantities. The reference scales for velocity, length, time and viscosity are denoted by U_∞, L_∞, L_∞/U_∞ and μ_∞ respectively. In the present computational framework, the non-Newtonian flow is modelled using a non-linear constitutive relation,

$$\tau_{\alpha\beta} = \frac{1}{Re}\mu(|\dot{\gamma}|)\dot{\gamma}_{\alpha\beta} \tag{2.3}$$

where, Re is the Reynolds number, and $\mu(|\dot{\gamma}|)$ is known as the apparent or effective viscosity that depends on the second invariant $|\dot{\gamma}|$ of strain-rate tensor $\dot{\gamma}_{\alpha\beta}$ which can be expressed in terms of the velocity gradients as,

$$\dot{\gamma}_{\alpha\beta} = \frac{\partial u_\alpha}{\partial x_\beta} + \frac{\partial u_\beta}{\partial x_\alpha} - \frac{2}{3}\frac{\partial u_\alpha}{\partial x_\alpha}\delta_{\alpha\beta} \tag{2.4}$$

where, $\delta_{\alpha\beta}$ denotes the Kronecker delta (unity for $\alpha = \beta$ and zero if $\alpha \neq \beta$). The magnitude of $\dot{\gamma}_{\alpha\beta}$ in two-dimensions is given by,

$$|\dot{\gamma}| = \sqrt{2\left[\left(\frac{\partial u}{\partial x}\right)^2 + \left(\frac{\partial v}{\partial y}\right)^2\right] + \left(\frac{\partial u}{\partial y} + \frac{\partial v}{\partial x}\right)^2} \tag{2.5}$$

It can be easily seen from Eq. (2.5) that the present non-Newtonian fluid model does not account for time history of the apparent viscosity which is beyond the scope of this thesis work. We restrict ourselves to power-law and Carreau family of models, in addition to Newtonian fluid which follows as a special case of power-law fluid with $n = 1$. The models are listed in Table 2.1 and are used in the present study because the shear-thinning power law fluids and Carreau fluids are the most popularly used fluid models to simulate blood flow. In the followings, the apparent viscosity is simply denoted by μ instead of $\mu(|\dot{\gamma}|)$ for convenience.

The power-law model is a simple model that can exhibit both shear-thinning ($n < 1$) and shear-thickening ($n > 1$) behaviours. However, the drawback of the power-law fluid model is that it fails to describe the non-Newtonian behaviour at very low and very high shear rate regions by predicting infinite viscosity [6]. These shortcomings are overcome by the Carreau-Yasuda fluid model which is the most common model in the Carreau family. In these two non-Newtonian models, the Reynolds numbers are defined as $Re = \rho_\infty U_\infty^{2-n} L_\infty^n / K$ and $Re = \rho_\infty U_\infty L_\infty / \mu_\infty$ respectively, where K denotes the consistency coefficient of power-law fluid model.

Table 2.1: Constitutive relations for Newtonian and non-Newtonian fluids in non-dimensional form. μ_0 and μ_∞ are the viscosities at zero and infinite shear rate limits respectively, Wi is the dimensionless relaxation time of the fluid and is known as Weisenberg number, and a is the model constant.

Fluid model	Apparent viscosity
Newtonian	$\mu = 1$
Power–law [59]	$\mu = \lvert\dot{\gamma}\rvert^{n-1}$
Carreau–Yasuda [4, 25, 60]	$\mu = 1 + \left(\frac{\mu_0}{\mu_\infty} - 1\right)\left[1 + (\text{Wi}\ \lvert\dot{\gamma}\rvert)^a\right]^{\left(\frac{n-1}{a}\right)}$

On mathematical manipulation of Eq. (2.2) using Eq. (2.1), the momentum equation can be expressed in the conservative form given by,

$$\frac{\partial u_\alpha}{\partial t} + \frac{\partial}{\partial x_\beta}\left(u_\alpha u_\beta - \tau_{\alpha\beta}\right) = -\frac{\partial p}{\partial x_\alpha} \tag{2.6}$$

The above equation and the continuity Eq. (2.1) can be recast in the following compact

vector form,

$$\nabla \cdot \mathbb{U} = 0 \tag{2.7}$$

$$\frac{\partial \mathbb{U}}{\partial t} + \nabla \cdot \overline{\mathbb{H}} = \mathbb{Q} \tag{2.8}$$

It must be emphasised that the term $\overline{\mathbb{H}}$ itself is a vector of vectors which is defined by $\overline{\mathbb{H}} = [\mathbb{E} \quad \mathbb{F}]$ in two-dimensions (extension to three-dimensions is straightforward). The vectors $\mathbb{E}$, $\mathbb{F}$, and $\mathbb{Q}$ have the following Cartesian components,

$$\mathbb{U} = \begin{pmatrix} u \\ v \end{pmatrix} \qquad \mathbb{E} = \begin{pmatrix} u^2 - \tau_{xx} \\ uv - \tau_{xy} \end{pmatrix} \qquad \mathbb{F} = \begin{pmatrix} uv - \tau_{yx} \\ v^2 - \tau_{yy} \end{pmatrix} \qquad \mathbb{Q} = \begin{pmatrix} -\dfrac{\partial p}{\partial x} \\ -\dfrac{\partial p}{\partial y} \end{pmatrix}$$

where, u and v represent the Cartesian velocity components, and τ with the respective components denotes the viscous stress tensor.

2.3 Hybrid staggered/non-staggered framework

The key idea behind the hybrid staggered/non-staggered approach is to evaluate the fluxes (convective and viscous) at the cell centroids in the same manner as in a non-staggered framework (see Figure 2.1(c)) but to solve the momentum equation for velocities at the faces similar to a staggered framework. This is in sharp contrast to a purely staggered formulation (see Figure 2.1(a)) where the convective and diffusive fluxes would be discretised directly at the face center. It must be noted that the because update and storage of the velocity (normal velocity) still occurs at the face centers with the fluxes computed at cell centers interpolated to faces and therefore, it is referred to as *hybrid staggered/non-staggered framework* which is shown in Figure 2.1(b). In this framework, one therefore needs to solve for only one momentum equation referred to as “normal momentum equation” instead of two momentum equations in two dimensions. We shall now discuss the derivation of the normal momentum equation and its discretisation. We work with the integral form of the governing equations since we

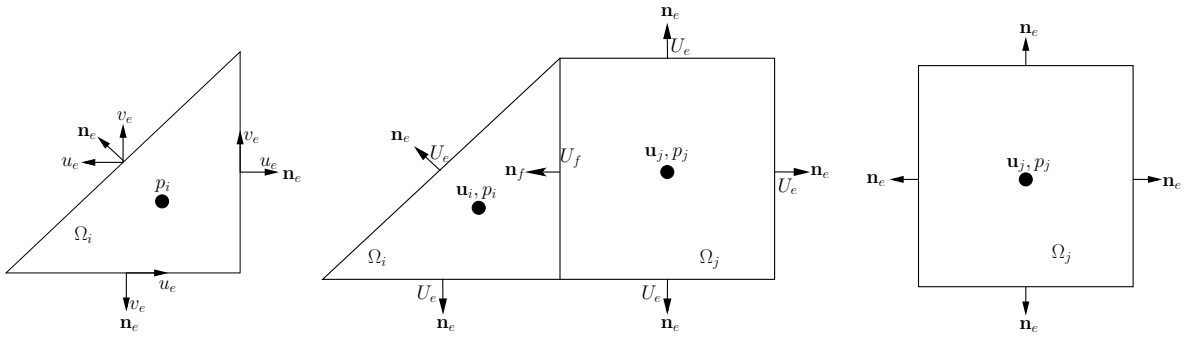

(a) Staggered mesh (b) Hybrid staggered/non-staggered mesh (c) Collocated mesh

Figure 2.1: Storage of solution variables for the different mesh frameworks. $\Omega_i \cup \Omega_j = \Omega$ is the control volume for the hybrid staggered/non-staggered framework where the two control cells i and j share the face $f \subseteq e$ and e denotes the set of edges of a control cell with corresponding unit normal vector $\mathbf{n}_e$. $\mathbf{n}_f \subseteq \mathbf{n}_e$ indicates the unit normal vector of f.

adopt the finite volume method. To derive the normal momentum equation, Eq. (2.8) is integrated over the finite control volume Ω as shown in Figure 2.1(b) and then projected along $\mathbf{n}_f$ to yield,

$$\int_\Omega \frac{\partial \mathbb{U}}{\partial t}\, d\Omega \cdot \mathbf{n}_f + \int_\Omega \nabla \cdot \overline{\mathbb{H}}\, d\Omega \cdot \mathbf{n}_f = \int_\Omega \mathbb{Q}\, d\Omega \cdot \mathbf{n}_f \tag{2.9}$$

In the present study, the control volumes are fixed in time and on applying Gauss divergence theorem to the second term of Eq. (2.9) we get,

$$\frac{\partial}{\partial t}\int_\Omega \mathbb{U}_f\, d\Omega + \left(\oint_{S(\Omega)} \overline{\mathbb{H}}_e \cdot \mathbf{n}_e\, dS\right) \cdot \mathbf{n}_f = \int_\Omega \mathbb{Q}_f\, d\Omega \tag{2.10}$$

where, $\mathbb{U}_f = \mathbb{U} \cdot \mathbf{n}_f$ and $\mathbb{Q}_f = \mathbb{Q} \cdot \mathbf{n}_f$ are the projection of centroidal velocity and pressure gradient along the unit normal $\mathbf{n}_f$ to the face f. The above Eq. (2.10) can be further simplified to yield,

$$\Omega \frac{\partial \hat{U}_f}{\partial t} + \left(\oint_{S(\Omega)} \overline{\mathbb{H}}_e \cdot \mathbf{n}_e\, dS\right) \cdot \mathbf{n}_f = \Omega \hat{Q}_f \tag{2.11}$$

where, $\hat{U}_f$ and $\hat{Q}_f$ are the cell (Ω) averaged normal velocity and pressure gradient respectively and are lumped at the center of f and are obtained from the following

relations,

$$\hat{U}_f = \frac{1}{\Omega}\int_{\Omega} \mathbb{U}_f d\Omega \tag{2.12}$$

$$\hat{Q}_f = \frac{1}{\Omega}\int_{\Omega} \mathbb{Q}_f d\Omega \tag{2.13}$$

Henceforth, the notation '$\wedge$' (hat) will have been omitted from the normal velocity and pressure gradient for convenience. The semi-discrete form of the Eq. (2.11) after approximating the flux integral by single point Gauss quadrature[1] can be represented as,

$$\frac{\partial U_f}{\partial t} \approx \underbrace{\frac{1}{\Omega}\Big[\sum_{e\in S(\Omega)} \overline{\mathbb{H}}_e \cdot \mathbf{n}_e \, \Delta S_e\Big] \cdot \mathbf{n}_f}_{\text{Flux term}} - \frac{\delta p}{\delta n}\Big|_f \tag{2.14}$$

where, ΔS_e denotes the surface area of e that constitutes the control surfaces of the control cells Ω_i and Ω_j. The flux term comprises of convective $\overline{\mathbb{H}}_{e,c}$ and viscous $\overline{\mathbb{H}}_{e,v}$ fluxes and they are given by,

$$\overline{\mathbb{H}}_{e,c} = \begin{pmatrix} -u^2 & -uv \\ -uv & -v^2 \end{pmatrix} \qquad \overline{\mathbb{H}}_{e,v} = \begin{pmatrix} \tau_{xx} & \tau_{xy} \\ \tau_{yx} & \tau_{yy} \end{pmatrix} \tag{2.15}$$

The convective and viscous fluxes are first evaluated at the cell centers and then interpolated to the faces while the discrete normal pressure gradient $\delta p/\delta n|_f$ is evaluated at f. It is important to note that the momentum equation uses a control volume that consists of the union of two cells. As such, the control volumes for the normal momentum equation for adjacent cells would indeed overlap. Despite the use of overlapping control volumes, we shall demonstrate in Chapter 4 that the approach indeed conserves mass and momentum discretely on all mesh topologies. The discretisation of the convective and viscous fluxes as well as other terms appearing in the momentum equation are described in the following sections.

[1] Single point Gauss quadrature at the center of e is enough for second order flux accuracy [7].

2.3.1 Discretisation of convective fluxes

The convective contribution to the flux term in Eq. (2.28) after substituting the convective part $\mathbb{H}^*_{e,c}$ of Eq. (2.15) and on simplification gives,

$$\frac{1}{\Omega}\Big[\sum_{e\in S(\Omega)} \overline{\mathbb{H}}^*_{e,c}\cdot\mathbf{n}_e\,\Delta S_e\Big]\cdot\mathbf{n}_f = \frac{1}{\Omega}\left[\sum_{e\in S(\Omega)}\begin{pmatrix}-u_e\\-v_e\end{pmatrix}U^*_e\Delta S_e\right]\cdot\mathbf{n}_f \tag{2.16}$$

where, u_e, v_e are the Cartesian components of the convective velocity vector $\mathbf{u}_e$, and $U^*_e = \mathbb{U}^*\cdot\mathbf{n}_e$ are the normal velocity at the center of the edge e. Here, the term U^*_e which makes the convective flux term non-linear is linearised by taking its value at the latest available time level. It must be emphasised that the velocity components of $\mathbf{u}_e$ are unknown and are computed using a second-order upwind scheme defined by,

$$\mathbf{u}_e = \begin{cases} \mathbf{u}_i + \nabla\mathbf{u}_i\cdot(\mathbf{x}_e-\mathbf{x}_i) & \text{if} \quad U^*_e \geq 0 \\ \mathbf{u}_s + \nabla\mathbf{u}_s\cdot(\mathbf{x}_e-\mathbf{x}_s) & \text{if} \quad U^*_e < 0 \end{cases} \tag{2.17}$$

where, $\mathbf{x}_e$ refers to the position vector at the center of e, $\mathbf{x}_i$ and $\mathbf{x}_s$ represent the position vectors of the centroids of the cells i and s respectively (see Figure 2.2(b)). The centroidal velocities are clearly not known either and are related to the face normal velocities which are the unknowns to be computed from the momentum equation. It is evident that although we solve for the normal velocity U^*_f at the faces, we require the velocities as well as their gradients at cell centroids. The latter is necessary for the evaluation of inviscid fluxes to higher order accuracy (see Eq. 2.17 above) as well as to compute viscous fluxes whose discretisation is described in the following section.

2.3.2 Discretisation of diffusive fluxes

The diffusive flux contribution to the flux term in Eq. (2.28) from the two neighbouring cells is obtained by substituting $\overline{\mathbb{H}}^*_{e,v}$ from Eq. (2.15) and on simplification yields,

$$\frac{1}{\Omega}\Big[\sum_{e\in S(\Omega)} \overline{\mathbb{H}}^*_{e,v}\cdot\mathbf{n}_e\,\Delta S_e\Big]\cdot\mathbf{n}_f = \frac{1}{\Omega}\left[\sum_{e\in S(\Omega_i)}\begin{pmatrix}\tau_{xx}|_e n_{e,x} & \tau_{xy}|_e n_{e,y}\\ \tau_{yx}|_e n_{e,x} & \tau_{yy}|_e n_{e,y}\end{pmatrix}\Delta S_e\right]\cdot\mathbf{n}_f \tag{2.18}$$

where, $n_{e,x} = \Delta S_{e,x}/\Delta S_e$ and $n_{e,y} = \Delta S_{e,y}/\Delta S_e$ denote the Cartesian components of the unit normal vector $\mathbf{n}_e$ (see Figure 2.2(a)) at e, and $\tau_{xx}|_e$ with the other components represent the stresses at e and are obtained from Eq. (2.3) as follows:

$$\tau_{xx}|_e = \frac{\mu_e}{Re}\left[2\frac{\delta u}{\delta x}\Big|_e\right] \tag{2.19}$$

$$\tau_{xy}|_e = \frac{\mu_e}{Re}\left(\frac{\delta u}{\delta y}\Big|_e + \frac{\delta v}{\delta x}\Big|_e\right) = \tau_{yx}|_e \tag{2.20}$$

$$\tau_{xx}|_e = \frac{\mu_e}{Re}\left[2\frac{\delta v}{\delta y}\Big|_e\right] \tag{2.21}$$

where, μ_e is the apparent viscosity at e which is obtained from second invariant of strain rate tensor and using suitable constitutive model (see Table 2.1). The apparent viscosity introduces non-linearity into the viscous flux contribution and is linearised by taking this value at the previous time level akin to the linearisation of the convective term. It must be emphasised that this is in contrast with Newtonian flows where the diffusive term is clearly linear and requires no further linearisation. The discrete velocity gradients at e are calculated from the adjacent cell centroid (i and s) gradients described in Section 2.3.7 as follows [61]:

$$\frac{\delta u}{\delta x}\Big|_e = \frac{1}{2}\left(\frac{\delta u}{\delta x}\Big|_i + \frac{\delta u}{\delta x}\Big|_s\right) - \mathrm{C} \tag{2.22}$$

where, C represents the correction term to mitigate decoupling and is given by,

$$\mathrm{C} = \left[\frac{1}{2}\left(\frac{\delta u}{\delta x}\Big|_i + \frac{\delta u}{\delta x}\Big|_s\right)n_{l,x} + \frac{1}{2}\left(\frac{\delta u}{\delta y}\Big|_i + \frac{\delta u}{\delta y}\Big|_s\right)n_{l,y} - \frac{u_s - u_i}{|\Delta\mathbf{x}_{is}|}\right]n_{l,x} \tag{2.23}$$

where, $n_{l,x}$ and $n_{l,y}$ are the x and y components of the unit vector $\mathbf{n}_l$ along the line $|\Delta\mathbf{X}_{is}|$ joining the two cell centroids i and s, and $\Delta\mathbf{X}_{is}$ refers to the displacement from i to s (see Figure 2.2(b)). The discrete velocity gradients $\delta u/\delta y|_e, \delta v/\delta x|_e$ and $\delta v/\delta y|_e$ are computed in the analogous manner. The unit vector $\mathbf{n}_l$ along the line connecting the two adjacent cell centroids is calculated as,

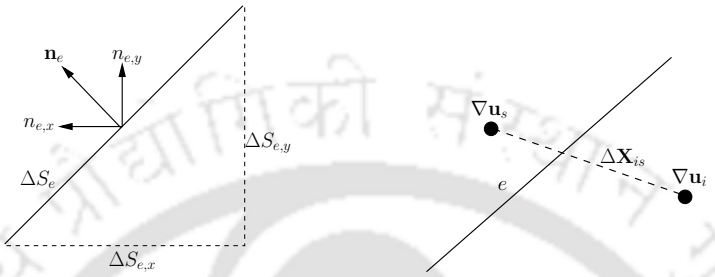

Figure 2.2: (a) Arbitrarily oriented area vector $\mathbf{n}_e\Delta S_e$ of e with its x and y parts, $\Delta S_{e,x}$ and $\Delta S_{e,y}$ and the respective components of the unit normal vector $n_{e,x}$ and $n_{e,y}$. (b) Displacement $\Delta\mathbf{x}_{is}$ required to obtain the directional derivative in C from the cell centroid i to s.

$$\mathbf{n}_l = \frac{\Delta\mathbf{x}_{is}}{|\Delta\mathbf{x}_{is}|} \tag{2.24}$$

It is must be remarked that in spite of the staggered positioning of the normal momentum, the calculation of gradients and the fluxes are similar to those in a collocated framework. In particular, as far as the viscous contribution is concerned, the gradients are first computed at the cell centers and then interpolated on the faces to obtain the diffusive fluxes.

2.3.3 Discretisation of normal pressure gradient

The normal pressure gradient term at a cell face in the normal momentum equation can be discretised using simple central differencing in Cartesian mesh. In unstructured mesh/cell however we have to discretise it along a line normal to the face f as shown

in Figure 2.3(a) and is given by,

$$\left.\frac{\delta p^m}{\delta n}\right|_f = \frac{p^m_{j'} - p^m_{i'}}{|\Delta \mathbf{n}_i| + |\Delta \mathbf{n}_j|} \tag{2.25}$$

where, $p_{i'}$ and $p_{j'}$ are the pressure at the points i' and j' on the line vector $\Delta \mathbf{n}_i$ and

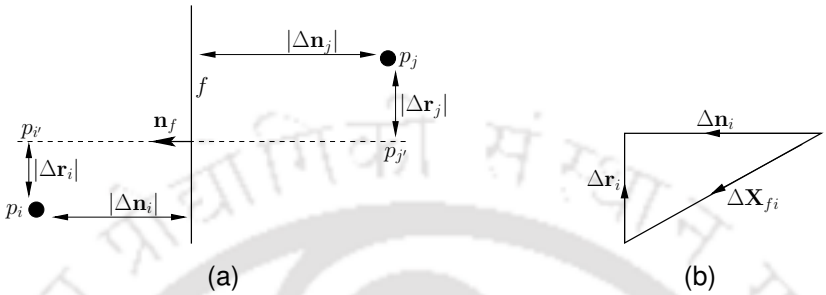

Figure 2.3: (a) Non-orthogonal cell centroids i and j with respect to the face f shared by two adjacent control volumes those hold the two pressure fields p_i and p_j respectively. $\Delta \mathbf{r}_i$ and $\Delta \mathbf{r}_j$ denote the displacements from the respective cell centroids to i' and j' respectively that lie on the line coinciding with the direction of unit normal vector $\mathbf{n}_f$. $|\Delta \mathbf{n}_i|$ and $|\Delta \mathbf{n}_j|$ denote the shortest distances of the cell centroids i and j respectively from f. (b) Representation of directions of the different vectors.

$\Delta \mathbf{n}_j$ respectively. Since, $p_{i'}$ and $p_{j'}$ are not known they are expressed in terms of cell centroid pressures p_i and p_j using truncated Taylor series which after rearrangement yields,

$$\left.\frac{\delta p^m}{\delta n}\right|_f = \frac{p^m_j - p^m_i}{|\Delta \mathbf{n}_i| + |\Delta \mathbf{n}_j|} + \frac{\Delta \mathbf{r}_j \cdot \nabla p^m_j - \Delta \mathbf{r}_i \cdot \nabla p^m_i}{|\Delta \mathbf{n}_i| + |\Delta \mathbf{n}_j|} \tag{2.26}$$

The second term of the right hand side of Eq. (2.26) indicates the correction term to account for mesh non-orthogonality and is zero for orthogonal meshes.

2.3.4 Temporal term discretisation and time integration

Explicit schemes are easier to implement for time marching of solution variables compared to their implicit counterpart [62, 63] but have stringent time step restrictions. We adopt an implicit treatment of the convective and viscous fluxes in the present study and also treat the time derivative in Eq. (2.14) using a second-order accurate three

point backward differencing approach that reads,

$$\frac{dU_f}{dt} = \frac{3\,U_f^{m+1} - 4\,U_f^{m} + U_f^{m-1}}{2\,\Delta t} \tag{2.27}$$

where, superscripts $m+1$, m, and $m-1$ represent the time levels t^{m+1}, t^m, and t^{m-1} respectively with the time step $\Delta t = t^{m+1} - t^m = t^m - t^{m-1}$. We adopt the fractional step approach similar to the approach utilized in [43] where we solve the momentum equation for auxiliary (or intermediate) momentum by considering the pressure contribution at the m^{th} time level. The auxiliary quantities are denoted by superscript '*' and the discrete normal momentum equation that is solved for at the faces reads,

$$\frac{3\,U_f^{*} - 4\,U_f^{m} + U_f^{m-1}}{2\,\Delta t} = \frac{1}{\Omega}\Big[\sum_{e\in S(\Omega)}\Big(\overline{\mathbb{H}}^{*}_{e,c} + \overline{\mathbb{H}}^{*}_{e,v}\Big)\cdot\mathbf{n}_e\,\Delta S_e\Big]\cdot\mathbf{n}_f + \frac{\delta p^m}{\delta n}\Big|_f \tag{2.28}$$

It is important to note that this approach is adopted since one needs to artificially construct an evolution equation for pressure. The normal derivative for pressure appearing in the above equation is a source term although the convective and viscous fluxes does depend on the unknown face normal velocities. The right hand side of Eq. (2.28) represents a residual that comprise of the fluxes and cell averaged normal pressure gradient representing the spatial discretisation. It must be emphasized that this step, referred to as the "momentum step" is fully implicit and second-order accurate (assessed in Section 4.2) in time [2]. The non-linear implicit normal momentum equation for the auxiliary normal velocity U_f^* is solved by an inexact Newton-Krylov solver using the open source libraries PetSc [64]. We now discuss the approach to obtain the pressure field and to correct the auxiliary momentum in the sections to follow.

[2]The first momentum step ($m = 0$) uses an implicit Euler discretisation, since values at $(m-1)$ are then not available. The first-order accuracy in a single step does not affect the overall second-order temporal accuracy.

2.3.5 Pressure correction equation

There is no time evolution equation for pressure field in the incompressible flows and therefore we construct a pressure correction equation to obtain the pressure field. To derive the pressure correction, we have to make use of the momentum equation and the continuity equation. The discrete form of the implicit momentum equation is given by,

$$\frac{3\mathbb{U}^{m+1} - 4\mathbb{U}^{m} + \mathbb{U}^{m-1}}{2\Delta t} = \mathbb{C}^{m+1} + \mathbb{D}^{m+1} - \mathbb{G}p^{m+1} \tag{2.29}$$

where, $\mathbb{C}$, $\mathbb{D}$ and $\mathbb{G}$ denote the discrete convective flux, diffusive flux and pressure gradient operators respectively. The equation solved for the auxiliary momentum field treats the pressure gradient term explicitly and consequently the velocity field from the following equation does not satisfy the continuity equation.

$$\frac{3\mathbb{U}^{*} - 4\mathbb{U}^{m} + \mathbb{U}^{m-1}}{2\Delta t} = \mathbb{C}^{*} + \mathbb{D}^{*} - \mathbb{G}p^{m} \tag{2.30}$$

Subtracting Eq. (2.30) from Eq. (2.29) yields,

$$\frac{3\mathbb{U}^{m+1} - 3\mathbb{U}^{*}}{2\Delta t} = (\mathbb{C}^{m+1} - \mathbb{C}^{*}) + (\mathbb{D}^{m+1} - \mathbb{D}^{*}) - (\mathbb{G}p^{m+1} - \mathbb{G}p^{m}) \tag{2.31}$$

Neglecting the contributions $\mathbb{C}^{m+1} - \mathbb{C}^{*}$ and $\mathbb{D}^{m+1} - \mathbb{D}^{*}$ leads to,

$$\frac{3\mathbb{U}^{m+1} - 3\mathbb{U}^{*}}{2\Delta t} = -\mathbb{G}\phi \tag{2.32}$$

where, $\phi = p^{m+1} - p^{m}$ denotes the pressure correction. Taking discrete divergence ($\mathcal{D}$) of the above equation and invoking $\mathcal{D}\mathbb{U}^{m+1} = 0$ using continuity equation results in,

$$\frac{2\Delta t}{3}\mathcal{D}(\mathbb{G}\phi) = \mathcal{D}\mathbb{U}^{*} \tag{2.33}$$

Integrating the above equation over a control volume Ω_i[3] and approximating it with Gauss quadrature after using Gauss-divergence theorem to convert the volume integration to the surface integration gives (after further simplification),

$$\sum_{e\in S(\Omega_i)} \frac{2\Delta t}{3} \left.\frac{\delta\phi}{\delta n}\right|_e \Delta S_e = \sum_{e\in S(\Omega_i)} U_e^* \Delta S_e \tag{2.34}$$

where, $\delta\phi/\delta n|_e$ represents the discrete value of the normal gradient of ϕ at e and is calculated using the same discrete operator as employed for the discretisation of the normal pressure gradient (in Eq. (2.26)) as,

$$\left.\frac{\delta\phi}{\delta n}\right|_e = \frac{\phi_s - \phi_i}{|\Delta\mathbf{n}_i| + |\Delta\mathbf{n}_s|} + \frac{\Delta\mathbf{r}_s \cdot \nabla\phi_s - \Delta\mathbf{r}_i \cdot \nabla\phi_i}{|\Delta\mathbf{n}_i| + |\Delta\mathbf{n}_s|} \tag{2.35}$$

where, ϕ_i and ϕ_s denote pressure corrections at the two cell centroids sharing the edge e, and $\nabla\phi_i$ and $\nabla\phi_s$ are the corresponding gradients. Here, $|\Delta\mathbf{n}_s|$ is the normal length between the cell centroid s and face e, and $\Delta\mathbf{r}_s$ is the displacement to account for the non-orthogonal cell centroid $\mathbf{X}_s$ with reference to $\mathbf{X}e$. Defining $l = |\Delta\mathbf{n}_i| + |\Delta\mathbf{n}_s|$ and substituting Eq. (2.35) in Eq. (2.34) with rearrangement yields,

$$\sum_{e\in S(\Omega_i)} \frac{2\Delta t}{3}\frac{\phi_s}{l}\Delta S_e - \sum_{e\in S(\Omega_i)} \frac{2\Delta t}{3}\frac{\phi_i}{l}\Delta S_e = \sum_{e\in S(\Omega_i)} U_e^* \Delta S_e - \sum_{e\in S(\Omega_i)} \frac{2\Delta t}{3}\frac{\Delta\mathbf{r}_s \cdot \nabla\phi_s - \Delta\mathbf{r}_i \cdot \nabla\phi_i}{l}\Delta S_e \tag{2.36}$$

This is known as the pressure correction equation and the right hand side term is a source term since U_e^* is obtained from the auxiliary normal momentum Eq. (2.28). The second term of right hand side of Eq. (2.36) however is dependent on the solution variable ϕ. However, by lagging this term and employing a defect correction like approach (treating the gradient terms as a source term) the resulting linear system of equations can be represented as,

$$\mathbb{A}\Phi^{q+1} = \mathbf{S} - \mathbf{f}(\nabla\phi^q) \tag{2.37}$$

[3]Integration is performed over a single control volume unlike for the normal momentum equation where integration is carried out over the union of two adjacent control cells.

where, $\mathbb{A}$ denotes the matrix consists of geometric quantities, Φ refers to the vector comprising of the pressure corrections at the cell centroids, and $\mathbf{S}$ indicates the known vector source term. The presence of the non-orthogonality correction term yields the function $\mathbf{f}$ that contain gradients of ϕ at the cell centroids and necessitates the solution of this linear system several times in a given time step. Equation (2.37) is essentially a Poisson equation and is solved by an algebraic-multigrid preconditioned GMRES (generalised minimal residual) solver utilising the open source library LiS (library of iterative solvers) [65]. The outer iterations are started with $\Phi = 0$ and consequently $\nabla\phi = 0$ and are terminated when $||\Phi^{q+1} - \Phi^{q}||_{\infty} \leq 10^{-10}$, while the inner Krylov iterations are converged when the relative error is less than 10^{-10}. No sub-iterations are needed on uniform Cartesian meshes and 8-10 outer iterations are sufficient for non-orthogonal meshes to solve the Eq. (2.37).

2.3.6 Solution update

After obtaining the normal auxiliary momentum and the pressure correction (ϕ), the normal velocity and the pressure field at the next time level ($m+1$) are computed as,

$$U_f^{m+1} = U_f^{*} - \frac{2}{3}\frac{\Delta t}{}\left.\frac{\delta\phi}{\delta n}\right|_f \tag{2.38}$$

$$p^{m+1} = p^{m} + \phi \tag{2.39}$$

where, $\delta\phi/\delta n|_f$ is the normal gradient of ϕ at f and is computed in the same manner as $\delta p/\delta n|_f$ in Eq. (2.26). The updated centroidal velocities are obtained after reconstruction (see Section 2.3.7) from the updated normal velocity U_f^{m+1} in addition to the gradients (velocity, pressure and pressure correction) which are computed at the cell centroids.

2.3.7 Velocity reconstruction and gradient computation

Discretisation of the convective (see Eq. (2.17)) and viscous (see Eq. (2.23)) fluxes necessitate the centroidal velocities as well as their gradients. Therefore, velocity reconstruction from the normal velocity U_f at the cell centroid is an essential feature of the hybrid staggered/non-staggered finite volume framework. The centroidal velocity $\mathbf{u}_i$ is reconstructed from the known U_f^{m+1} to second order accuracy using an iterative defect correction strategy based on the Green-Gauss theorem. This reconstruction and the subsequent computation of gradients are critical for accurate numerical simulations and is described in detail in Chapter 3.

2.3.8 Boundary conditions

The well-posedness of the incompressible Navier-Stokes equations is decided by the boundary conditions pertinent to the specific problem being solved. We discuss the most common boundary conditions and their implementation in our framework in this section. For a Dirichlet velocity field $\mathbf{u}_b$ at a boundary shown in Figure 2.4(a), the normal velocity U_b^* is calculated as,

$$U_b^* = u_b n_{b,x} + v_b n_{b,y} \tag{2.40}$$

where, $\mathbf{n}_b$ is the unit normal vector of the boundary surface b with its components $n_{b,x}$

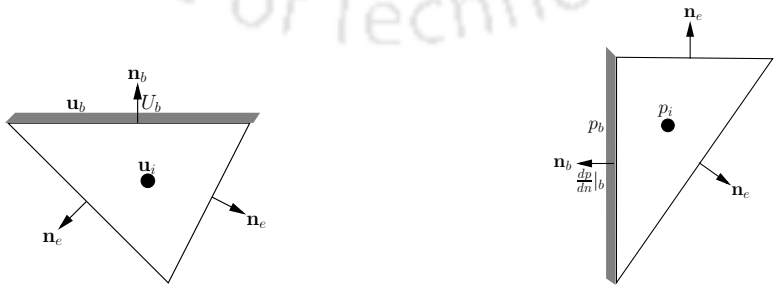

(a) Dirichlet velocity boundary

(b) Dirichlet pressure boundary

Figure 2.4: Implementation of boundary conditions. Subscript 'b' denotes the boundary values for the different quantities.

and $n_{b,y}$, u_b and v_b denote the x and y velocities respectively. The normal momentum equation is not solved on these boundaries since $U_b^{m+1} = U_b^*$. This leads to $\delta\phi/\delta n|_b = 0$ and consequently $\delta p/\delta n|_b = 0$. This can be easily seen from Eq. (2.38) which at the boundary reads,

$$U_b^{m+1} = U_b^* - \frac{2\,\Delta t}{3}\left.\frac{\delta\phi}{\delta n}\right|_b \tag{2.41}$$

where, $\delta\phi/\delta n|_b$, and $\delta p/\delta n|_b$ are the normal pressure correction, and pressure gradients respectively at the boundary face b. In the present studies, a velocity profile that can vary with space and time are prescribed at the inlet whereas at the outlet boundary, it is obtained by a first–order accurate extrapolation from the adjacent cell centroids $\mathbf{u}_i$ sharing the faces at the outlet. Therefore, at the outlet boundary,

$$U_b^* = \mathbf{u}_i \cdot \mathbf{n}_b \tag{2.42}$$

In general, the auxiliary face normal momentum calculated in this way will not satisfy global mass conservation. Therefore, we apply a correction to the normal velocity on these faces (at the outlet) to satisfy the global mass conservation criterion. We thus have,

$$\sum_{b\in O} U_b^{(m+1)} \Delta S_b = 0 \tag{2.43}$$

where, O is the set of faces with area ΔS_b at the outlet boundary. We obtain these corrections by finding the global mass defect (difference between inlet and outlet mass flow rates) and equally redistributing it to the outlet faces so that the above equation is satisfied. It must be noted that the outlet velocities after correction act as if it were a Dirichlet boundary condition, which in turn means that the boundary condition on pressure correction is a homogeneous Neumann condition.

No convective and viscous fluxes conditions are imposed for the lines of symmetry and inviscid wall as well since the normal velocity $U_b^* = 0$. This boundary condition holds for the no-slip solid wall ($\mathbf{u}_b = 0$) as well although the viscous flux is obtained

using the velocity gradients at the boundary (from Eq. (2.22)),

$$\left.\frac{\delta u}{\delta x}\right|_b = \left.\frac{\delta u}{\delta x}\right|_i - \left(\left.\frac{\delta u}{\delta x}\right|_i n_{ib,x} + \left.\frac{\delta u}{\delta y}\right|_i n_{ib,y} - \frac{u_b - u_i}{|\Delta \mathbf{x}_{ib}|} \right) n_{ib,x} \tag{2.44}$$

where, $n_{ib,x}$ and $n_{ib,y}$ are the Cartesian parts of the unit normal vector $\mathbf{n}_{ib}$ of the displacement $\Delta \mathbf{x}_{ib}$ from the cell centroid i to the middle of boundary face b, and the other velocity gradients are also computed in the similar way.

In the prescribed boundary conditions for the pressure field p_b (see Figure 2.4(b)), the normal pressure gradient at the boundary $\delta p/\delta n|_b$ referring to Eq. (2.26) is computed as follows:

$$\left.\frac{\delta p^m}{\delta n}\right|_b = \frac{p_b - p_i^m}{|\Delta \mathbf{n}_{ib}|} - \frac{\Delta \mathbf{r}_i \cdot \nabla p_i^m}{|\Delta \mathbf{n}_{ib}|} \tag{2.45}$$

where, $|\Delta \mathbf{n}_{ib}|$ denotes the normal distance between the cell centroid i and the boundary face. For such boundaries, we clearly need to solve the normal momentum equation to obtain the normal velocity U_b^{m+1} at the boundary. However, we do not perform any correction for global mass conservation in this case. It must be remarked herein that all boundaries with a Neumann boundary condition are merely ignored in the solution of the pressure correction equation (since their contribution is zero in any case) but must be necessarily accounted for (using the prescribed pressure value, taken typically to be 0) when Dirichlet pressure boundary condition is imposed.

2.3.9 Solution algorithm

The solution approach underlying the hybrid staggered/non-staggered framework can be summarized in the flowchart shown in Figure 2.5.

2.4 Summary

In this chapter, we provide an overview of the governing equations for non-Newtonian incompressible flow followed by the details of the hybrid staggered/non-staggered com-

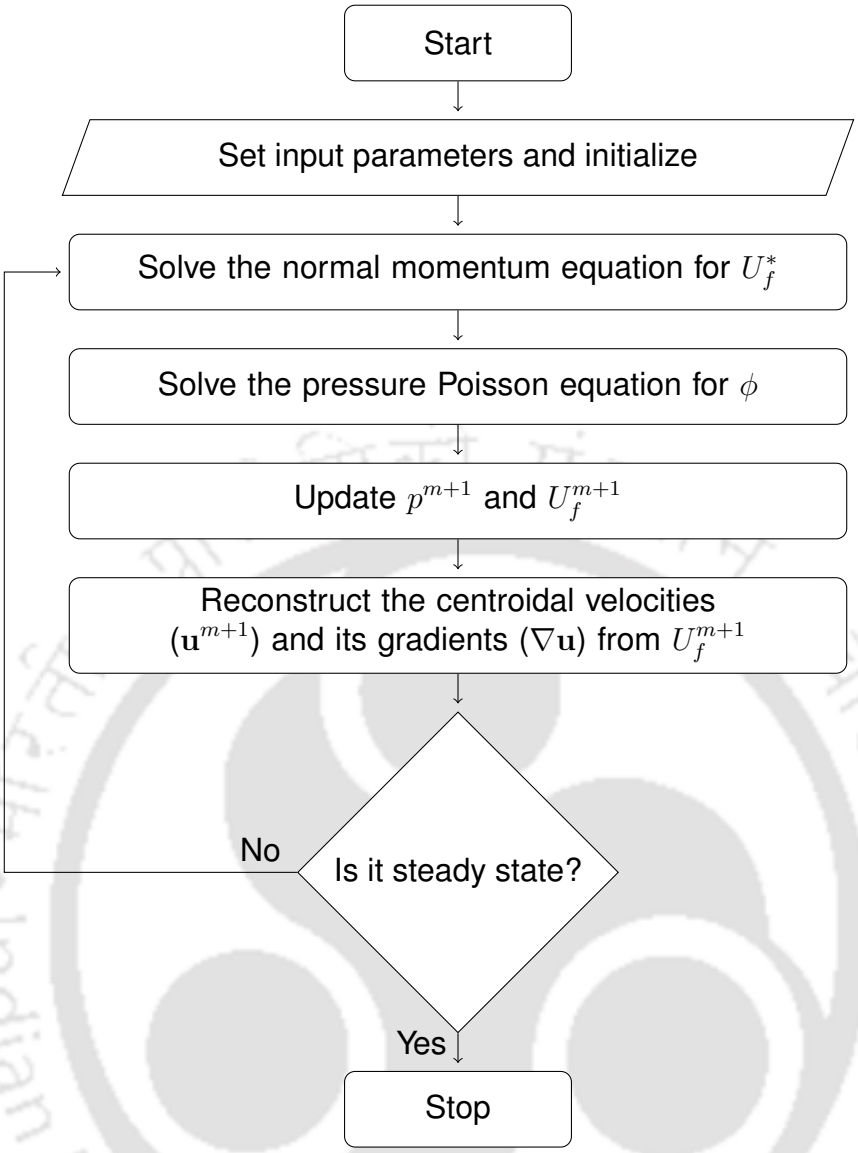

Figure 2.5: Flowchart of the solution procedure for the hybrid staggered/non-staggered finite volume computational framework.

putational framework. The finite volume discretisation of the convective and viscous fluxes as well as the temporal discretisation are discussed. The salient features of the framework and their implementation including the boundary conditions is presented and the framework shall be assessed on canonical problems later in the thesis.

Chapter 3

Velocity reconstruction

This chapter addresses the issues of velocity reconstruction on unstructured staggered meshes. A novel algorithm referred to as IDeC(k)-GG reconstruction that recovers centroidal velocities from face normal velocity on two-dimensional arbitrary polygonal meshes is proposed. It is a vector interpolation strategy that employs iterative defect correction in conjunction with a lower-order accurate Gauss reconstruction to obtain second-order accurate centroidal velocities. Various numerical experiments are performed on different mesh topologies and few canonical problems to demonstrate the importance and utility of the current velocity reconstruction algorithm.

3.1 Background

The velocity reconstruction approach is an essential part of the hybrid staggered/non-staggered finite volume framework (described in Chapter 2) for physically accurate solutions. Gilmanov and Sotiropoulos [40] as well as Ge and Sotiropoulos [43] have developed simple one-dimensional expressions to reconstruct centroidal velocities from their contravariant face velocities on Cartesian and curvilinear meshes respectively. Although simple to implement, their approaches are inherently limited by the need for having a logical grid structure. Natarajan and Sotiropoulos [41] devised a defect-correction based least-squares approach to recover the centroidal velocities. Their approach was cell-based and involved a relatively compact stencil and posed minimal

difficulties in terms of implementation on unstructured and hybrid meshes and extensions to three dimensions. However, their approach requires solution to system of linear equations which could be computationally expensive on fine grids and three-dimension.

The present study attempts to devise an alternative velocity reconstruction of staggered data as in [41] and demonstrate its utility for simulation of non-Newtonian flows in the incompressible regime. In particular, we carry out a thorough and detailed study of a variant of the approach in [41], involving a lower-order reconstruction based on Gauss theorem which was also introduced in [31]. The lower-order reconstruction employed by Perot [31] is first-order accurate and its accuracy is enhanced in the present study using the iterative defect correction strategy. The proposed variant, referred to as IDeC(k)-GG reconstruction in this study, is expected to be marginally faster than its least-squares counterpart in [41] and the importance of second-order accuracy is also highlighted herein.

3.2 IDeC(k)-GG algorithm for velocity reconstruction

This section describes in detail the new algorithm referred to as IDeC(k)-GG reconstruction. The primary motivation of the proposed algorithm is the development of higher-order accurate framework for velocity reconstruction on unstructured staggered meshes. The objective of the reconstruction algorithm is to obtain the centroidal velocity field $\mathbf{u}_i$ in each control volume Ω_i from the known face normal velocities U_f. The philosophy of the new reconstruction algorithm is to combine the lower-order reconstruction derived from the Gauss theorem with an iterative defect correction approach. The latter is a generic technique used for accuracy enhancement and is efficiently exploited in the present work in the design of the new algorithm. We describe below these ideas and later demonstrate their need for accurate simulations of non-Newtonian flows.

3.2.1 Reconstruction based on Gauss theorem

The centroidal velocities may be obtained from face normal velocities using the Gauss theorem as [31],

$$\mathbf{u}_i = \frac{1}{\Omega_i} \sum_f U_f (\mathbf{x}_f - \mathbf{x}_i) \Delta S_f \tag{3.1}$$

where, the summation is over the faces f of the cell whose centroid is i. The geometric quantities include the cell volume Ω, the position vector $\mathbf{x}$ and the face area ΔS. This reconstruction is a simple vector interpolation approach and is a direct consequence of Gauss divergence theorem where the centroidal velocity is assumed constant throughout the cell. This reconstruction has been employed previously in [31] and is only first-order accurate. It is interesting to note that this reconstruction however gives a simple closed-form expression for the velocity field in contrast to its least-squares counterpart [41] which requires the solution to a system of equations, for the same order of accuracy. We shall now provide an alternate derivation for the first-order accuracy of this reconstruction to highlight the "defect" that needs to be corrected (or removed) to achieve second-order accuracy.

The centroidal field in Eq. (3.1) is a numerical estimate for a given set of face-normal velocities. Rewriting the face-normal velocities in terms of the exact centroidal velocities using truncated Taylor series gives,

$$U_f = \left(\mathbf{u}_i^e + \nabla \mathbf{u}_i^e : (\mathbf{x}_f - \mathbf{x}_i) \right) \cdot \mathbf{n}_f + \mathbf{O}(||\mathbf{x}_f - \mathbf{x}_i||^2) \tag{3.2}$$

where the superscript "e" indicates "exact" values of the centroidal velocity field which are not known. Substitution of Eq. (3.2) in Eq. (3.1) and simplification gives,

$$\mathbf{u}_i = \mathbf{u}_i^e + \underbrace{\frac{1}{\Omega_i} \nabla \mathbf{u}_i^e : \sum_f ||\mathbf{x}_f - \mathbf{x}_i||^2 \mathbf{n}_f \Delta S_f}_{\text{Defect term}} + \mathbf{O}(||\mathbf{x}_f - \mathbf{x}_i||^2) \tag{3.3}$$

where, the symbols ":" and "$\cdot$" denote tensor and vector inner product respectively. It is

evident from Eq. (3.3) that the second term on the right hand side represents the truncation error due to Gauss reconstruction and is **O**(h) on arbitrary polygonal meshes where h is a characteristic grid scale associated with the mesh. This term is therefore, the “defect" which is responsible for the first-order accuracy of the reconstruction. A closer examination of the term also shows that on uniform Cartesian meshes, the defect is identically zero and the reconstructed velocities are second-order accurate.

3.2.2 Defect-corrected Gauss reconstruction

The analysis of the lower-order Gauss reconstruction indicates that if the defect could be reduced or ideally eliminated, then second-order accuracy of the reconstructed velocity field can be realized. This suggests the use of a “modified" face normal velocity in the Gauss reconstruction for enhancing the accuracy defined by,

$$\tilde{U}_f = U_f - \Big(\nabla \mathbf{u}_i^e : (\mathbf{x}_f - \mathbf{x}_i)\Big) \cdot \mathbf{n}_f \tag{3.4}$$

The definition of this “modified" scalar velocity is however, flawed in that it involves the “exact" derivatives of the centroidal velocity field which are not clearly known. Moreover, the centroidal velocities that appear (through the derivatives) in the definition are precisely what is sought by the reconstruction. These issues however, can be easily circumvented by replacing the “exact" derivatives by the numerically computed derivatives and then introducing an iterative approach for reconstruction. This leads to the following theorem that exemplifies the new algorithm, which is referred to as IDeC(k)-GG reconstruction.

Theorem 3.2.1 (IDeC(k)-GG reconstruction)**.** *The velocity reconstruction defined by,*

$$\mathbf{u}_i^k = \frac{1}{\Omega_i} \sum_f \tilde{U}_f (\mathbf{x}_f - \mathbf{x}_i) \Delta S_f \tag{3.5}$$

with a "modified" scalar face-normal velocity $\tilde{U}_f$ defined by,

$$\tilde{U}_f = U_f - \left(\nabla \mathbf{u}_i^{k-1} : (\mathbf{x}_f - \mathbf{x}_i)\right) \cdot \mathbf{n}_f \tag{3.6}$$

is second-order accurate if and only if the gradients are computed to atleast first order accuracy and the iterative process defined by Eqs. (3.5)-(3.6) converges.

Proof. We start by assuming that the iterative process defined by Eqs. (3.5)-(3.6) converges in some suitable norm so that the iteration counter k can be dropped from the analysis. Rewriting the face normal velocity U_f in terms of the exact Cartesian velocities of the cell where the velocity needs to be reconstructed, we have,

$$U_f = \left(\mathbf{u}_i^e + \nabla \mathbf{u}_i^e : (\mathbf{x}_f - \mathbf{x}_i)\right) \cdot \mathbf{n}_f + \mathbf{O}(||\mathbf{x}_f - \mathbf{x}_i||^2) \tag{3.7}$$

The velocity derivatives $\nabla \mathbf{u}_i$ appearing in the definition of the "modified" face normal velocity are computed using some numerical technique. Assuming that the derivatives so obtained are p^{th} order accurate, we have,

$$\nabla \mathbf{u}_i = \nabla \mathbf{u}_i^e + \mathbf{O}(h^p) \tag{3.8}$$

where h is some characteristic length scale associated with the mesh. Substitution of Eq. (3.7) and (3.8) in Eq. (3.6) and further simplification gives,

$$\tilde{U}_f = \mathbf{u}_i^e \cdot \mathbf{n}_f + \mathbf{O}(h^p)||\mathbf{x}_f - \mathbf{x}_i|| + \mathbf{O}(||\mathbf{x}_f - \mathbf{x}_i||^2) \tag{3.9}$$

Realising that $||\mathbf{x}_f - \mathbf{x}_i|| \sim h$, Eq. (3.9) reduces to,

$$\tilde{U}_f = \mathbf{u}_i^e \cdot \mathbf{n}_f + \mathbf{O}(h^{min(p+1,2)}) \tag{3.10}$$

The estimate of truncation error in the reconstruction is then obtained by using Eq. (3.10)

in Eq. (3.5) which results in,

$$\mathbf{u}_c = \mathbf{u}_c^e + \mathbf{O}(h^{min(p+1,2)}) \tag{3.11}$$

The reconstructed velocities are therefore second-order accurate iff $p \geq 1$ which is the condition of consistent gradients alluded to in the theorem. □

It must be remarked that the standard identities $\sum_f \mathbf{x}_f \cdot \mathbf{n}_f \Delta s_f = \Omega_i$ and $\sum_f \mathbf{n}_f \Delta S_f = \mathbf{0}$, and the variation in geometric quantities $\Delta S_f \sim \mathbf{O}(h^2)$ and $\Omega_i \sim \mathbf{O}(h^3)$ have been made use of in the proof. Although the theorem was briefly introduced in [41], we present the theorem in a more compact form with a complete proof for the first time in this work. Furthermore, we also carry out an extensive study of the theorem and the resulting IDeC(k)-GG reconstruction with special emphasis on non-Newtonian flows which is a focal point of the current study. It must also be mentioned that a rigorous mathematical proof of the convergence of the iterative approach involved in the algorithm is a non-trivial exercise which is beyond the scope of this work and extensive numerical experiments presented in Section 3 show that convergence is achieved in a few iterations thereby justifying the assumption made in the proof.

Remark 1: The first step of the IDeC(k)-GG reconstruction algorithm is merely the lower-order accurate Gauss reconstruction which is therefore, referred to also as IDeC(1)-GG reconstruction. On uniform Cartesian meshes, the “defect" term vanishes due to the cancellations arising due to grid regularity and the IDeC(1)-GG reconstruction is equivalent to IDeC(k)-GG reconstruction and is second order accurate.

Remark 2: The IDeC(k)-GG algorithm is generic and equally applicable in both two and three dimensions. It provides a closed-form reconstruction formula (although iterative) without the need for solution to system of equations and is hence expected to incur lesser computational effort and be marginally faster in comparison to the least-squares based IDeC(k) reconstruction proposed in [41].

3.2.3 Computing velocity gradients

The definition of the “modified" face-normal velocity involves the numerical computation of the centroidal velocity gradients that are dependent on the reconstructed velocities themselves. It has been proved earlier [41] that the choice of the numerical methodology for gradient evaluation must be driven by the need for atleast first-order accuracy of the computed gradients. Since the velocity reconstruction is based on Gauss theorem, it is logical to adopt a similar approach for obtaining centroidal gradients of the velocity components as well. The Green-Gauss reconstruction computes the centroidal gradients of any scalar φ as,

$$\nabla\varphi_i = \frac{1}{\Omega_i}\sum_f \varphi_f \mathbf{n}_f \Delta S_f \tag{3.12}$$

where φ_f represents the scalar values at the centroid of faces constituting a cell. The scalar Cartesian velocity components are unknowns and are reconstructed only at the centroids which means that the face values of these velocity components need also to be estimated numerically. It follows that the accuracy of the face values will influence the accuracy of the computed gradients. The choice of numerical method to obtain the face values from centroidal components is however critical and is reflected in the following theorem.

Theorem 3.2.2. *Let φ represents any component of the centroidal velocity vector which is b^{th} order accurate. If the Green-Gauss reconstruction approach is employed for gradient computation on an arbitrarily polygonal mesh and the face values obtained are v^{th} order accurate, then (i) $v = b$ and (ii) the order of accuracy of the gradients is min($1, v-1$).*

Proof. We know from Theorem 3.2.1 that $b = min(p+1, 2)$ where p is the order of accuracy of the centroidal gradients of velocity. Assuming that $p = min(1, v-1)$ is true, we then have $m = min(v, 2)$. Therefore, $v \geq b$. It is also clear that the face values of the velocity components are obtained from the centroidal values which are themselves only b^{th} order accurate. A little consideration then shows that order of accuracy of

the face values cannot exceed that of the quantities used to calculate it and therefore, $v \leq b$. It follows therefore, that $v = b$.

It is shown that the order of accuracy of gradients is $min(1, v-1)$. If the face values are accurate to order q then,

$$\varphi_f = \varphi_f^e + \mathbf{O}(h^v) \tag{3.13}$$

Also, rewriting the “exact" face values φ_f in terms of the “exact" centroidal values φ_i using Taylor's expansion gives,

$$\varphi_f^e = \varphi_i^e + \nabla\varphi_i^e \cdot (\mathbf{x}_f - \mathbf{x}_i) + \mathbf{O}(||\mathbf{x}_f - \mathbf{x}_i||^2) \tag{3.14}$$

Substitution of Eqs. (3.13) and (3.14) in Eq. (3.12) and further simplification gives,

$$\nabla\varphi_i = \nabla\varphi_i^e + \mathbf{O}(h^{min(1,v-1)}) \tag{3.15}$$

which is the desired result.

This proof conclusively demonstrates the complex interplay between the face values of velocity components, gradient computation and the accuracy of the reconstructed velocities. It also shows that the accuracy of the reconstructed velocities is identical to the accuracy to which their face values are estimated in the gradient computation and hence the latter holds the key to obtaining higher-order centroidal velocities. □

3.2.4 Determining face values in gradient computation

In the earlier subsections 3.2.2 and 3.2.3, we have shown that the accuracy of the velocity reconstruction from staggered data is governed by the accuracy of face values used in gradient computation for the IDeC(k)-GG algorithm. The face values must be obtained from the centroidal velocity components and the numerical method to achieve this objective is chosen in accordance with Theorem 3.2.3. It is clear therefore, that the face values must be obtained to atleast second-order accuracy and a lower-order accurate method would defeat the purpose of defect correction. In the current study,

we use a linearity preserving pseudo-Laplacian approach [66] to transfer the centroidal values to the nodes and then average nodal values of each face to get the face values. The choice of such an approach for face value determination is motivated by the following results.

Theorem 3.2.3. *If a linearity-preserving pseudo-Laplacian is employed to estimate nodal velocity components from* b^{th} *order accurate centroidal velocity components, then the nodal velocities are accurate to order* $min(b, 2)$*. Furthermore, the face values obtained by simple averaging of the nodal values retain the same order of accuracy as the nodal values.*

Proof. The pseudo-Laplacian computes the nodal values φ_n from the centroidal values φ_i as,

$$\varphi_n = \frac{\sum_{i \in \mathcal{S}} w_i \varphi_i}{\sum_{i \in \mathcal{S}} w_i} \tag{3.16}$$

where, $\mathcal{S}$ is the set of volumes surrounding (shared by) the node n. The weights can be written as a perturbation about unity as $w_i = 1 + \Lambda \cdot (\mathbf{x_i} - \mathbf{x_n})$ and the vector Λ is calculated so that the weights satisfy the principle of linearity preservation. This defines a system of d linear equations (in d dimensions) given by,

$$\sum w_i (\mathbf{x}_i - \mathbf{x}_n) = \mathbf{0} \tag{3.17}$$

which can be solved easily for Λ and hence w_i. Rewriting the centroidal values in terms of the “exact" nodal values using truncated Taylor’s series gives,

$$\varphi_i^e = \varphi_n^e + \nabla \varphi_n^e : (\mathbf{x}_i - \mathbf{x}_n) + \mathbf{O}(||\mathbf{x}_f - \mathbf{x}_i||^2) \tag{3.18}$$

Also,

$$\varphi_i = \varphi_i^e + \mathbf{O}(h^b) \tag{3.19}$$

Simplification after substitution of Eqs. (3.17), (3.18) and (3.19) in Eq. (3.16) result in,

$$\varphi_n = \varphi_n^e + \mathbf{O}(h^{min(b,2)}) \tag{3.20}$$

which is a statement on the order of accuracy of the nodal values. The face values are obtained by simple averaging as,

$$\varphi_f = \frac{\sum_N \varphi_n}{N} \tag{3.21}$$

where, N is the number of nodes constituting the face. Writing the nodal values in terms of the “exact" face values and realizing that the order of accuracy of the nodal values is itself equal to $min(b, 2)$ gives,

$$\varphi_f = \frac{\sum_N (\varphi_f^e + \nabla\varphi_f^e : (\mathbf{x}_f - \mathbf{x}_n) + ||\mathbf{x}_f - \mathbf{x}_n||^2)}{N} + \mathbf{O}(h^{min(b,2)}) \tag{3.22}$$

Recognizing that the values at the face are lumped at the face centroid and invoking the definition of the latter easily leads us to,

$$\varphi_f = \varphi_f^e + \mathbf{O}(h^{min(b,2)}) \tag{3.23}$$

which is the desired result. □

We remark here that the use of any other choice for the weights, such as the volume weighted averaging ($w_i = \Omega_i$) would lead to only first-order accurate face values and hence to first-order accurate reconstructed velocities by virtue of Theorem 3.2.3. We shall demonstrate the importance of the nodal computation strategy and its effect on the reconstruction accuracy in the later sections. Interestingly, it is easy to see that the IDeC(k)-GG reconstruction to obtain centroidal velocities requires the gradients of these velocity components that in turn, through the face values depend on the centroidal velocities themselves. This paradoxical situation is not surprising however and is resolved by the use of the iterative approach which at convergence yields consistent gradients as well as second-order accurate centroidal velocities provided the nodal values are computed to second-order accuracy as described by Theorem 3.2.1. The paradoxical nature of the reconstruction procedure is also reflected in [41] and is true of any similar implicit approach.

3.3 Accuracy studies

We investigate the accuracy and convergence of the IDeC(k)-GG reconstruction on different mesh topologies in this section and highlight the importance of linearity-preserving pseudo-Laplacian in the reconstruction. We choose the following two exact vector fields for this investigation, where Case 1 represents a parabolic velocity profile similar to the 2-D channel flows and Case 2 is typical of incompressible flows and has also been studied in [41].

$$Case\ 1 : u = 1 - y^2, v = 0$$

$$Case\ 2 : u = e^y \cos(x), v = e^y \sin(x)$$

The accuracy studies are performed on a [-0.25,0.25]$\times$[-0.25,0.25] square domain, with computations done on three progressively refined grids starting from the initial grid. The grid topologies are shown in Figure 3.1 and the exact face normal velocities are prescribed at the faces for the accuracy studies.

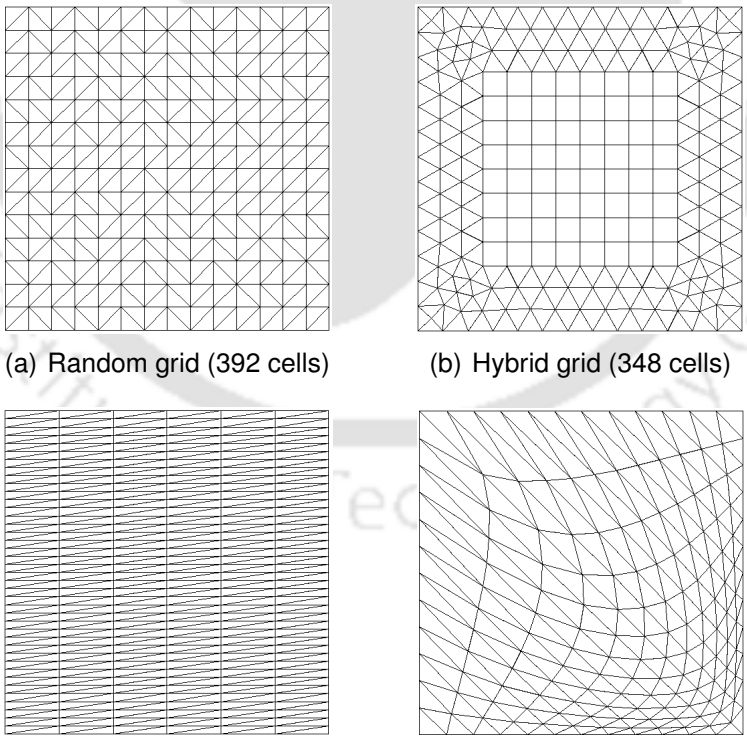

(a) Random grid (392 cells) (b) Hybrid grid (348 cells)

(c) Skewed grid (480 cells) (d) Distorted grid (288 cells)

Figure 3.1: Grid topologies for the accuracy studies.

Figure 3.2 presents the L_∞ norm of error in reconstructed velocities on the four grid

topologies using IDeC(k)-GG reconstructions. It is clear that the error decreases at a rate close to two for both test fields independent of the grid topology, demonstrating the generic nature of the proposed higher-order reconstruction. The IDeC(k)-GG and IDeC(1)-GG reconstructions are compared by studying the error decay for Case 2 on progressively refined meshes for a chosen grid topology. It is evident from Figure 3.3(a) that the reconstructed velocities from IDeC(1)-GG reconstruction are only first-order accurate, as opposed to the second-order accuracy resulting from IDeC(k)-GG reconstruction. The error in gradients of u-velocity for this case is also shown in

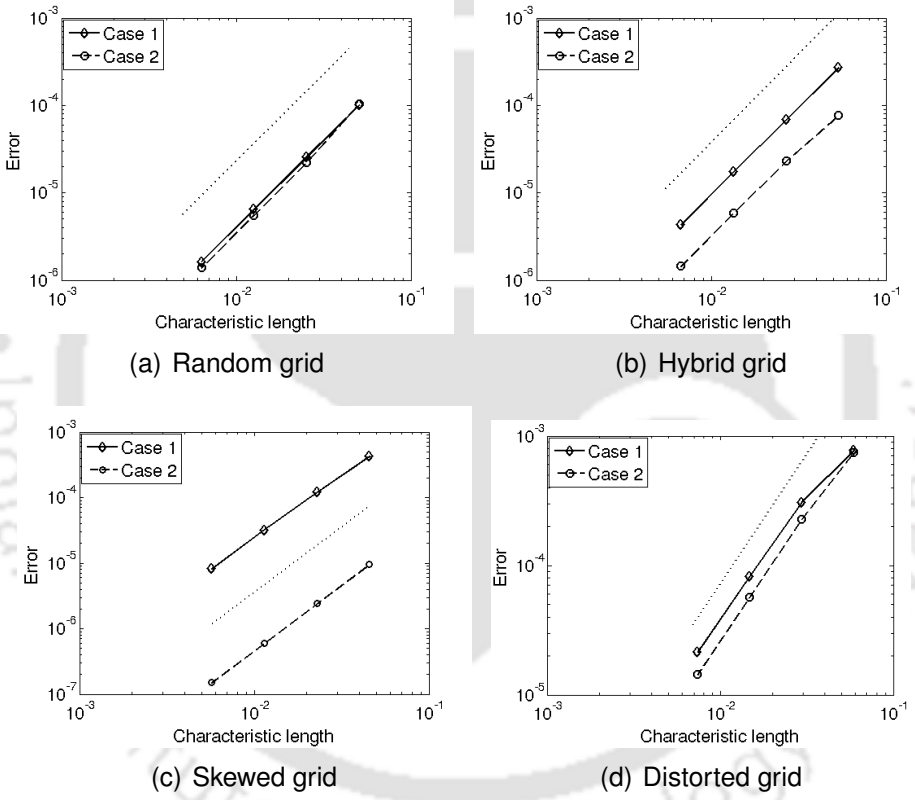

Figure 3.2: L_∞ norm of global error in velocity with uniform grid refinement on the four grid topologies for the two test cases. The dotted line has a slope of two.

Figure 3.3(b) and does not diminish with refinement when IDeC(1)-GG reconstruction is employed. As discussed in Section 3.3, the lower order accuracy of the Gauss reconstruction is attributed to the inconsistency of the gradients and this is shown to be led to physically inconsistent solutions (See Section 3.4). The importance of face-value determination in IDeC(k)-GG reconstruction is highlighted by comparing the error in reconstructed velocities as well as velocity gradients with mesh refinement when using

volume weighting as well as linearity-preserving weights for computing nodal values. Figure 3.4 shows that while volume-weighted averaging leads to inconsistent gradients and first-order accurate centroidal velocities despite the correction, gradients from the linearity-preserving pseudo-Laplacian approach are consistent and result in second-order accurate reconstructed velocities. These observations are in excellent agreement with the theoretical arguments presented in Theorems 3.2.1-3.2.3 and demonstrate the efficacy of the proposed IDeC(k)-GG reconstruction algorithm.

Studies are also performed on the convergence of the algorithm and its dependence on mesh size and topology. Table 3.1 shows the number of iterations to convergence on different grid topologies measured on the finest mesh and Figure 3.5 shows the convergence history [1] of the IDeC(k)-GG reconstruction on two grid topologies when Case 1 is studied. The number of iterations for convergence is roughly 10 and is nearly independent of the mesh topology and refinement. This study further underlines the robustness and utility of the proposed algorithm on arbitrary polygonal meshes in two dimensions.

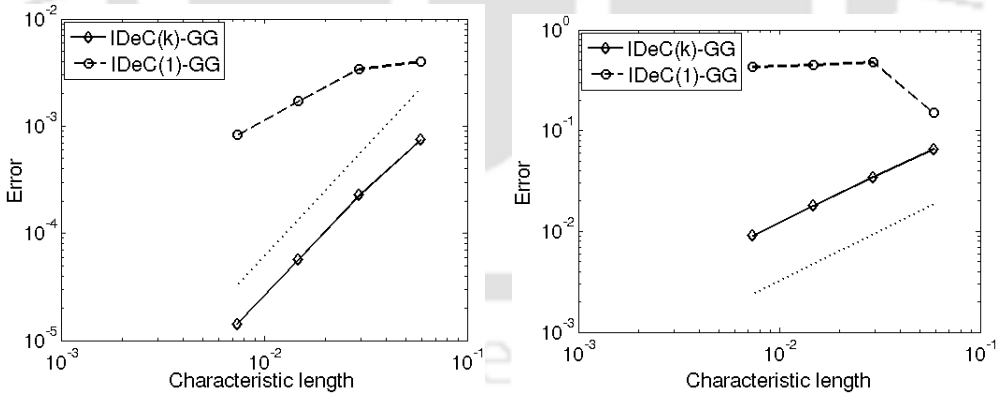

(a) Error in velocity (b) Error in gradient

Figure 3.3: L_∞ norm of error in velocity and gradient calculation on distorted mesh for Case 2.

[1] The time is measured using the intrinsic function “CPU_time" and the data shown is average over several runs on each grid.

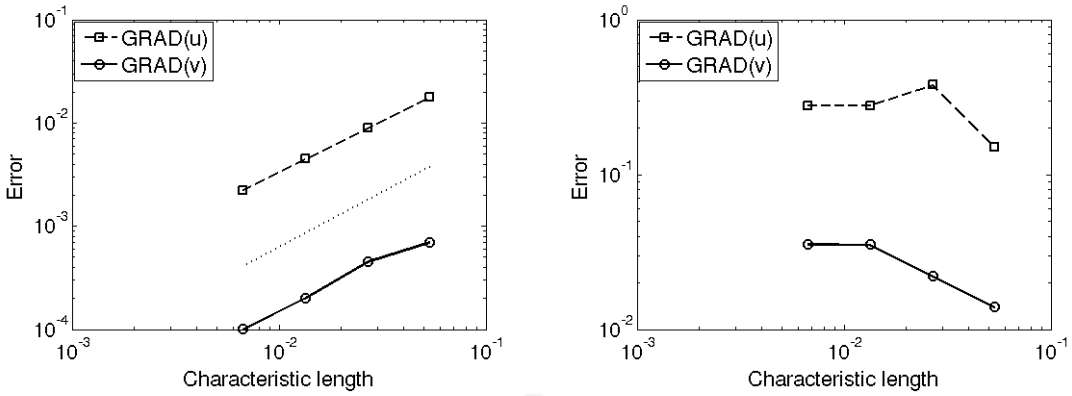

(a) Linearity preserving weight (b) Volume weight

Figure 3.4: L_∞ norm of error in gradients on hybrid mesh when calculated using (a) linearity preserving weight and (b) volume weight for Case 2.

Table 3.1: Number of iterations for convergence of IDeC(k)-GG reconstruction on different mesh topologies for Case 1.

Grid topology	Number of iterations
Random	11
Hybrid	11
Skewed	8
Distorted	11

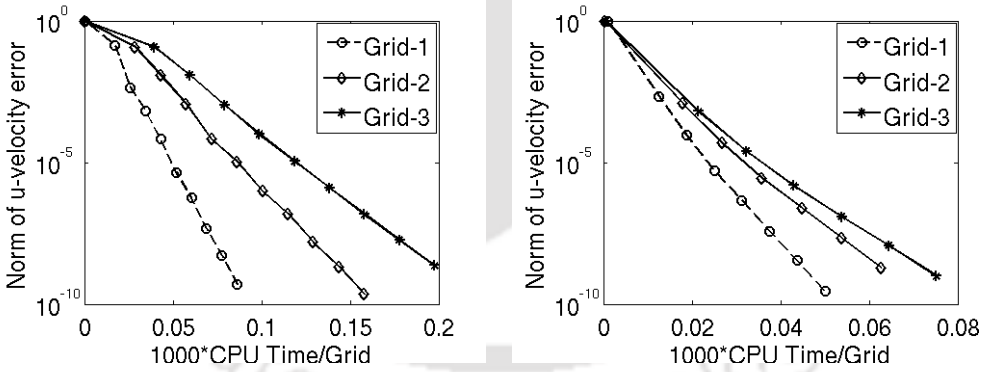

(a) Hybrid (b) Skewed

Figure 3.5: Convergence history of IDeC(k)-GG reconstruction on hybrid and skewed grids for Case 1 with progressive mesh refinement in the order Grid-1, Grid-2 and Grid-3.

3.4 Studies using IDeC(k)-GG and IDeC(1)-GG

In this section after the implementation of the reconstruction algorithm into the existing solver we perform numerical studies in incompressible non-Newtonian flows using IDeC(1)-GG and IDeC(k)-GG reconstruction to know their effect on the physical solu-

tion. In this study we have chosen power-law (both shear thinning and shear thickening) and Carreau family of models which are described in Chapter 2.

3.4.1 Two-dimensional channel flow

The flow of power-law fluids through a two-dimensional channel of unit width is studied at $Re = 100$. A portion of the discretised mesh (17000 cells) is shown in Figure 3.6. The computational domain is chosen to be 30 units long so as to ensure fully-developed flow at the outlet. An uniform velocity is prescribed at the inlet and studies are performed using IDeC(1)-GG and IDeC(k)-GG reconstructions. Figure 3.7 shows the comparison between the velocity profiles obtained using both reconstructions along with the analytical solution for a power-law exponent of n = 0.8. No discernible difference between the reconstructions is evident. Studies with $n = 1$ (Newtonian fluid) also lead to similar conclusions and is not shown here for sake of brevity. Interestingly, the computed pressure drop across the channel using both approaches for the Newtonian case were also nearly identical. While this study seems to suggest that the IDeC(1)-GG reconstruction suffice to obtain solutions for laminar, incompressible flow of non-Newtonian fluids, the numerical experiments that follow reveal that this is indeed not the case. The agreement between the results of the two reconstructions observed for this study is rather fortunate and the reasoning for this agreement is discussed later in this section.

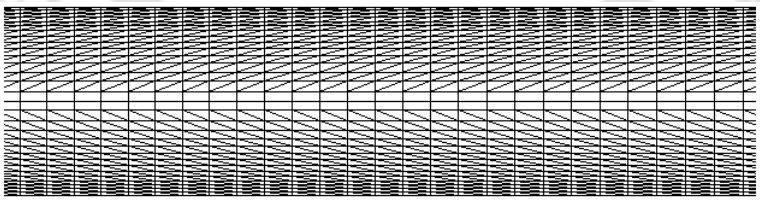

Figure 3.6: Triangulated and quadrilateral (at the center) meshes used for the computation.

3.4.2 Lid driven cavity flow

The lid driven cavity flow is a benchmark problem studied by several researchers for incompressible Newtonian flows. In this study, we investigate its non-Newtonian coun-

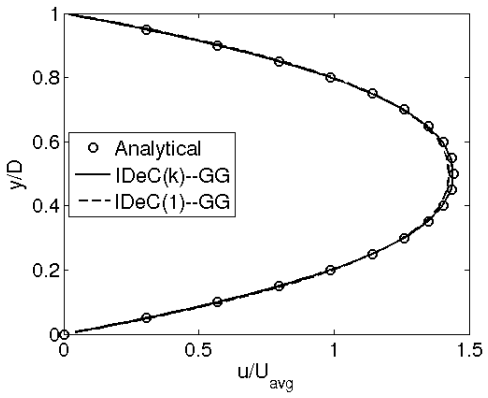

Figure 3.7: Velocity profile plot of downstream using IDeC(k)-GG and IDeC(1)-GG and compared with analytical solution.

terpart using shear-thickening and shear-thinning power-law fluids as in [12, 67]. The computational domain is $[0, 1] \times [0, 1]$ and the Reynolds number based on the lid velocity is 100. Non-Newtonian exponents of $n = 0.75$ and $n = 1.5$ are chosen for shear-thinning and shear-thickening fluids respectively, and the domain is meshed using a triangulated Cartesian grid with 3200 cells. The centerline velocity profiles obtained using IDeC(1)-GG and IDeC(k)-GG reconstructions for the shear-thickening fluid are compared with the results of Bell and Surana [67] in Figure 3.8. The results of the defect-corrected Gauss reconstruction agree reasonably well with the benchmark computations unlike those of Gauss reconstruction without defect correction which show a considerable deviation in the velocity profiles. This is reflected also in the streamline plots shown in Figure 3.9, which are completely dissimilar. It is interesting to note that that the IDeC(1)-GG reconstruction predicts a wrong vortex structure and a greater disparity in the size of corner vortices as compared to the IDeC(k)-GG reconstruction. It must be remarked that in employing either reconstruction, the numerical solution were obtained at steady state and the divergence was close to machine zero. This indicates that while both solutions are numerically consistent, only the computations of IDeC(k)-GG reconstruction leads to a physically consistent simulation. These arguments apply equally well for the shear-thinning fluid, for which the results are compared with the computations of Neofytou [12] and are presented in Figure 3.10. The differences in streamline pattern shown in Figure 3.11 for this case is more striking, showing a perceptible shift in the primary vortex and disappearance of a secondary corner vortex

when lower-order accurate reconstruction is employed.

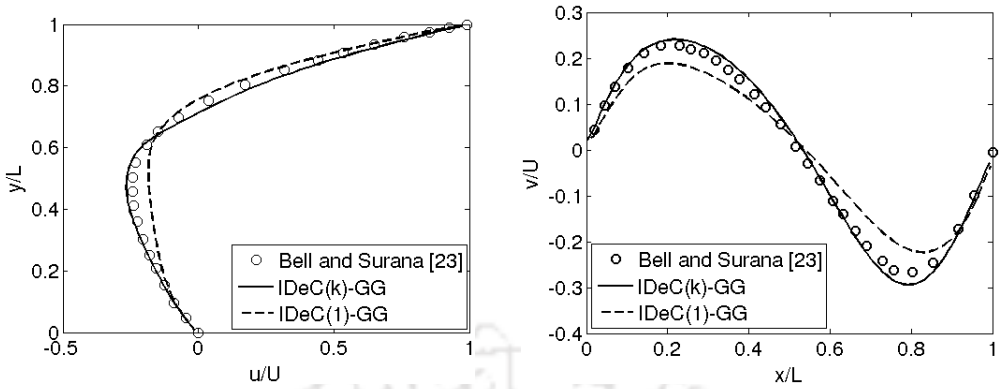

(a) u-velocity profile (b) v-velocity profile

Figure 3.8: Centerline velocity profiles at $Re = 100$ and $n = 1.5$.

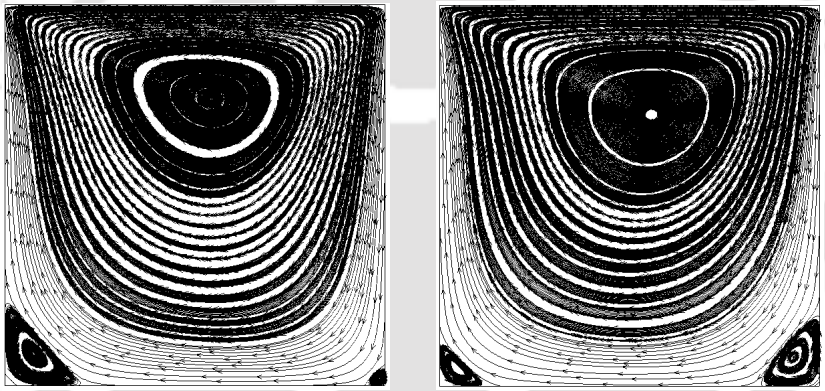

(a) IDeC(1)-GG reconstruction (b) IDeC(k)-GG reconstruction

Figure 3.9: Streamline patterns at $Re = 100$ and $n = 1.5$.

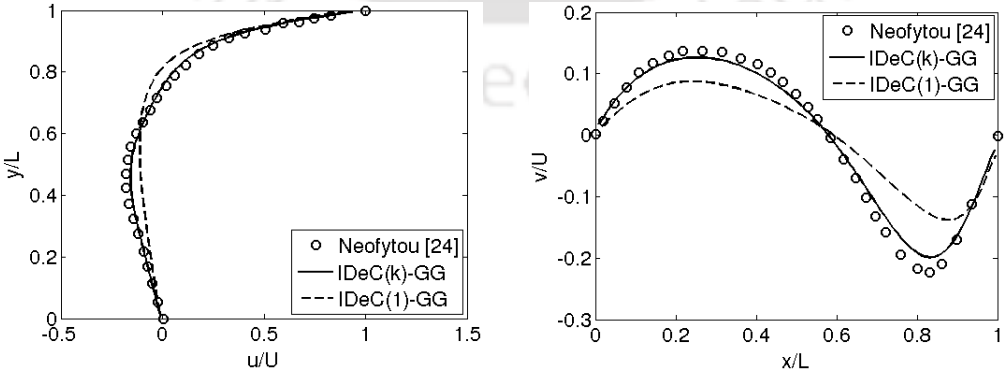

(a) u-velocity profile (b) v-velocity profile

Figure 3.10: Centerline velocity profiles at $Re = 100$ and $n = 0.75$.

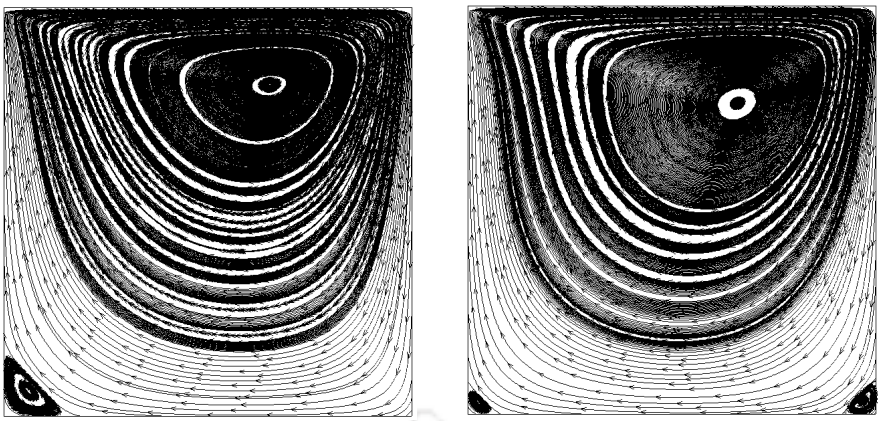

(a) IDeC(1)-GG reconstruction (b) IDeC(k)-GG reconstruction

Figure 3.11: Streamline patterns at $Re = 100$ and $n = 0.75$.

3.4.3 Backward facing step in a channel

The laminar flow over a backward facing step is investigated using the IDeC(1)-GG and IDeC(k)-GG reconstructions using the Carreau-Bird model. Figure 3.12 shows the computational domain [0,30]$\times$[0,1.9423] employed in the study which is discretised using a hybrid mesh with 20550 cells as shown in Figure 3.13. A fully developed power-law velocity profile is imposed at the inlet and velocities are extrapolated at the outlet, ensuring global mass conservation. Simulations have been performed for three different values of Reynolds number for which the flow remains laminar as shown in Table 3.2. It is clear from Table 3.2 as well as Figure 3.14 that the predictions of the recirculation zone lengths from the IDeC(1)-GG reconstruction do not compare well with the computations of Choi and Barakat [13], in contrast to the results using IDeC(k)-GG reconstruction which show a reasonable agreement. We emphasise that as in the driven cavity problem, the computed solutions when using either reconstruction are obtained at steady state and there is no mass loss which guarantees local mass conservation.

Numerical investigations on lid driven-cavity flow and flow over the backward-facing step indicate that while both IDeC(1)-GG and IDeC(k)-GG reconstruction lead to results that are steady and satisfy the discrete continuity criterion, the solutions are markedly different in both cases. Comparisons with benchmark data show that the IDeC(1)-GG

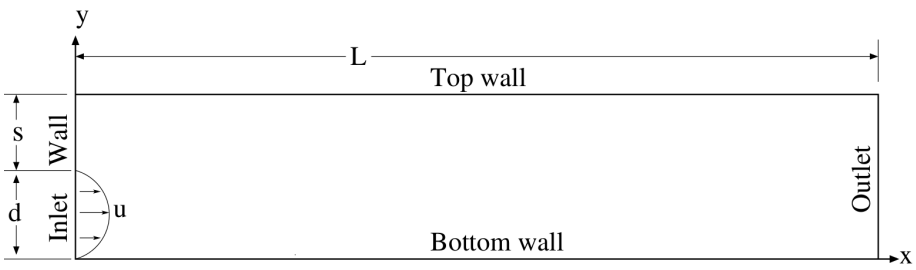

Figure 3.12: 2-D geometry of backward facing step.

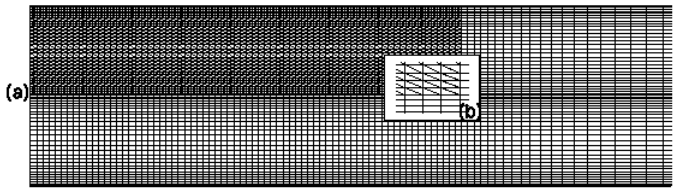

Figure 3.13: Hybrid mesh used for the computation. Part (b) shows the zoom in view of the hybrid mesh.

Table 3.2: Recirculation length for IDeC(1)-GG, IDeC(k)-GG and the literature using Carreau fluid model.

Parameters used	Recirculation length		
	IDeC(1)-GG	IDeC(k)-GG	Choi and Barakat [13]
$Re = 100$, Wi=108	0.98	1.29	1.39
$Re = 300$, Wi=322	4.24	4.88	4.77
$Re = 400$, Wi=430	6.05	6.46	6.33

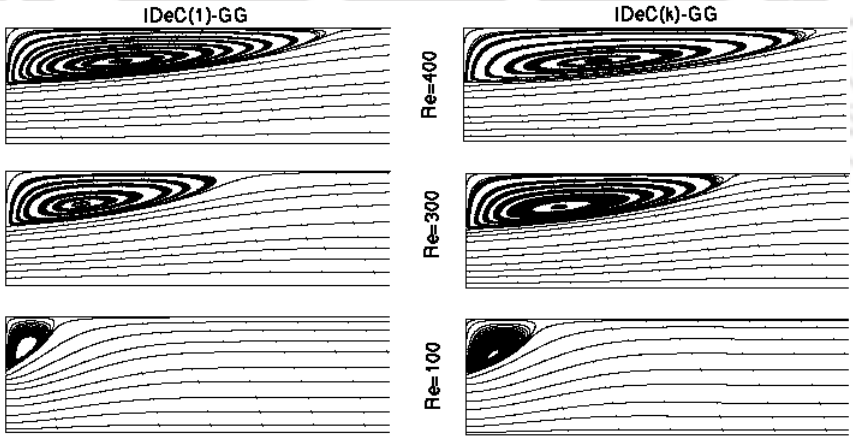

Figure 3.14: The streamline pattern obtained using the two reconstruction approaches.

leads to spurious solutions and this is attributed to the lower-order accuracy of the reconstructed velocity field. The viscous fluxes are dependent on the gradients of the velocity field which are inconsistent when IDeC(1)-GG reconstruction is employed. It is important to realise that these flows are diffusion-dominated as Reynolds numbers are small (in the laminar regime) and the viscous fluxes play a major role for such

flows. A striking aspect of these flows, however, is that they are vorticity-dominated and vorticity generation is inherently linked to the viscous fluxes. The lack of consistency of the gradients using Gauss reconstruction without defect correction therefore, reflects as a numerically consistent but physically inconsistent solution for such flows. Defect correction enhances the order of accuracy of the reconstructed velocities and renders the gradients consistent and hence leads to flow patterns that are physically consistent. This also explains why the reconstructions behaved identically for the channel flow case; the flow was not vorticity-dominated and despite lower Reynolds numbers the flow pattern and pressure drop remain unaffected by the numerical inconsistency from the reconstruction.

3.4.4 Flow past circular cylinder

Conservation properties of any numerical schemes is indispensable criteria to guarantee the conservation of physical properties in the discrete sense. A scheme may mislead (giving spurious solution) us about a physical problem without this property is one of the major concerns of the ability of the underlying discretisation to conserve mass, momentum and energy at the discrete level. In order to explore if and how conservation or its lack thereof could lead to non-physical solutions on unstructured staggered meshes, we consider the flow of a shear-thinning power-law fluid ($n = 0.6$) past a circular cylinder of unit diameter at $Re = 40$. A schematic diagram of the problem is shown in Figure 3.15 where a hybrid mesh in a $[0, 30] \times [0, 15]$ computational domain is employed, with triangular cells in the cylinder vicinity and quadrilateral cells in the rest of the domain. Figure 3.16 shows a zoom in portion of the mesh encompassing the circular cylinder. The mass imbalance is studied by monitoring the discrete divergence of velocity field, while momentum conservation is investigated by computing the drag coefficient using a momentum balance method as well as direct integration of the pressure and viscous forces on the surface of the cylinder.

Figure 3.17(a) shows the time history of the maximum value of velocity divergence in the domain for the IDeC(k)-GG and the IDeC(1)-GG algorithms. It is easy to see that

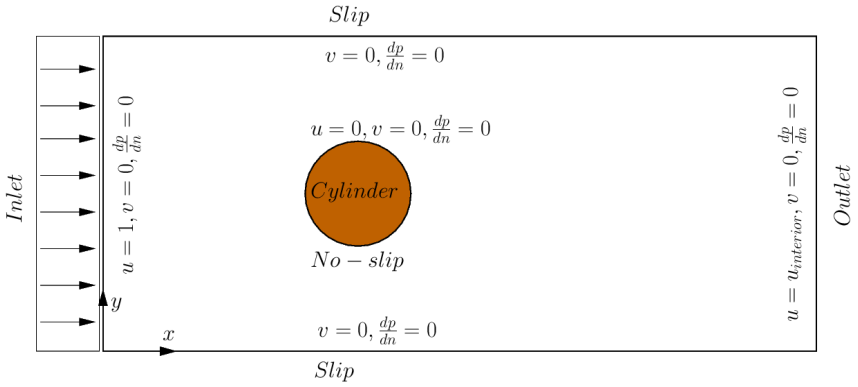

Figure 3.15: Schematic computational domain for a steady flow past a circular cylinder in the laminar flow regime.

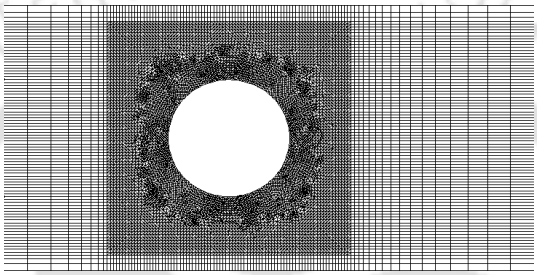

Figure 3.16: An enlarge view of the hybrid mesh in the computational domain surrounding the cylinder.

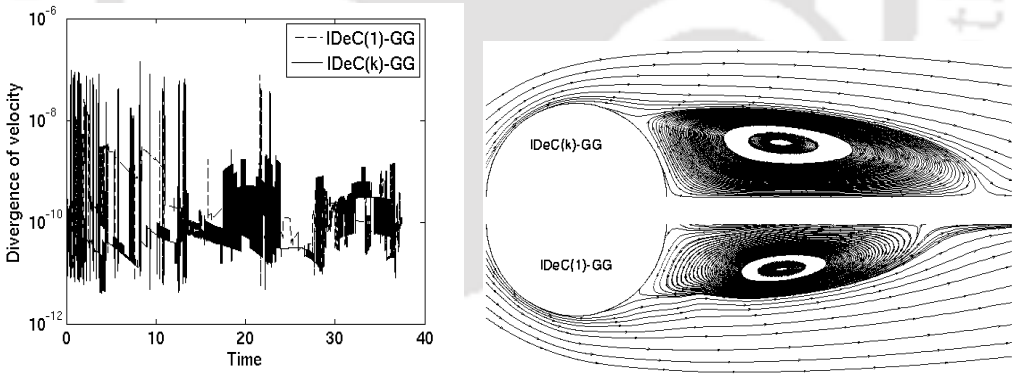

Figure 3.17: (a) Mass conservation with time to reach steady state solution and (b) streamline pattern of the flow past cylinder using IDeC(1)-GG and IDeC(k)-GG reconstructions.

the mean value of velocity divergence is appreciably small at all times and is around 10^{-10} at steady state, with and without defect correction, which ensures discrete mass conservation. The drag coefficient values calculated using global momentum balance (involving integrals on the domain boundary only) and direct surface force integration (involving integrals on the cylinder surface only) are tabulated in Table 3.3. It is easy

Table 3.3: Drag coefficient and recirculation length for the flow of shear-thinning power-law ($n = 0.6$) fluid past a cylinder at $Re = 40$. The computed values for the drag coefficient and recirculation length in [15] are 1.34 and 1.75 respectively.

Method used	Drag coefficient, C_d		Recirculation length	
	IDeC(1)-GG	IDeC(k)-GG	IDeC(1)-GG	IDeC(k)-GG
Momentum balance	1.53	1.37	1.41	1.75
Surface integration	1.51	1.36	1.41	1.75

to realise that the drag coefficient calculation using the two different methods agree to within 0.5% accuracy for IDeC(k)-GG and IDeC(1)-GG reconstructions, indicating that the discretisation guarantees global momentum conservation. However, the IDeC(1)-GG approach, devoid of defect correction, overpredicts the drag coefficient and underpredicts the recirculation length, as compared to the computed results of Sivakumar et.al. [15]. The results in the latter, which were obtained using a commercial finite-volume based continuum solver, are in good agreement with the IDeC(k)-GG results. These studies conclusively prove that whilst both IDeC(k)-GG and IDeC(1)-GG are discretely conservative, the lower order accuracy of the latter is solely responsible for physically inconsistent solutions as is evident in the distinctly shorter recirculation bubble observed in Figure 3.17(b).

3.5 Summary

A new velocity reconstruction algorithm, referred to as IDeC(k)-GG reconstruction, which reconstructs centroidal velocities to second order accuracy from face-normal data on arbitrary polygonal staggered meshes is proposed. The conditions that guarantee the second-order accuracy of the velocity reconstruction are derived and its efficacy on arbitrary polygonal mesh topologies is demonstrated. The importance of the proposed algorithm for non-Newtonian flows on unstructured meshes is elucidated through numerical simulations of driven cavity and backward facing step problems with power-law and Carreau fluids. Numerical investigations show that second-order accuracy of the reconstructed velocity field is essential to obtain physically consistent

solutions of vorticity dominated flows typical of hemodynamic simulations. It is demonstrated that the causality of spurious solutions are not linked to discrete conservation and arise solely due to the lower order accuracy of velocity reconstruction.

Chapter 4

Validation studies

In this chapter, we assess the computational framework developed in the previous chapters using canonical test cases involving steady and unsteady flows. Studies on spatial-temporal accuracy on unstructured meshes as well as the discrete conservation properties are studied. Investigations are carried out using different non-Newtonian models and mesh topologies to highlight the efficacy of the proposed framework.

4.1 Background

The foremost task in the development of a computational framework is validation against analytical solutions or well established experimental or/and numerical data in literature. While there are extensive studies for Newtonian fluid flows in the incompressible laminar flow regime, only few numerical benchmark problems are available for non-Newtonian flows. We employ a range of test problems in both external and internal flows which span those with simple analytical solutions to those with purely computational benchmarks that account for the non-linear behaviour of viscosity. We also discuss the accuracy of the solver on arbitrary polygonal meshes and investigate the discrete conservation property of the framework since the control volumes are overlapping unlike conventional finite volume approach.

4.2 Accuracy study

We study the spatial and temporal accuracy of the flow solver by considering a Newtonian flow problem that has an exact solution to the Navier-Stokes equations. This test case consists of periodic counter-rotating decaying vortices and we consider a computational domain [-0.25,0.25]×[-0.25,0.25] with exact solution prescribed at the boundaries. The exact flow field at any time is given by [68],

$$
\begin{aligned}
u &= -\ \cos(2\pi x)\ \sin(2\pi y)\ e^{-\frac{8\pi^2}{Re}t} \\
v &= \ \sin(2\pi x)\ \cos(2\pi y)\ e^{-\frac{8\pi^2}{Re}t} \\
p &= -\frac{1}{4}\left(\cos(4\pi x) + \sin(4\pi x)\right)\ e^{-\frac{16\pi^2}{Re}t}
\end{aligned}
$$

The solution is dependent on time and space, therefore it can be used to assess the temporal and spatial accuracies of the flow solver using separate experiments. It must be emphasised here that since the velocities at the boundaries are prescribed (Dirichlet condition), the gradient of pressure correction on the boundaries are set to zero (Neumann condition). We solve the governing equations upto a time of $t = 0.2$ at $Re = 100$ and compute the errors in velocity and pressure (difference between analytical and numerical solutions) in the L_∞ norm.

4.2.1 Temporal accuracy

This test is performed considering four progressively refined time steps 0.01, 0.005, 0.0025, and 0.00125 for a sufficiently fine mesh. The mesh chosen for this study is a hybrid mesh with 348 finite volumes. The solution using a very small time step $\Delta t = 0.0001$ is considered as the reference solution for error analysis. This strategy is adopted to remove the spatial errors that can contaminate the total error and affect the temporal accuracy. It is easy to see from Figure 4.1 that the error norms of the pressure and the velocity fields versus time steps fall with a slope of 2. This implies that the present computational solver is second order accurate in time which is not

surprising given that the temporal integration adopted is a second-order accurate three point backward differencing scheme.

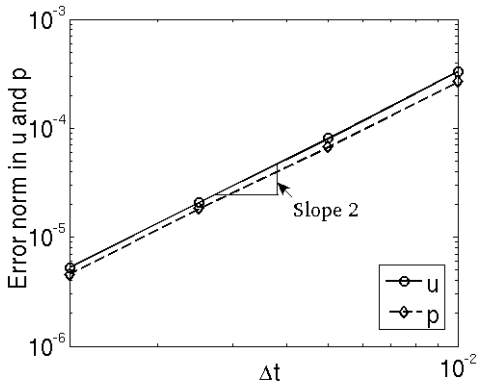

Figure 4.1: Temporal accuracy using the Taylor-Green vortex decay test on hybrid meshes.

4.2.2 Spatial accuracy

We now consider the spatial accuracy study on hybrid meshes at the given Re and choose a sufficiently small time step $\Delta t = 10^{-3}$. Three levels of progressive mesh refinement is carried out starting from the initial hybrid mesh topology with 348 cells as shown in the Figure 4.2. We compute the L_2 norm of error for the flow variables which is presented in Figure 4.3. It must be remarked that mean pressure (of the domain) is subtracted from the numerical solution of pressure field before calculating its error norm. This is because the pressure is only determined to an additive constant owing to the homogeneous Neumann boundary condition for pressure at the boundaries. It can be easily observed from Figure 4.3 that the error norm of the resultant velocity and pressure field fall with a slope close to 2 and 1 respectively. This is consistent with previous studies where the pressure shows one order lesser rate of convergence than the velocities. Clearly, one can argue that the solver is nominally second-order accurate on hybrid grids and a similar order of accuracy is observed on other mesh topologies as well (but not shown here for brevity). Even though the accuracy study has been performed for Newtonian fluid (since the analytical solution is only available for this case), we can speculate that the order of accuracy of the present numerical

solver would not be very different even when non-Newtonian fluid flows are considered.

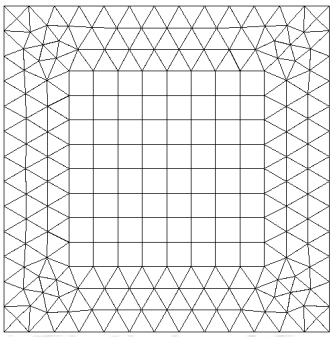

Figure 4.2: The discretised computational domain using hybrid mesh.

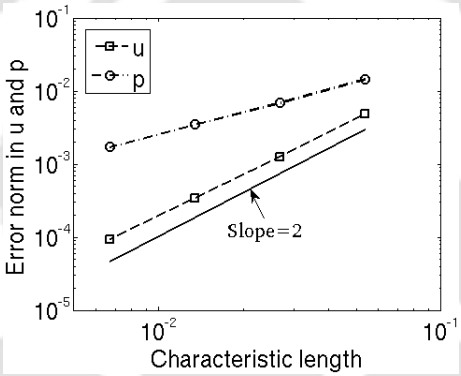

Figure 4.3: Spatial accuracy using the Taylor-Green vortex decay test study in hybrid meshes. The solid line with slope equal to two is the reference line.

4.3 Poisson equation and preconditioning

We employ an algebraic-multi-grid (AMG) preconditioner along with a Krylov solver for solving the Poisson equation in the proposed framework. In order to highlight the importance of this choice as opposed to the more common incomplete-lower-uppertriangular (ILU) preconditioner, we consider the case of an impulsively started channel flow as discussed also by Ge and Sotiropoulos [43]. We consider a square channel geometry with a [0,1]$\times$[0,1] domain to investigate the impulsively started laminar flow of power-law fluid with $n = 0.8$ at $Re = 100$. We use a time step of $\Delta t = 0.001$ and carry out simulations for just a single time step. The inlet is given a uniform velocity profile while

the domain is initialised with zero velocity. Three triangulated meshes, $G1$ (200 initial cells), $G2$ (see Figure 4.4) and $G3$ with aspect ratios 1, 10 and 100 respectively have been used. The motive of this study is to understand the effect of convergence of the Poisson solver for this test case using ILU and AMG preconditioners in conjunction with the FGMRES solver for the linear equations. The high aspect ratio grids are representative of high Reynolds number simulations, although such simulations have not been attempted in the present study. Figure 4.5 shows the performance of the FGM-

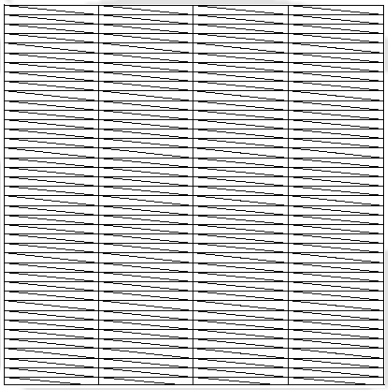

Figure 4.4: Zoom in view of the computational domain $G2$.

RES solver to solve the incompressible pressure Poisson equation preconditioned by AMG and ILU. It is easy to understand from the Figure 4.6 that AMG preconditioned FGMRES solver converges with fewer number of iterations as opposed to the ILU preconditioned FGMRES solver for a given tolerance convergence criterion. Importantly, the number of iterations increase nearly linearly with aspect ratio when ILU preconditioner is used but remains relatively constant (it increases from around 12 to less than 25) when AMG preconditioner is employed. This anisotropic coarsening strategy embedded into the AMG preconditioner makes it an ideal choice for solving Poisson equation (such as the pressure correction equation) on unstructured meshes and is therefore adopted in the present study as well. The AMG preconditioned FGMRES solver gives a fast convergence with the number of iterations weakly depending on the grid topology, skewness and aspect ratio.

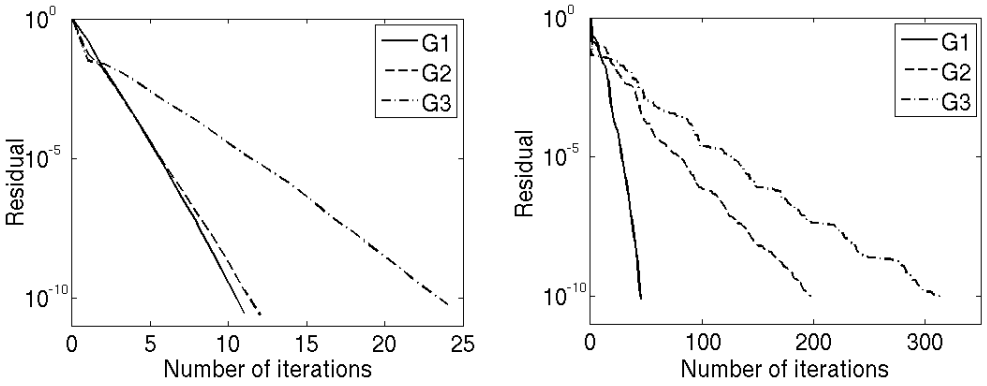

(a) AMG (b) ILU

Figure 4.5: Convergence history using the two preconditioners in skew meshes with different aspect ratios for a given tolerance of 10^{-10}.

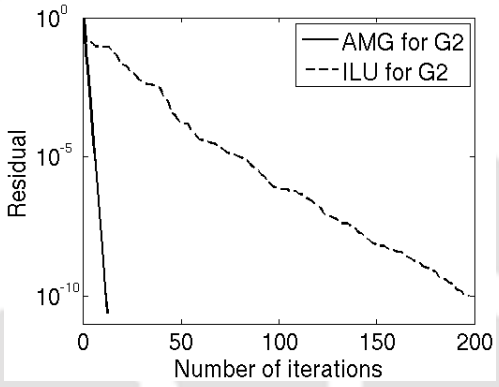

Figure 4.6: Convergence history using the two preconditioners in $G3$ with aspect ratio 10 for a given convergence criterion.

4.3.1 A note on discrete conservation

In this section, we investigate the discrete conservation of mass and momentum for the staggered/non-staggered finite volume approach introduced in this thesis. This exercise assumes significance because the momentum control volumes do overlap and it is not obvious whether the discrete conservation property of the conventional finite volume approach translates to this framework as well. We consider the two-dimensional channel flow for the shear-thinning ($n = 0.8$) power-law fluid for which the analytical solutions can be easily derived for the fully developed axial velocity profile

(u) and shear stress (τ_{xy}) as,

$$u = \frac{2n+1}{n+1}\left(1 - (|2y-1|)^{\frac{n+1}{n}}\right) \tag{4.1}$$

$$\tau_{xy} = -\frac{2^n}{Re}\left(\frac{2n+1}{n}\right)^n (2y-1) \tag{4.2}$$

For this study, height and average velocity of the channel are chosen as the reference length and velocity respectively. The simulation is performed at $Re = 100$ in a computational domain $[0, 40] \times [0, 1]$ that is discretised using non-uniform quadrilateral cells (15000) resolving the boundary layers. Figure 4.7 shows the history of maximum velocity divergence in the domain where one can see that the maximum net mass flux of the order of 10^{-9} indicating local mass conservation at all times and not just at steady state. Furthermore, local mass conservation would automatically imply global mass conservation as well. However, one must note that the control volume for the continuity equation is a single cell as opposed to the union of two cells for the normal momentum equation. Comparison in Figures 4.8(a) and (b) depict quantitative agreement between the analytical and numerical solutions for the u-velocity profile and shear stress respectively. This provides an indirect numerical evidence that the framework conserves momentum at the discrete level despite overlapping control volumes.

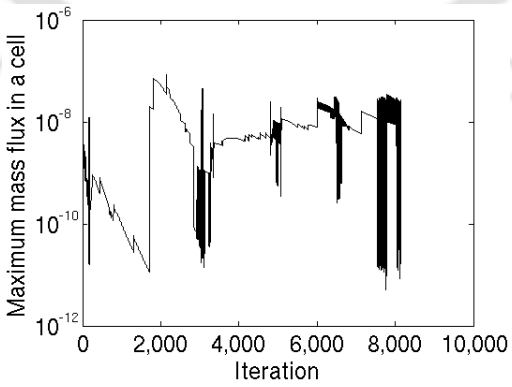

Figure 4.7: Local mass conservation in a cell until the steady state solution is reached.

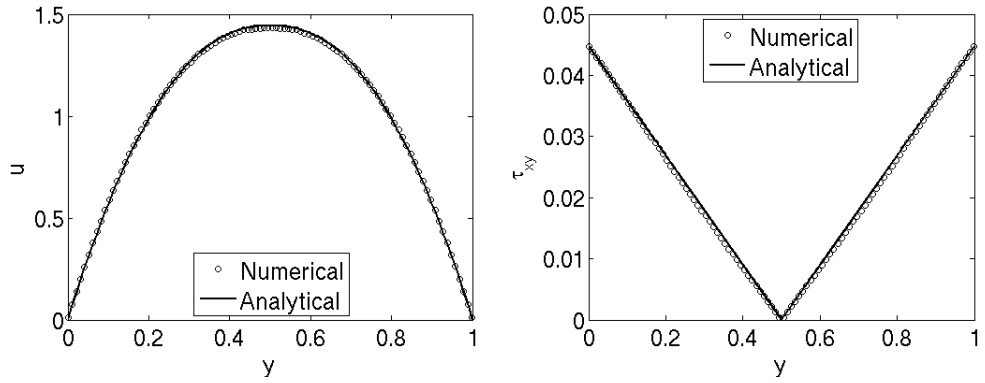

(a) Axial velocity profile (b) Shear stress (absolute value)

Figure 4.8: Comparison of the analytical solutions to the numerical results at $Re = 100$ and $n = 0.8$ using power-law fluid model.

4.4 Lid-driven cavity flow

We begin the validation studies by considering the lid driven cavity flow which is one of the extensively studied problems for incompressible Newtonian flows. We however simulate non-Newtonian flows using the power-law and Carreau-Yasuda fluid models in a square cavity. The hybrid mesh shown in Figure 4.9 in a computational domain [0,1]$\times$[0,1] with 6332 number of cells is used for the current investigations. The Reynolds number based on the lid velocity is 100 for the power-law fluids. Non-

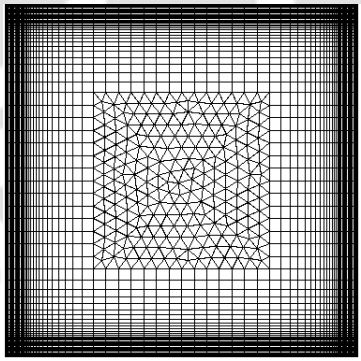

Figure 4.9: The hybrid mesh used to simulate the non-Newtonian flows inside the lid-driven square cavity.

Newtonian exponents of $n = 0.75$ and $n = 1.5$ are chosen for shear-thinning and shear-thickening fluids respectively using the power-law fluid model. Figure 4.10 shows the centerline velocity profiles for the shear-thinning and shear-thickening power-law fluid model which compares well with the results of Bell and Surana [67]. The validation of

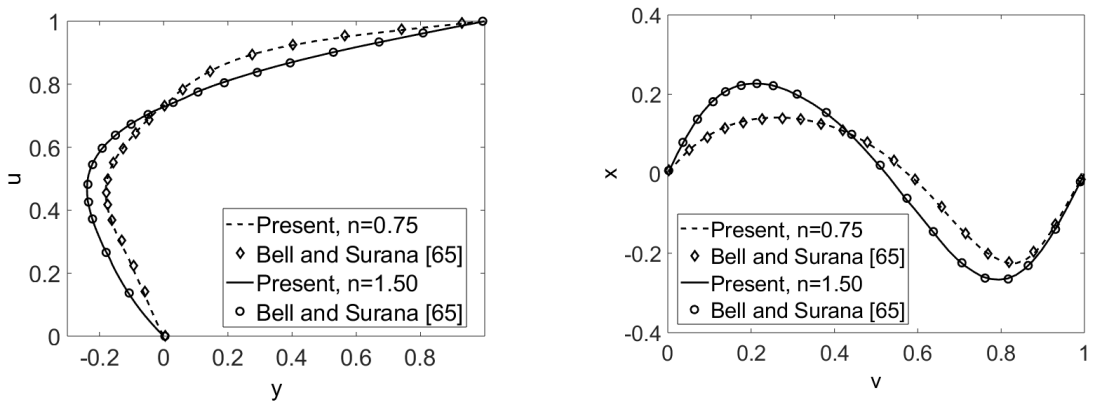

(a) u-velocity profile (b) v-velocity profile

Figure 4.10: Centerline velocity profiles of the lid-driven cavity flow using power-law fluid model with $n = 0.75$, $n = 1.50$ and $Re = 100$.

the Carreau-Yasuda model is made in an indirect manner by simplifying the viscosity relation as mentioned in Table 2.1. The modification is that the normalization of the apparent viscosity is done using μ_0 and we assume that $\mu_\infty/\mu_0 = 0$. The final simplified equation is derived as,

$$\mu = [1 + (\text{Wi } |\dot{\gamma}|)^a]^{\left(\frac{n-1}{a}\right)} \tag{4.3}$$

We have carried out two numerical test cases, at high Wi to validate the implementation of this model in the present computational framework as also pointed out in [69]. The model parameters of the Carreau-Yasuda fluids are listed in Table 4.1 where Reynolds number is defined as $Re = \rho U_{lid} H/\mu_0$. Figure 4.11 shows a good agreement

Table 4.1: Setting of flow parameters for the Carreau-Yasuda fluid model Lashckarbolok et al. [2014].

Parameters	Case 1	Case 2
Weisenberg number, Wi	10	10
Reynolds number, Re	56.23	316.23
Non-Newtonian exponent	0.75	1.5
Model constant	2	2

of the u and v-velocity profiles of present study with the published results of Bell and Surana [67]. It is not surprising to see this agreement since the Carreau-Yasuda fluid behaves like a power-law fluid for a large value of Wi ($Wi \gg 1$).

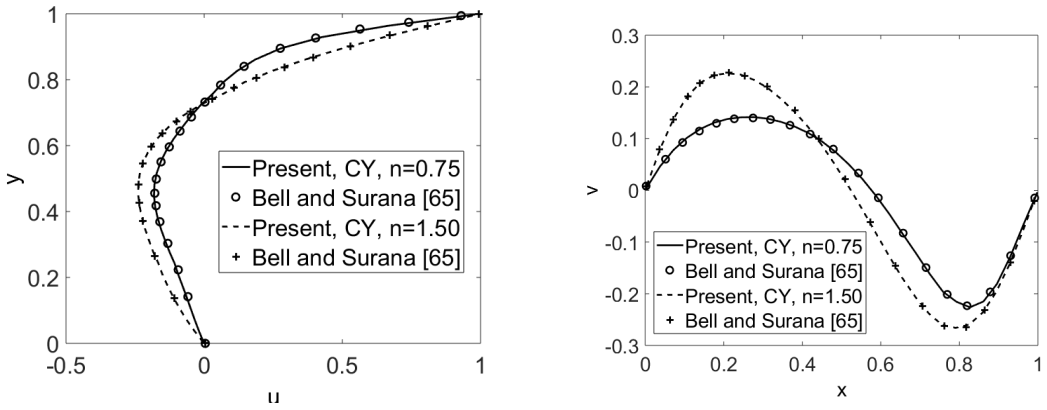

(a) u-velocity profile (b) v-velocity profile

Figure 4.11: Centerline velocity profiles of the lid-driven cavity flow using Carreau-Yasuda fluid model.

4.5 Two-dimensional channel flow

In this section, we simulate non-Newtonian flows through a two-dimensional channel using different fluid models. This is a test case that allows a test of inflow/outflow boundary conditions and also an analytical solution for a select number of cases. Figure 4.12 shows the discretised computational domain using triangular and quadrilateral cells with a flow domain size of [0,40]$\times$[0,1]. The number of cells in the domain are 17000. It is easy to obtain analytical solution of fully developed velocity profile in a two-

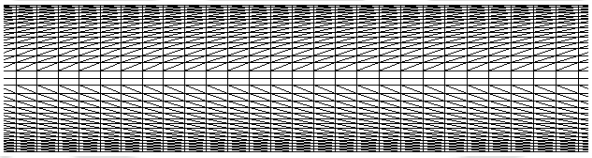

Figure 4.12: Discretised computational domain of the two-dimensional channel flow.

dimensional rectangular geometry for the power-law fluid model in the incompressible laminar flow regime. The flow of the power-law fluid model ($n = 0.8$ and $n = 1.2$) through the aforementioned geometry of unit width are studied at $Re = 100$. A uniform velocity is prescribed at the inlet so as to allow the flow to become fully developed in the sufficiently long channel. Figure 4.13 shows comparison of fully developed axial velocity profile obtained numerically with the analytical solution. No discernible difference is observed between the two results, highlighting the accuracy of the flow solver. The

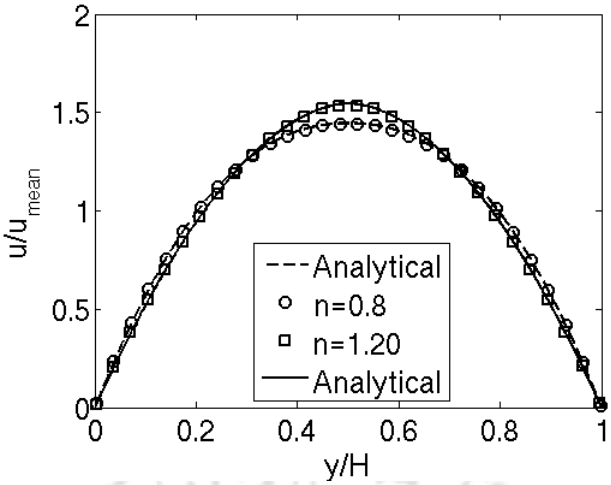

Figure 4.13: Fully developed axial velocity profiles for different power-law exponent ranging from shear-thinning to shear thickening fluids at $Re = 100$.

five parameter Carreau-Yasuda fluid model does not permit an analytical solution even for this simple test problem. Following the studies in Hao and Chao [70] which show that for a given set of the model parameters with $n = 0.3678$, Carreau-Yasuda model resembles the power-law model with $n = 0.708$, we use this Carreau model to effect an indirect comparison and validation of the implementation of the Carreau model in our framework. Figure 4.14 shows that the Carreau model (modified with a prescribed set of parameters) results in a velocity profile that agrees well with that obtained using shear-thinning power law fluid model and confirms both the proposition and validates the implementation of the Carreau model. Yet another numerical experiment is per-

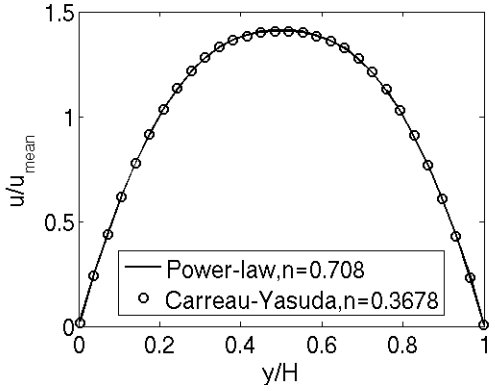

Figure 4.14: Fully developed axial velocity profiles using power-law and Carreau-Yasuda fluids at $Re = 100$, $Wi = 100$.

formed to validate the Carreau-Yasuda model by considering the pressure drop in the channel for three different Reynolds numbers. Ternik et al. [71] have demonstrated that the ratio of the pressure drop for the Newtonian fluid model to that of the Carreau-Yasuda fluid model roughly remains constant. Our results in Table 4.2 also support this fact and agrees closely with the ratio of 0.33 reported in [71] for the same flow and model parameters.

Table 4.2: Ratio of non-dimensional pressure drop of Newtonian to Carreau model.

Reynolds number	$\frac{\Delta P_N}{\Delta P_{CY}}$
150	0.3258
200	0.3300
250	0.3378

4.6 Backward facing step flow

The backward facing step is a canonical problem involving recirculation and is even more significant for hemodynamics since it can be considered as a geometry representative of stenosis which is a constriction in cardiovascular flow. In the present study, we perform simulations of steady laminar flow using Newtonian and Carreau fluid models in a backward facing step geometry. Figure 4.15 depicts the computational domain which is discretised using a hybrid mesh (see Figure 4.16) with 31540 cells. The comparison of the velocity profiles with the experiments of Armaly et al. [72] at two locations after the step are depicted in Figure 4.17 for the Newtonian fluid. Simulations have been carried out at three different Reynolds numbers (100, 200 and 400) which corresponds to Wi = 108, 322 and 430 respectively with the Carreau family of models (see Table 5.1 for model parameters) and the recirculation bubble length is compared with the results of Choi and Barakat [13] in Figure 4.18. We see that the comparison is excellent and the recirculation length increases with Reynolds number, consistent with streamline patterns shown in Figure 4.19.

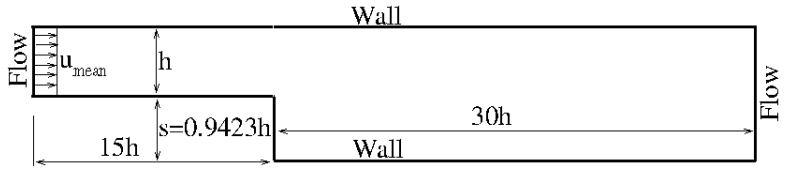

Figure 4.15: Computational domain, where h is the height of the inlet and s is the height of the step.

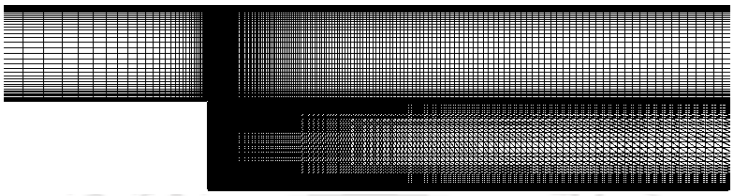

Figure 4.16: Enlarged view of discretisation of the computational domain near the step.

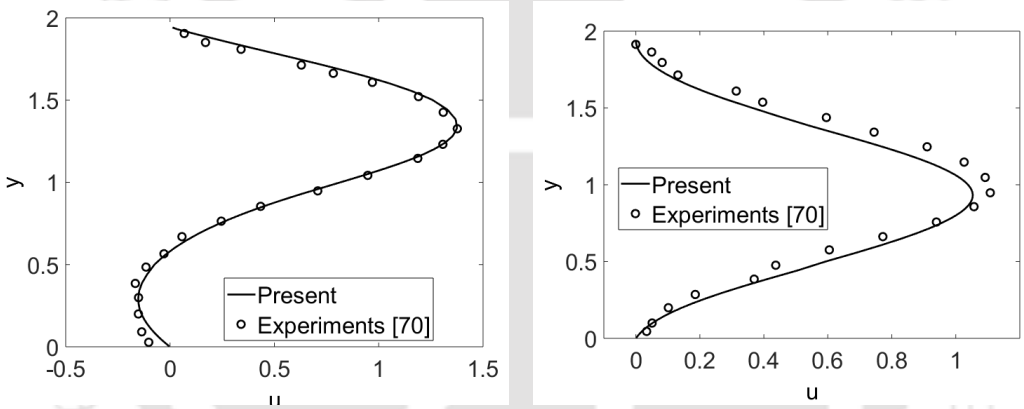

(a) $x/s = 2.55$ (b) $x/s = 7.76$

Figure 4.17: Variation of axial velocity fields in a direction normal to the flow at the two locations. Herein s is the length of the step.

4.7 Flow past a circular cylinder

The flow past a circular cylinder is a classical test case involving steady and unsteady external flow and is chosen as the final test case in the validation suite for the present flow solver. The Newtonian, power-law and Carreau-Yasuda fluid flows past a stationary as well as rotating circular cylinder of unit diameter (D) in the steady and unsteady laminar flow regime are simulated. The Reynolds numbers for the power-law and Carreau-Yasuda models are defined based on the diameter of the cylinder. Some of the important non-dimensional parameters for this test case are described below.

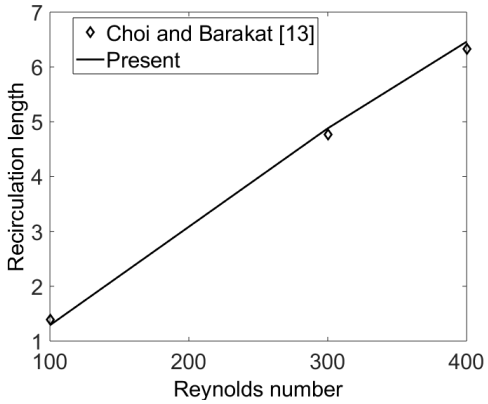

Figure 4.18: Comparison of the recirculation lengths with the reported literature data at the three Reynolds numbers with the corresponding values of Wi=108, 322 and 430.

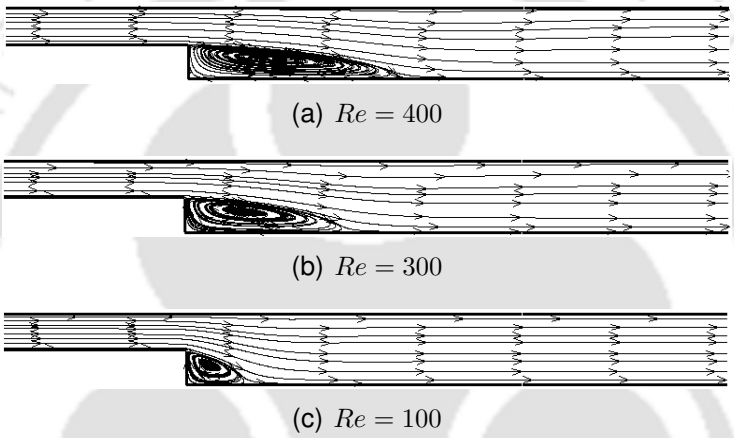

Figure 4.19: Streamline patterns using the Carreau fluid model for different Reynolds numbers.

- Rotational speed of the cylinder is defined as,

$$\beta = \frac{D\omega}{2U_\infty} \tag{4.4}$$

where, ω is the angular velocity of the circular cylinder and the rotating effect of the cylinder surface is obtained by setting the following Dirichlet boundary condition for velocities,

$$u_b = \beta\, n_{b,y}, \qquad v_b = -\beta\, n_{b,x} \tag{4.5}$$

where, $n_{b,x}$ and $n_{b,y}$ are the components of unit normal vector $\mathbf{n}_b$ of the cylinder

surface A.

- Recirculation (wake) length l_r.

$$l_r = \frac{l_c - 0.5D}{D} \tag{4.6}$$

where, l_c is the distance from the center of the cylinder to the point of reattachment (at the downstream of the cylinder and symmetry line with velocities $u = v = 0$).

- Drag C_d and lift C_l force coefficients.

$$C_d = \frac{2F_x}{\rho_\infty U_\infty^2 D},\ C_l = \frac{2F_y}{\rho_\infty U_\infty^2 D} \tag{4.7}$$

where, F_x and F_y are the forces contributing to drag and lift respectively comprising of the pressure and shear forces, and are calculated by the surface integration method over the cylinder surface and are obtained as,

$$F_x = \underbrace{\int_A p(A) n_{b,x} dA}_{\text{Pressure part}} + \underbrace{\int_A (\tau_{xx}(A)\ n_{b,x} + \tau_{yx}(A)\ n_{b,y}) dA}_{\text{Viscous part}} \tag{4.8}$$

$$F_y = \underbrace{\int_A p(A) n_{b,y} dA}_{\text{Pressure part}} + \underbrace{\int_A (\tau_{xy}(A)\ n_{b,x} + \tau_{yy}(A)\ n_{b,y}) dA}_{\text{Viscous part}} \tag{4.9}$$

where, dA denotes the elemental area of the cylinder surface A. Second order accurate pressure $p(A)$ is calculated at the boundary from the adjacent cell centroids to b, and the shear stress components $\tau(A)$ on the cylinder surface are obtained from the Eq. (2.3).

- Pressure coefficient at the cylinder surface C_p.

$$Cp = \frac{2(p - p_\infty)}{\rho_\infty U_\infty} \tag{4.10}$$

where, p and p_∞ are the pressures on the surface of the cylinder and the free

stream respectively.

- Time averaged drag $\bar{c}_l$ and lift $\bar{c}_d$ in the time interval ΔT.

$$\bar{c}_d = \frac{\int_{\Delta T} C_d \, dt}{\int_{\Delta T} dt}, \; \bar{c}_l = \frac{\int_{\Delta T} C_l \, dt}{\int_{\Delta T} dt} \tag{4.11}$$

The non-Newtonian exponents $n = 0.8$, $n = 1.0$ (Newtonian) and $n = 1.2$ are selected for the simulations using the power-law fluid model whilst for the Carreau-Yasuda fluid model is chosen as in [73]. A computational domain size [0,40]$\times$[0,20] with the center of the cylinder at $(10, 10)$ is discretised using hybrid mesh with triangular cells around the circular cylinder and quadrilateral cells in the rest of the domain. Figure 4.20 shows a zoomed view of the mesh around the circular cylinder.

We first consider simulations for both stationary and moving cylinder at $Re = 40$ using the power-law and Carreau-Yasuda fluid models. It must be noted that this problem does not have any benchmarks in literature for the Carreau fluid. We first perform simulations to study the effect of number of points at the cylinder surface and cells in the chosen domain on the coefficient of drag for the flow over stationary cylinder using the Carreau fluid model. A relative difference below 0.50% is observed in the coefficient of drag (C_{dp} + C_{dv}) for $NP = 130$ with corresponding number of cells $N_c = 22818$ of the domain and is utilised in all simulations since it gives a nearly grid independent solution. Figure 4.21 depicts the streamline patterns obtained using the two non-Newtonian fluid

Table 4.3: Grid convergence study based on the number of points (NP) at the cylinder surface with the associated number of cells (N_c) of the computational domain on the drag coefficients contributed from the pressure drag (C_{dp}) and viscous drag (C_{dv}), and their relative differences (RD) for the Carreau-Yasuda fluid model with the parameters: $Re = 40$, $n = 0392$, $\mu_0/\mu_\infty = 10$, $a = 0.644$, and $\lambda = 0.11$.

NP	N_c	C_{dp}	RD(%)	C_{dv}	RD(%)
40	13772	2.180	3.11	1.503	3.84
70	18394	2.217	1.47	1.534	1.85
100	21094	2.240	0.44	1.549	0.89
130	22818	2.244	0.27	1.558	0.32
160	25708	2.250	0.00	1.563	0.00

models. It is interesting to observe that Carreau-Yasuda fluid model does not generate any wake behind the cylinder so the recirculation length is zero in contrast to the power-law fluid model for the given Reynolds number. This is also reflected with higher force coefficients prediction using Carreau-Yasuda fluid model than the power-law fluid model (see Table 4.4) for the stationary ($\beta = 0$) and rotating ($\beta = 2$) cylinders. Table 4.4 shows that present results agree well with the reported literature for the power-law fluid model. The different streamline patterns using the Newtonian and non-Newtonian

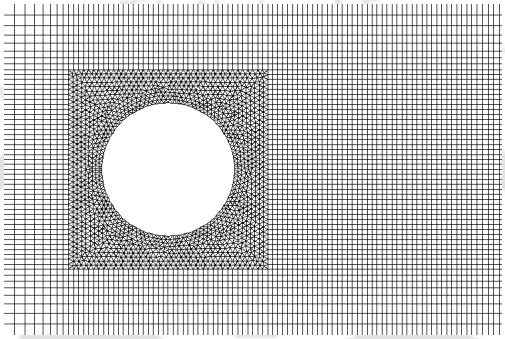

Figure 4.20: Discretised hybrid mesh encircling the circular cylinder of unit diameter.

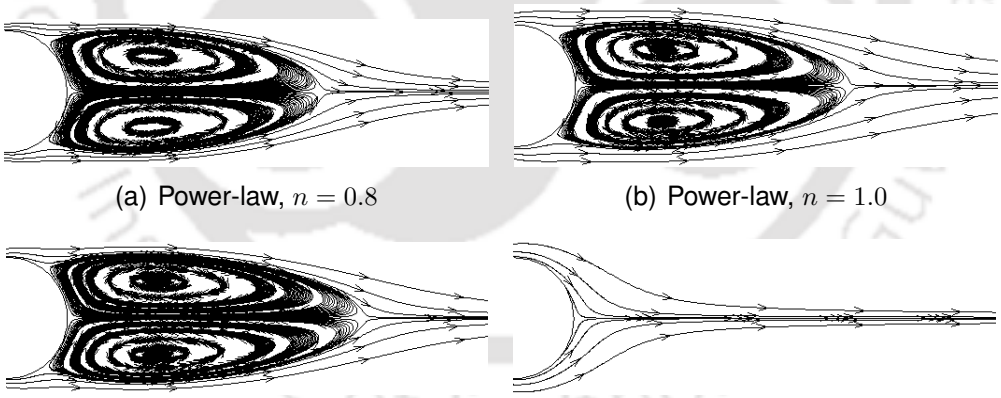

(a) Power-law, $n = 0.8$ (b) Power-law, $n = 1.0$

(c) Power-law, $n = 1.2$ (d) Carreau-Yasuda

Figure 4.21: Streamline pattern of steady flow of different fluid models over the stationary circular cylinder at $Re = 40$.

fluid models over the rotating circular cylinder in the steady flow regime are shown in Figure 4.22. The Carreau-Yasuda fluid model does not generate any vortices around the cylinder surface in contrast to power law fluid model. Figure 4.23 shows reasonable agreement of the coefficients of pressure distributions over the cylinder surface

Table 4.4: Drag coefficient (C_d), lift coefficient (C_l) and recirculation length (l_r) of steady flow of non-Newtonian as well as Newtonian fluid models over a circular cylinder with different rotating speeds (β).

Re	β	Fluids	Researchers	C_d	C_l	l_r
40	0	Power-law, n=0.8	Bharti et al. [74]	1.42	–	2.35
			Present	1.52	–	2.10
		Power-law, n=1.0	Bharti et al. [74]	1.53	–	2.22
			Ding et al. [75]	1.71	–	2.20
			Present	1.58	–	2.27
		Power-law, n=1.2	Bharti et al. [74]	1.54	–	2.32
			Present	1.63	–	2.46
		Carreau-Yasuda	Present	4.31	–	–
	2	Power-law, n=0.8	Panda and Chhabra [76]	0.85	-5.38	–
			Present	0.87	-5.54	–
		Newtonian (n=1.0)	Panda and Chhabra [76]	0.84	-5.72	–
			Paramane and Sharma [77]	0.86	-5.60	–
			Present	0.92	-5.68	–
		Power-law, n=1.2	Present	0.99	-5.82	–
		Carreau-Yasuda	Present	3.39	-5.88	–

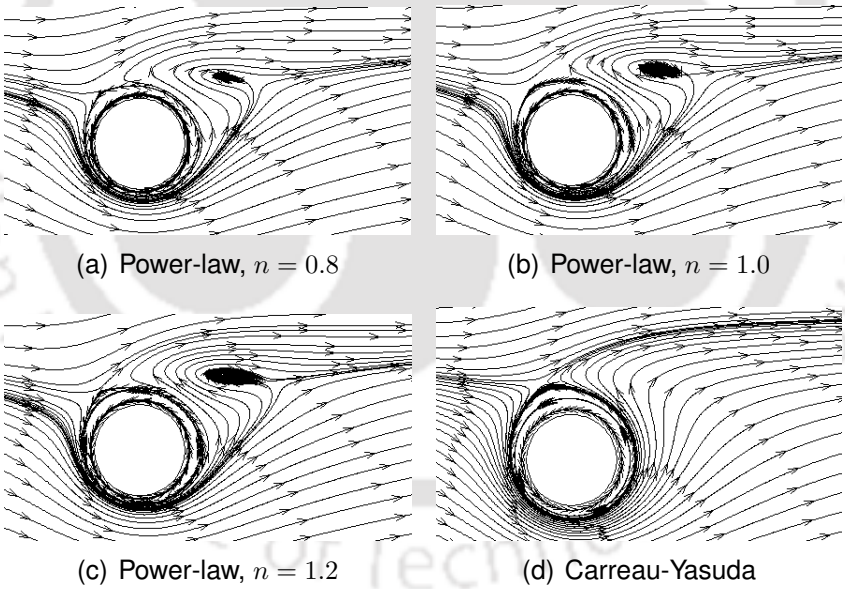

(a) Power-law, $n = 0.8$ (b) Power-law, $n = 1.0$

(c) Power-law, $n = 1.2$ (d) Carreau-Yasuda

Figure 4.22: Streamline pattern of steady flow of Newtonian and non-Newtonian fluid models over the rotating circular cylinder at $Re = 40$ and $\beta = 2$.

with that of Sivakumar et al. [15] at $Re = 40$ for the power-law fluid model with $n = 1$.

We have also studied simulations of unsteady flow where second-order time accuracy plays an important role and the results for stationary as well as rotating cylinder are presented using time averaged drag coefficients $\bar{c}_d$ in Table 4.5 at Reynolds num-

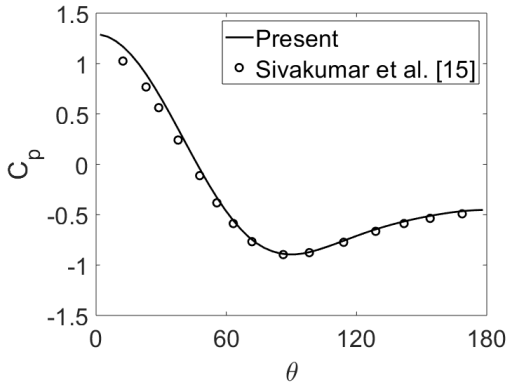

Figure 4.23: C_p variation over half surface of the cylinder from symmetry line with angle where it is calculated from the center of the cylinder.

bers of 100 and 140. The computed results from the present framework agree well with those reported by Fallah et al. [78] for the power-law fluid model. Figures 4.24(a) and

Table 4.5: Mean drag ($\bar{c_d}$) coefficients of the unsteady flow of non-Newtonian fluid over the stationary circular cylinder at $Re = 100$ and $Re = 140$.

Re	β	Fluids	Researchers	$\bar{c_d}$
100	0	Power-law, n=0.8	Fallah [78]	1.22
			Present	1.30
		Power-law, n=1.2	Fallah [78]	1.44
			Present	1.42
140	0	Power-law, n = 0.6	Fallah [78]	1.24
			Patnana [79]	1.23
			Present	1.26

(b) depict the history of C_d and C_l for the stationary ($\beta = 0$) and rotating ($\beta = 1.57$) cylinder respectively at the two given Reynolds numbers using the Newtonian fluid model. The present studies are in good agreement with the results of Zhang et al. [80] for both fixed and moving cylinder cases. It can be seen from Table 4.6 that the results from our simulations are comparable with those reported in Fallah et al. [78] for $\bar{c_d}$ and $\bar{c_l}$ at $\beta = 1.5$ and $Re = 100$.

These simulations categorically establish the proposed framework as an accurate and robust approach for simulating non-Newtonian flows using power-law and Carreau family of fluids on unstructured meshes.

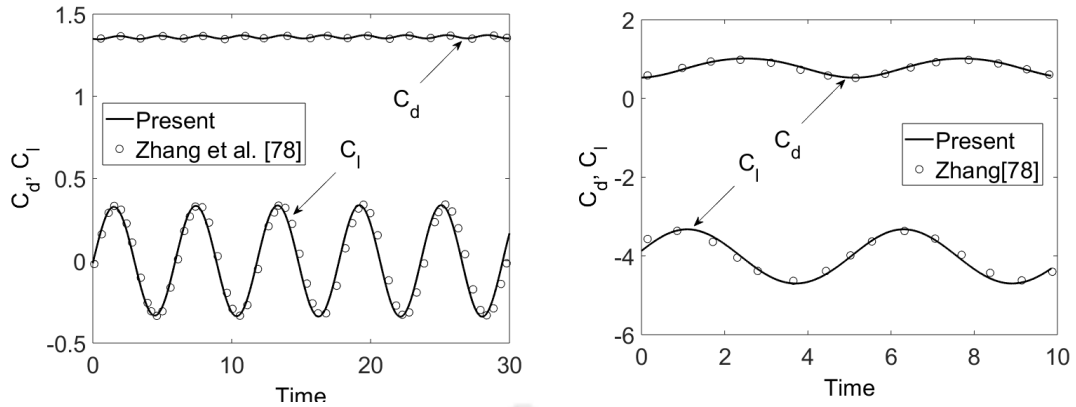

(a) Stationary, $\beta = 0$ and $Re = 100$ (b) Rotating, $\beta = 1.57$ and $Re = 200$

Figure 4.24: History of the force coefficients for the flow past circular cylinder when the periodic solution of C_d and C_l are achieved using the Newtonian model.

Table 4.6: Mean drag ($\bar{c_d}$) and lift ($\bar{c_l}$) coefficients of the rotating unsteady flow of power-law fluid model over the circular cylinder at $Re = 100$ and $\beta = 1.5$.

Fluids	Work	$\bar{c_d}$	$\bar{c_l}$
$n = 0.8$	Fallah [78]	0.846	-3.820
	Present	0.814	-3.783
$n = 1.0$	Fallah [78]	0.872	-4.058
	Present	0.857	-3.865
$n = 1.2$	Fallah [78]	0.916	-4.314
	Present	0.899	-3.955

4.8 Summary

In this chapter, we have validated the proposed computational framework on several steady and unsteady flow problems using non-Newtonian fluid models. Studies on structured and unstructured meshes show that the flow solver is able to accurately compute the numerical solutions. The solver has been shown to be nominally second-order accurate (both in space and time) and also satisfies discrete mass and momentum conservation. We have also shown that the linear solver strategy of using algebraic multigrid preconditioning for the Poisson equation could be more effective than ILU for high aspect ratio meshes and investigations using power-law fluids and Carreau models highlight the efficacy of the hybrid staggered/non-staggered framework developed as part of this thesis work.

Chapter 5

Application to steady hemodynamics

In this chapter the in-house computational framework has been utilised to investigate steady blood flow in canonical configurations of aneurysm and stenosis. We study the implications of different fluid models as well as geometries on the hemodynamics using numerical approach.

5.1 Background

Stenosis and aneurysm are two common problems that lead to cardiovascular diseases. Stenosis refers to the abnormal narrowing of blood vessel while aneurysm may be described as anomalous bulging of an artery. Since in-vivo patient specific investigations are not often possible, one needs to take help of numerical frameworks such as those in this study. It is a common practice to first simulate before carrying out an in-vitro experiment of hemodynamic problems. Furthermore, it is a more common practice to begin with simulations of steady flows before carrying out unsteady simulations though the latter are more realistic of flows in biofluid mechanics. Hence, we attempt to understand in this chapter the steady hemodynamics in aneurysm and stenosis by investigating different non-Newtonian models and geometries.

5.2 Problem set-up and computational details

The stenosis geometry is ideally modelled using a two-dimensional channel with double constrictions. The asymmetric stenosed geometry as shown in Figure 5.1 is obtained using a Gaussian function defined by [81],

$$y(x) = 1 - \sum_{i=1}^{2} c_i \, e^{-w_c(x-x_i)^2} \tag{5.1}$$

where, c_i represents the varying constriction ratios and is obtained from the relation

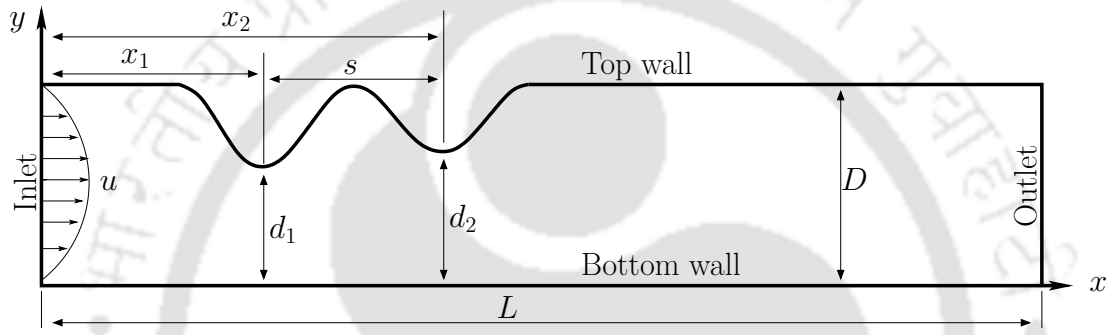

Figure 5.1: Schematic diagram of the asymmetric doubly constricted stenoses with boundary conditions

$c_i = (D - d_i)/D$. D is the depth of the channel without constriction and is the characteristic length. d_1 and d_2 denote the depths of channel at the first and second constriction respectively those lie at distances $x_1 = 2D$ and $x_2 = 4D$ from the inlet and are separated by a distance $s = x_2 - x_1$. $w_c = 3$ indicates a constant that governs the widths of the constrictions. The length of the channel $L = 36D$ is sufficiently long enough after the second constriction to ensure a fully developed flow and this has been verified from the simulations. Three doubly constricted channel geometries are obtained by varying the constriction ratios (c_i) to represent mild ($d_1 = d_2 = 0.8D$), medium ($d_1 = d_2 = 0.5D$) and severe ($d_1 = d_2 = 0.2D$) stenosed artery.

An intracranial aneurysm geometry is modelled using a two-dimensional channel with expansion at the top wall. The expansion is assumed to be ideal semi-circle that represents the asymmetric intracranial aneurysm. The geometric parameters of the two-dimensional aneurysm as seen from Figure 5.2 are selected from the literature

[58]. D is the depth and characteristic length of the channel, $W = 2.2D$ denotes the width of the aneurysm neck and $H = 2.2D$ is the height of the aneurysm. Three different aneurysm geometries are obtained by varying the ratio H/W ($= R$, known as aspect ratio) while keeping aneurysm neck width constant. The aneurysm geometries with different aspect ratios 1.0, 2.0 and 2.6 are represented by R_1, R_2 and R_3 respectively.

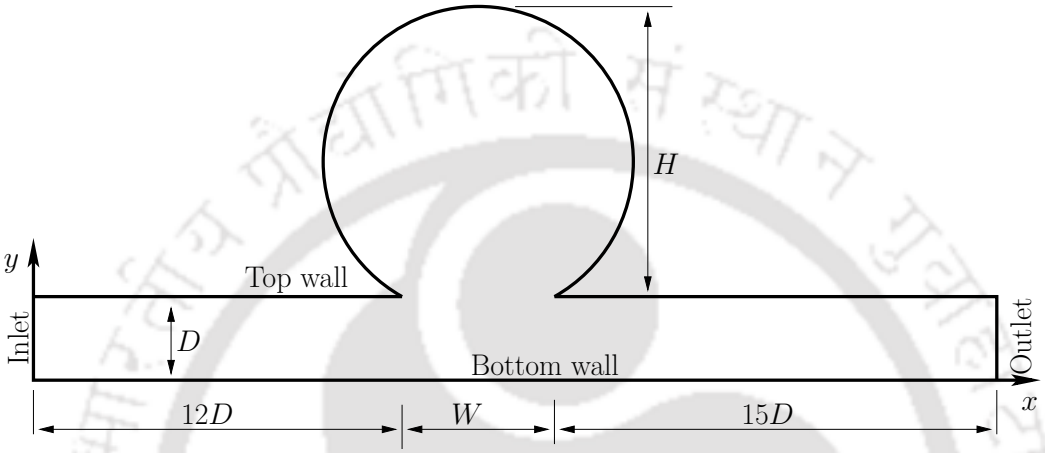

Figure 5.2: Schematic diagram of the aneurysm geometry with boundary conditions.

The double stenoses geometry is discretised using a combination of non-uniform quadrilateral (at non-constricted portion) and triangular (at stenosed region, see Figure 5.3) cells. We have ensured that the hybrid grid is able to resolve the boundary layer as it affects the wall shear which is a key parameter in hemodynamic simulations. Fully-developed parabolic velocity profile for channel flow using the power-law fluid is prescribed at the inlet. It is essential to obtain grid-independent solution for any numer-

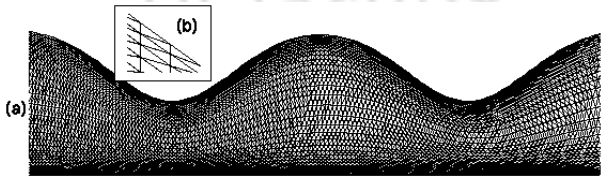

Figure 5.3: Typical triangulated grids showing resolution at the boundary for the medium stenosed artery. Part (b) shows the zoomed view of the meshes at the boundary near the curve surface.

ical simulation and we perform a thorough grid-refinement study only on the stenoses geometry of medium constriction. We investigate the variation of wall shear stress

(WSS) which is also clinically important and can be expressed as,

$$WSS = \tau_{xy}|_w \left(n_{w,x}^2 - n_{w,y}^2\right) + \left(\tau_{yy}|_w - \tau_{xx}|_w\right) n_{w,x} n_{w,y} \tag{5.2}$$

where, $\tau_{xy}|_w$, $\tau_{yy}|_w$, $\tau_{xx}|_w$ denote the components of shear stress at the wall and $n_{w,x}$, $n_{w,y}$ are the scalar components of unit normal vector at wall. Studies are carried out using the Newtonian fluid model on four meshes: Grid-1, Grid-2, Grid-3 and Grid-4 having cells 18000, 21000, 24000 and 27000 respectively. Figures 5.4(a) and (b) depict the distributions of WSS at the two constrictions and its neighbourhood for the grid refinement study on four different meshes using the Newtonian fluid model. A grid-independent solution is achieved using 24000 cells and this grid is employed for further computations involving blood flows using the different fluid models. A grid-independent

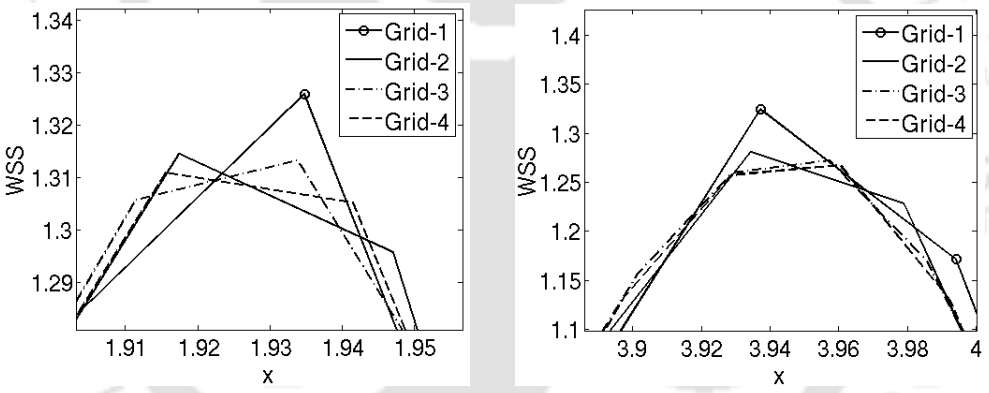

(a) First constriction (b) Second constriction

Figure 5.4: Wall shear stress at the two constrictions and their vicinity using four different meshes for the stenosed artery problem.

solution is achieved using Grid-3 and this grid is employed for further computations involving different fluid models. Despite the three stenoses geometries being different due to varying constriction ratios, we employ 24000 hybrid cells for all simulations assuming that it would also lead to nearly grid independent solution in other scenarios as well.

The aneurysm geometry is discretised using hybrid meshes which is the combination of non-uniform quadrilateral cells at the channel region and triangular cells at the expansion as shown in Figure 5.5. Grid refinement study is performed on the aneurysm

geometry R_1 for the given fluid model using hybrid cells 14946 (Grid-1), 20300 (Grid-2), 28848 (Grid-3) and 40574 (Grid-4). Figures 5.6(a) and (b) depict the distributions of

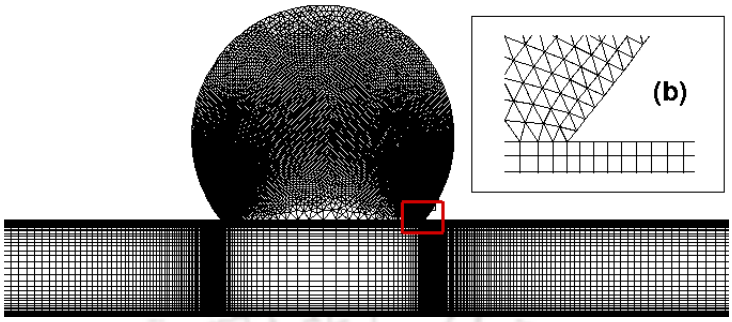

Figure 5.5: Hybrid mesh utilised to discretise the computational domain using triangular cells inside the aneurysm and quadrilateral cells in the parent artery. Part (b) is the zoomed view of the mesh in the vicinity of the aneurysm neck.

WSS for the grid refinement study using the four meshes with Newtonian model. The WSS value changes its sign from positive on the top wall of parent artery to negative inside the aneurysm because of the reverse flow (recirculation). The results of the mesh Grid-3 is accepted as the mesh independent since no discernible difference in WSS is observed relative to Grid-4 (finest) in comparison to the other three meshes and this grid has been utilised for the investigation. Grid independent result in WSS

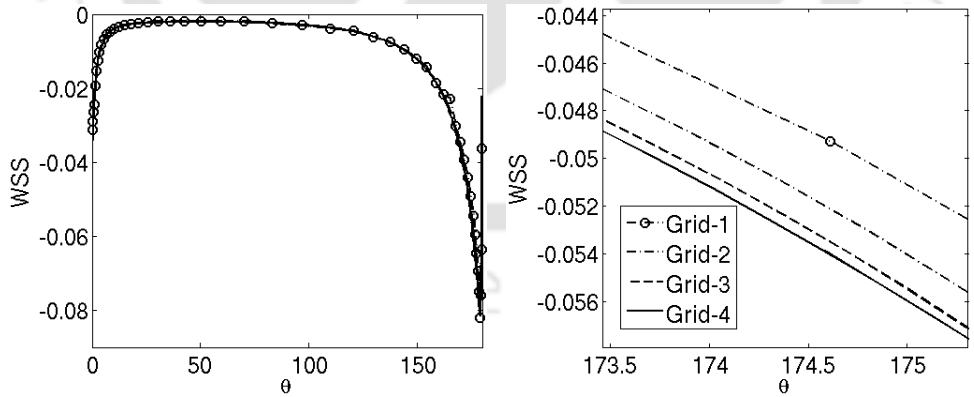

(a) Using Newtonian fluid (b) Zoomed view

Figure 5.6: Wall shear stress variations on the aneurysmed wall using the four meshes.

is obtained using the mesh Grid-3 and this grid has been utilised for further investigations. The three aneurysm geometries with different aspect ratios are discretised using 13150 (R_1), 19085 (R_2), and 24904 (R_3) triangular cells inside the dome (expansion).

In order to assess the effect of different non-Newtonian fluid models we choose the Carreau and power-law models. The fluid model parameters of the fluid models are tabulated in Table 5.1 to mimic the rheology of blood [2, 4, 6]. The simulations in the

Table 5.1: Model parameters of the different fluid models.

Parameters	Carreau-Yasuda	Carreau-Bird	Power law
Non-Newtonian exponent (n)	0.392	0.3568	0.8,1.0
High shear rate viscosity (μ_∞)	0.0022	0.0035	-
Zero shear rate viscosity (μ_0)	0.022	0.056	-
Model constant (a)	0.644	2.000	-
Relaxation time constant (λ)	0.110	3.313	-

following sections are carried out at $Re = 200$ with a time step $\Delta t = 0.005$ and Wi is defined based on the average diameter of an artery. We must remark that arterial wall is assumed to be rigid while this is not the case in practice which allows for a major implication and focus only on the role of fluid models and geometries on wall shear stress.

5.3 Effect of fluid models on double stenoses

We investigate the effect of different fluid models on the hemodynamics of a double stenoses when the blood flow is steady. The streamline patterns in the geometry obtained with the different fluid models for the double stenoses are shown in Figure 5.7. One can see the recirculation bubble length downstream of the second constriction shows considerable variation, with the longest recirculation bubble observed when using the power-law fluid while the Carreau-Yasuda model predict the shortest bubble. This is also reflected in the WSS distributions depicted in Figure 5.8, which also indicates a smaller peak WSS when using the power-law fluid. An interesting outcome of the study is that the Carreau-Bird model shows near-identical behaviour as the Newtonian fluid, both in terms of the peak WSS and the recirculation zone lengths. The Carreau-Yasuda model, in comparison, predicts slightly higher peak WSS, a marginal shift of the vortex core in the first constriction and a shorter bubble following the second constriction.

These observations can be reasoned by accounting for the apparent viscosity variation with shear rate for these fluids which is shown in Figure 5.9. It may be argued that for the shear rates persisting in the constriction, the apparent viscosity of the Carreau-Bird fluid is closest to the Newtonian model. The Carreau-Yasuda fluid would experience a viscosity higher than both these fluids while the power-law fluid has the lowest apparent viscosity, even lesser than the Newtonian fluid. The spatial distribution of apparent viscosity in the vicinity of the constrictions, omitted herein for sake of brevity, agrees with these arguments. Consequently, the “equivalent" Reynolds number [1] would be largest for the power-law fluid and smallest for the Carreau-Yasuda fluid. The length of the recirculation zone is expected to increase with equivalent Reynolds number, analogous to the observations in [72] for Newtonian flow over a backward facing step and the results from our numerical simulations are consistent with these expectations.

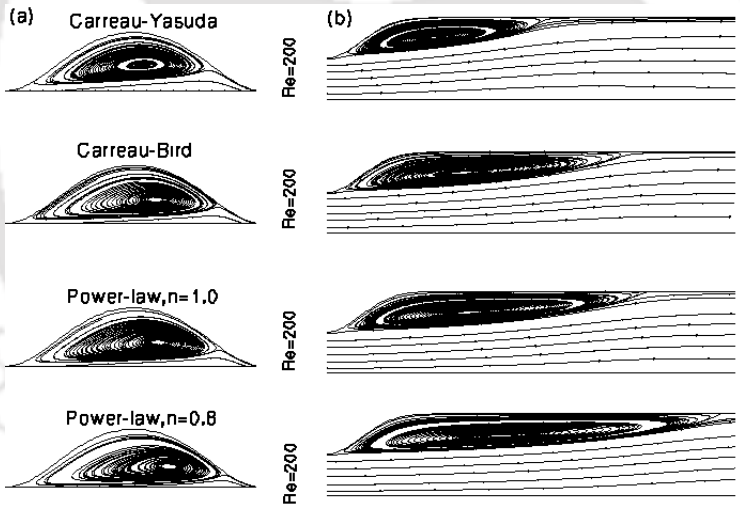

Figure 5.7: Streamline patterns at first and second constrictions using different fluids models.

It is a well-known fact [82] that endothelial cells respond to hemodynamic forces and their response to WSS is linked to plaque stability. In the absence of in-vivo studies, numerical simulations become critical in understanding the hemodynamics of stenosed arteries and choice of a suitable physiological model would dictate the predictions and subsequent clinical recommendations.

[1] This may be interpreted as the Reynolds number at which the pressure drop due to any non-Newtonian fluid flow would be equal to that of a Newtonian fluid flow through a given geometry.

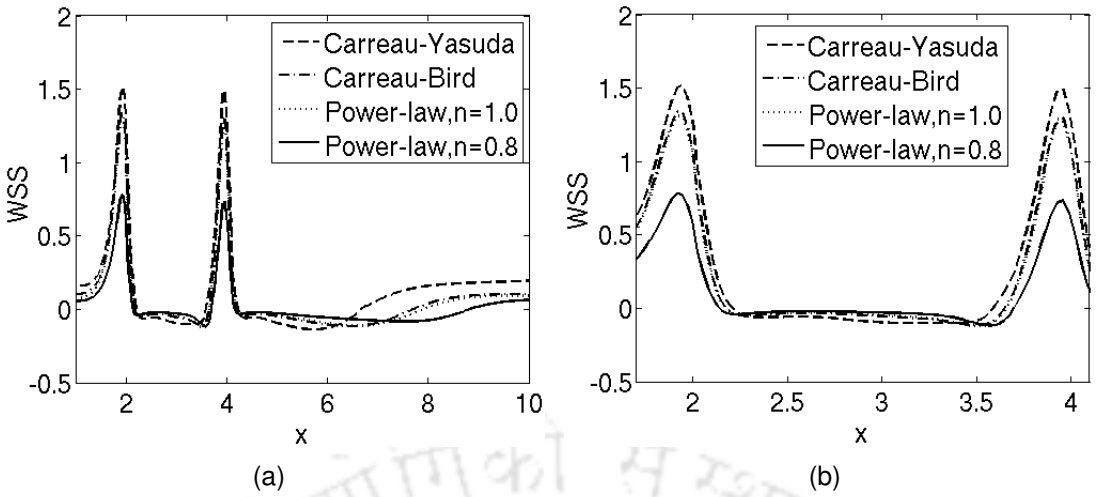

Figure 5.8: (a) Wall shear stress distributions and (b) zoomed view near constrictions for the stenosed artery problem using different fluid models.

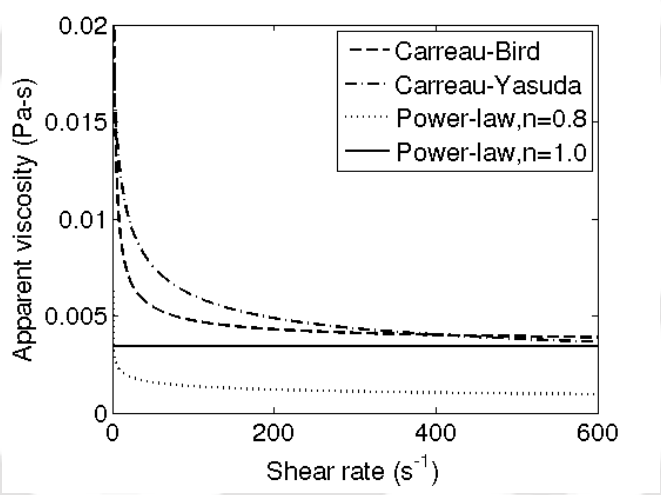

Figure 5.9: Variation of apparent viscosity with shear rate for the fluids considered in this study.

5.4 Role of degree of stenoses on hemodynamics

In this section, we investigate the role of constriction ratios representing mild, medium and severe stenosis on the hemodynamics in double stenoses. The shear-thinning Carreau-Yasuda non-Newtonian fluid model is adopted to model the blood for the simulations for these studies. The streamline patterns of the three stenoses using Carreau-Yasuda model are shown in Figures 5.10(a), (b) and (c). In case of the mild constriction, no recirculation bubble is formed as opposed to the other two constrictions. It is clearly comprehendable that with the increase in the constriction the wake length increases.

However, a striking difference is observed in case of the severely constricted stenosis whence multiple recirculation cores are developed just at the end of the second constriction. One can notice a recirculation bubble is generated in the bottom wall and there is a marginal shift of primary recirculation bubble core in severe constriction in comparison to medium constriction.

The aforementioned differences in the streamline pattern of the different degree of constrictions can be interpreted with the help of the relationship between apparent viscosity and shear-rate as mentioned in the previous section. From that plot, in the region of low shear-rate the value of apparent viscosity is very high and it remains invariant in the range of high shear-rates. In the region of flow recirculation the apparent viscosity becomes high as a result of low shear-rate and this increases with the increase in the constriction ratio. It is however necessary to carry out more in depth investigations into this behaviour.

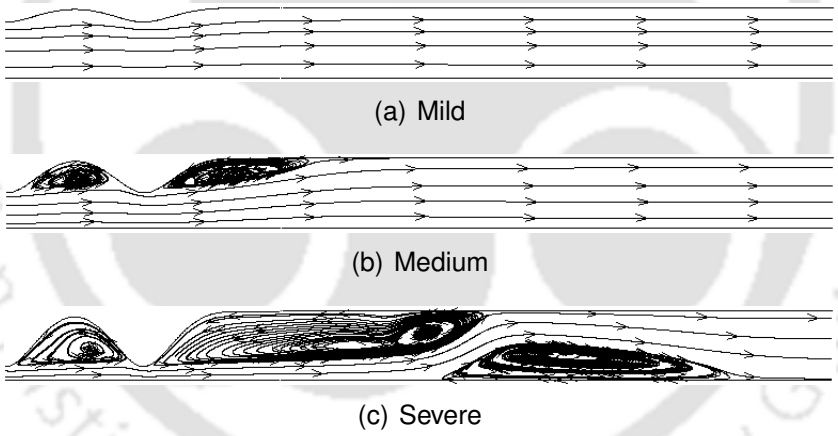

Figure 5.10: Streamline patterns obtained using the Carreau-Yasuda non-Newtonian fluid model for three constriction ratios.

Table 5.2 lists the pressure drops across the flow boundaries for the different constriction ratios including the straight channel (a representative of normal artery). It is easy to realize from this table that the pressure drop rises with the increase in the constriction ratios. Similar observations have been made in [51], although their study is performed on three-dimensional stenosis. Figure 5.11 depicts WSS distributions on the top wall. It is easy to notice from these plots that there is an increase in the peak WSS at the two constrictions regions as the constriction ratio increases which is

Table 5.2: The change in pressure drop with variation in the constriction ratio using Carreau-Yasuda fluid model.

Geometries	Pressure drop
Normal	- 0.118
Mild	- 0.125
Medium	- 0.164
Severe	- 0.723

consistent with the increasing pressure drop. Note that the distance between locations where WSS changes sign gives the length of recirculation bubble and the observations in Figure 5.11 agree with the streamline patterns shown in Figure 5.10.

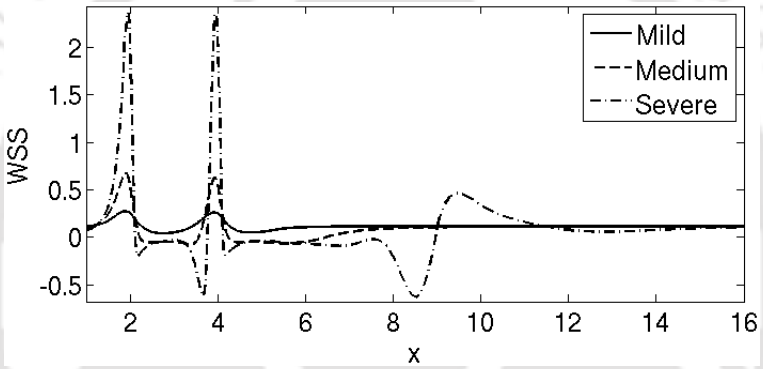

Figure 5.11: Wall shear stress distributions on the top wall for the different stenosed geometries.

It is now known [82, 83] that high shear stress can damage endothelum which causes to activate platelets aggregation and thrombus formation. However, no specific correlation has been clearly established to link the role of WSS in the atherosclerotic development [84]. The present investigation shows a clear and notable difference in the peak WSS on the wall of varying constriction of an asymmetric double stenoses and could possibly give some insights into this complex hemodynamics of the atherosclerotic process. Furthermore, the present study indicates that severity of the stenoses can be linked to high pressure drop and elevated wall shear stress. However, we must emphasize herein that these results must be interpreted with care since realistic flow in the arteries are inherently three-dimensional and pulsatile (unsteady).

5.5 Effect of fluid models on intracranial aneurysm

The focus of the present section is to investigate the effect of non-Newtonian (Carreau-Yasuda and power-law) and Newtonian fluid models on the hemodynamics of the idealised intracranial aneurysm. We choose the intracranial aneurysm geometry with aspect ratio R_1 for the study. WSS is the major parameter that could play a crucial role in the growth and rupture of intracranial aneurysm. Streamline plots inside the aneurysm dome for the geometry are shown in Figure 5.12 using the three fluid models. It is intriguing to observe that the flow patterns inside the aneurysm dome are analogous to that seen in a conventional lid-driven using the three fluids while the parent artery flow is marginally influenced by the presence of the aneurysm. We compare the WSS

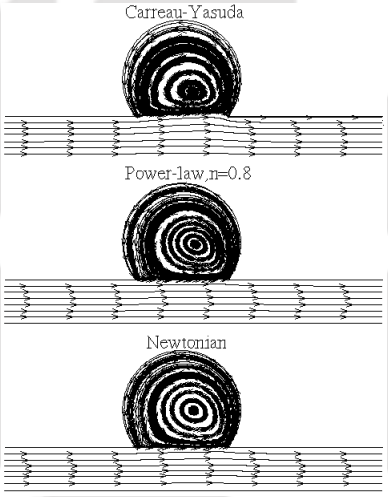

Figure 5.12: Streamline patterns inside the aneurysm dome using the different fluid models.

distributions on aneurysm dome wall using the different fluid models which is depicted in Figure 5.13. We observe that the Carreau-Yasuda fluid model computes a lower value of peak WSS relative to the Newtonian fluid model while the latter and power-law fluid model predict comparable WSS except at the downstream aneurysm neck region. It is reported in the literatures [78,79] that low WSS on the aneurysm wall indicates a higher chance of growth and rupture of an intracranial aneurysm. The present simulations indicate that the Newtonian model simulation of blood flow overestimates the wall shear stress in the aneurysm dome and underpredicts it at the post aneurysm

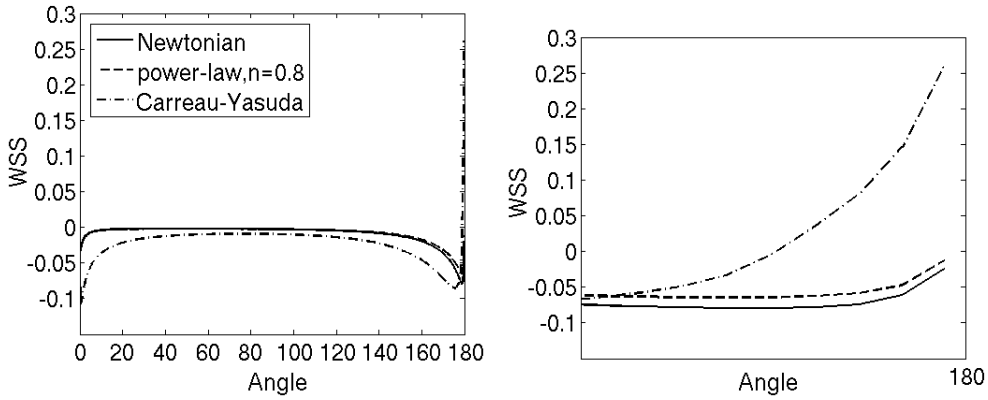

(a) WSS (b) Zoom in view

Figure 5.13: Wall shear stress variation on the aneurysm wall.

neck region. This may therefore lead to misinterpretation while planning for clinical interventions and highlights the need to account for non-Newtonian effects.

5.6 Effect of aneurysm size on hemodynamics

In this section, we investigate the effect of aneurysm size on the hemodynamics of aneurysms with the viscosity modelled using Carreau-Yasuda fluid. Three different aneurysm sizes are chosen which are represented by different aspect ratios $R_1 = 1.0$, $R_2 = 2.0$, and $R_3 = 2.6$ denoting mild, intermediate and severe aneurysms respectively. Figures 5.14 (a), (b) and (c) respectively depict the streamline patterns of the three aneurysm geometries with aspect ratios R_1, R_2, and R_3. We notice, interestingly that the bubble core shifts away from the parent artery with the increase in aneurysm size. The WSS distributions on the aneurysm wall are shown in Figure 5.15. We see that in the dome, WSS decreases with the increase in aneurysm size but this trend reverses at the neck region.

It has been stated previously that low WSS is an indicator of growth and rupture of an intracranial aneurysm. Herein in our study shows that low WSS region of the intracranial aneurysm lies at the posterior of aneurysm neck region with the increase in aneurysm size which can be a possible location for rupture. However, our results are not fully in agreement with those in [79] and necessitates further investigations.

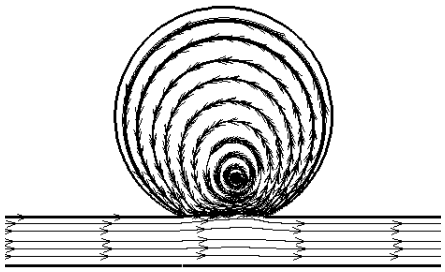

(a) R_3

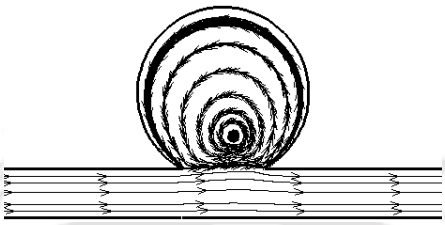

(b) R_2

(c) R_1

Figure 5.14: Streamline patterns in the different sized aneurysm.

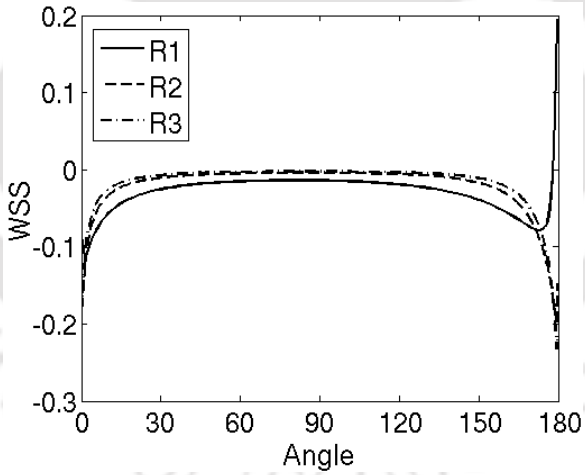

Figure 5.15: Wall shear stress distributions on the aneurysm wall.

5.7 Summary

In this chapter, the computational framework is utilised to investigate the steady blood flow dynamics in aneurysm and stenosis. The Carreau-Bird model shows near-identical behaviour as the Newtonian fluid model, in terms of the peak WSS in the study of double stenosis while Carreau-Yasuda model predicts slightly higher peak WSS. The

results of the different constriction ratio stenoses indicate that the WSS increases as the constriction ratio increases and consequently the pressure drop. Among the different fluid models, Newtonian model predicts a higher WSS than the two non-Newtonian models at the aneurysm dome region.The shear-thinning power-law fluid model however exhibits the highest WSS in the neighbourhood of aneurysm neck. Increase in aneurysm size is found to result with higher WSS at the aneurysm neck while it is seen to decrease in the aneurysm dome.

Chapter 6

Application to unsteady hemodynamics

The in-house incompressible flow solver has been utilised to investigate the unsteady flow of blood in aneurysm and stenosis configurations. The effect of pulsatile flow conditions and geometries on the hemodynamics using different non-Newtonian models have been studied.

6.1 Background

Studies performed in the earlier chapter are not entirely realistic because blood flow is inherently pulsatile (unsteady) owing to the action of heart that pumps blood periodically throughout the cardiovascular loop. The pressure or velocity pulse waveforms triggered by heart travels down the arterial network that alters with time and space. Furthermore, the flow waveform is influenced by the presence of aneurysm and stenosis [49] along with the non-Newtonian behaviour of blood. Blood has been treated as a Newtonian fluid in several scenarios, mostly in high shear flow regions [1]. It is reported in [47] that Newtonian modelling of blood results in overestimation of wall shear stress inside the aneurysm dome wall. We therefore attempt to employ the proposed computational framework to study the effect of pulsatile flows on hemodynamics in aneurysm and stenosis with different fluid models.

6.2 Problem set-up and computational details

The computational domains of stenosis and aneurysm of the previous chapter has been utilised for further investigations of the unsteady hemodynamics. Additionally, the same fluid model parameters as described in Chapter 5 have been used for the present studies. The pulsating characteristics of blood flow is modelled by prescribing an ideal sinusoidal velocity profile shown in Figure 6.1 at the inlet and is defined as,

$$u = \left[\left\{1 + \sin\left(\frac{4Wo^2 t}{Re}\right)\right\} - a\right] b + c \tag{6.1}$$

where, a, b, c are the scaling factors to obtain different pulsatile velocity conditions from the baseline/normal velocity waveform $u = 1 + \sin(4Wo^2 t/Re)$. $Wo = 0.5D\sqrt{\omega/\nu}$ denotes the Womersley number, where ω and ν are the angular frequency of a cycle and kinematic viscosity of fluid respectively. The Womersley is the ratio of unsteady inertia

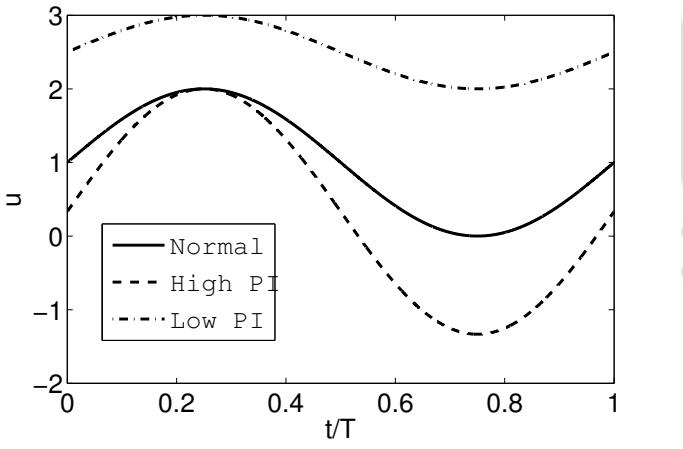

Figure 6.1: Pulsatile velocity waveforms over a cycle prescribed at the inlet of the computational domain.

force to viscous force and the values of a, b and c (see Table 6.1) are chosen in such a way to obtain low, high and normal pulsatility index (PI) defined by [58],

$$PI = \frac{u_{max} - u_{min}}{\overline{u}} \tag{6.2}$$

where, u_{max} and u_{min} denote the maximum and minimum velocity respectively and $\overline{u}$ represents the mean velocity of a cycle. PI is the parameter that measures the

Table 6.1: Parameters to obtain different pulsatile velocity inlet conditions.

Velocity waveforms	a	b	c	PI	Wo	$\overline{Re}$	Re_{max}	Re_{min}
Baseline	0	1	0	2	3.3	291	582	0
High PI	0.8	1.67	0	10.06	3.3	96	582	-384
Low PI	0	0.5	1.5	0.5	3.3	582	727	437

unsteadiness of flow in the artery over a cycle. Equation (6.2) can be equivalently expressed in terms of Reynolds numbers,

$$PI = \frac{Re_{max} - Re_{min}}{\overline{Re}} \tag{6.3}$$

where, Re_{max}, Re_{min} and $\overline{Re}$ are the maximum, minimum and mean Reynolds numbers respectively. The low and high PI waveforms that correspond to diseased condition (healthy condition lies in the range 0.54 to 2.8) of an artery are constructed from the baseline pulsatile velocity profile by tunning a, b and c [85, 86]. The high $PI = 10.06$ velocity waveform is derived by keeping the value of Re_{max} equal to that of the baseline velocity waveform. On the other hand, the low $PI = 0.50$ velocity waveform is constructed by a waveform shift that leads to a higher value of Re_{max} than the baseline velocity waveform. Simulations have been carried out for sufficient time so as to obtain periodic solutions at constant time step $\Delta t = 0.005$. The important flow parameters of context are the instantaneous streamline patterns, instantaneous wall shear stress, mean wall shear stress (WSS_{mean}) and oscillating shear index (OSI). The mean wall shear stress over a cycle is given by the following Eq. (6.4),

$$WSS_{mean} = \frac{\int_0^T WSS \; dt}{\int_0^T dt} \tag{6.4}$$

where, T denotes the period of a cycle. The definition of OSI follows from the relation [48],

$$OSI = \frac{1}{2}\left[1 - \frac{\left|\int_0^T WSS \; dt\right|}{\int_0^T |WSS| dt}\right] \tag{6.5}$$

Equation (6.5) can also be recast in the following form after simple manipulations,

$$OSI = \frac{1}{2}\left[1 - \frac{|WSS_{mean}|}{\frac{1}{T}\int_0^T |WSS|dt}\right] \tag{6.6}$$

It is easy to realize from Eq. (6.6) that OSI has a spectrum of 0 (minimum) to 0.5 (maximum). The minimum value of OSI represents a steady flow whereas the maximum value indicates purely pulsating flow with zero mean flow at any location. The parameters WSS_{mean} and OSI are crucial from a clinical perspective because they can provide useful information about the growth and rupture/blockage of an aneurysm and stenosis.

6.3 Effect of fluid models on double stenoses

The present section focusses on the investigations of hemodynamics of the double stenoses using three different fluid models to model the pulsatile blood flow while the pulsatile flow condition is effected utilising the high PI waveform. The studies have been performed on the geometry of stenoses with medium constrictions. Figure 6.2 depicts the streamline patterns at the four instants in a cycle. The flow patterns are shown only at the two constrictions and their vicinity. Newtonian and power-law fluid models predict comparable flow patterns in the given instants of the cycle in contrast to Carreau-Yasuda fluid model. The variations of instantaneous WSS over the cycle (period) at the location $x = 5$ (post-stenotic region) are shown in Figure 6.3. The maximum value is observed at the start or end of the cycle where the Carreau-Yasuda fluid model computes the highest value while power-law and Newtonian model indicate the WSS of nearly same magnitude, but lower than the Carreau-Yasuda model. Figure 6.4 shows the distributions of WSS_{mean} on the stenosed wall using the three fluid models. Carreau-Yasuda model experiences the highest WSS_{mean} at the two constrictions with the power-law predicting the least and the Newtonian model computes an intermediate value. These trends are similar to those seen in the steady flow results of the previous chapter and arguments in Section 5.3 holds good here as well. The OSI on

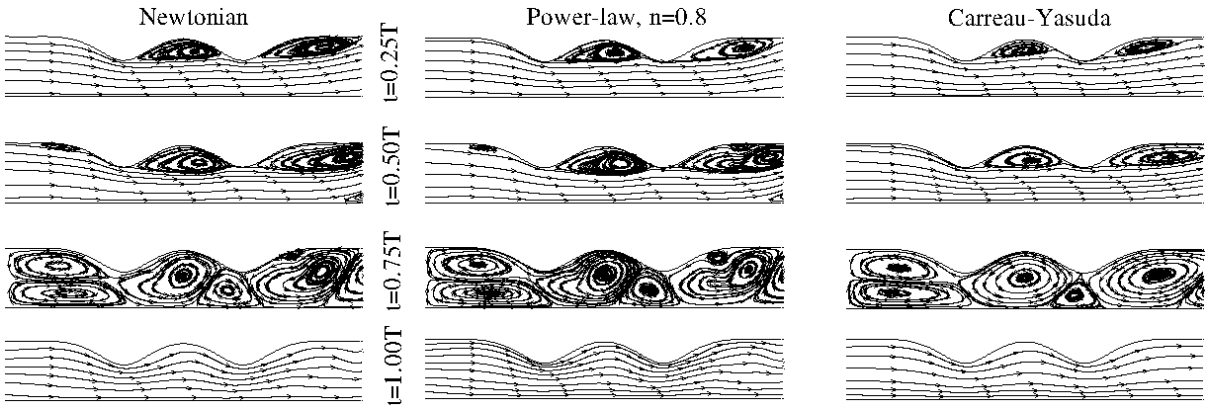

Figure 6.2: Streamline patterns at four time instants of a cycle using the different fluid models.

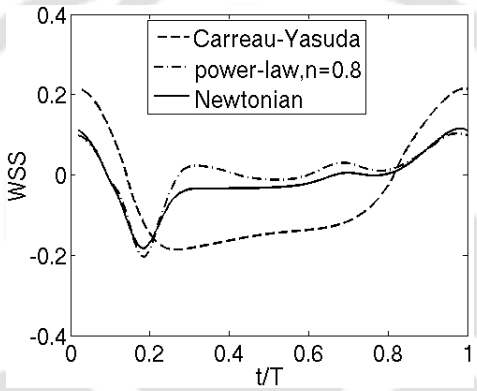

Figure 6.3: Temporal change of wall shear stress at the post-stenotic point ($x = 5$) over a period.

the top wall at the first and second constrictions and their neighbourhood are shown in Figures 6.5(a) and (b) respectively. It is intriguing to note that the OSI is relatively quiet low in regions of peak WSS_{mean} over a period. However, peak OSI values are observed after the first and second constriction except in case of the power-law fluid. Furthermore, the location of peak OSI in case of Carreau-Yasuda fluid model is shifted away from the two constrictions in contrast to the other two fluid models.

The power-law ($n = 0.8$) model produces marginal difference from Newtonian model. Therefore, Newtonian fluid model has been utilised for comparison with the Carreau-Yasuda model. Nevertheless, further studies are needed to understand the effect of shear-thinning power-law model ($n < 0.8$) which is part of future work. The importance of the non-Newtonian fluid model is evident at the two constrictions as well as regions

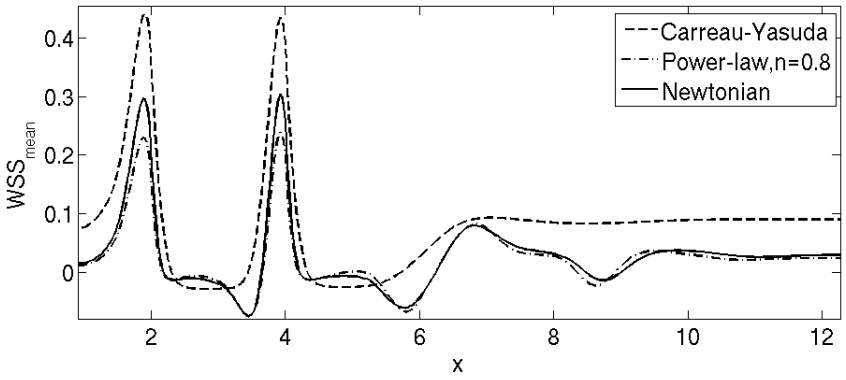

Figure 6.4: Average wall shear stress variation on the top wall comprising the two stenosis.

dominated by flow recirculation, i.e., after the first and second constrictions. In addition, it is reported that "the highly localized distribution of low and oscillatory shear stress along the walls strongly correlated with the focal locations of atheroma[1] in the human left coronary artery" in [48]. We see from the present results that Newtonian model overpredicts the low WSS_{mean} (i.e., a location with higher risk of atheroma formation) in contrast to the Carreau-Yasuda fluid model and this is in agreement with the results in [47].

6.4 Effect of degree of stenoses on hemodynamics

In this section, the hemodynamics of mild, medium and severely constricted geometries of double stenoses are investigated employing the Carreau-Yasuda fluid model to mimic the non-Newtonian behaviour of blood flow. The unsteady (pulsatile) flow is achieved by prescribing the ideal sinusoidal velocity profile in time with high pulsating index. The streamline patterns of the three geometries are shown in Figure 6.6 at the four instants (1) $t = T/4$, (2) $t = T/2$, (3) $t = 4T/3$, and (4) $t = T$ of the period. Recirculation bubbles are observed only at $t = 4T/3$ for the geometry with least constriction compared to other two geometries. Trains of multiple recirculation bubbles have been formed in the severe stenoses in comparison to the medium stenoses geometry. The variations of the instantaneous WSS over a cycle at the post-stenotic location ($x = 5$)

[1] It is the deposition of degenerative cells and debris in the inner lining of arterial wall.

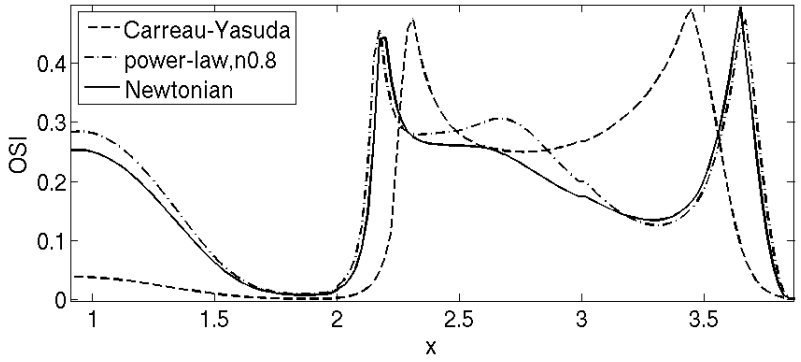

(a) First constriction region

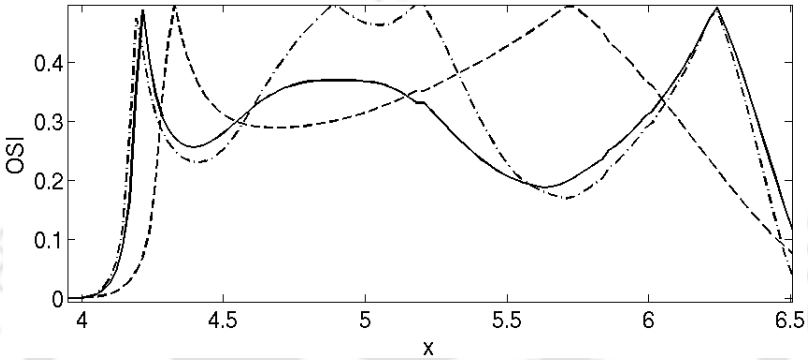

(b) Second constriction region

Figure 6.5: OSI distribution of the multiple constricted two-dimensional channel.

are shown in Figure 6.7 and Figure 6.8 depicts the distributions of WSS_{mean} on the stenosed wall. The calculated WSS_{mean} at the post-stenotic region is consistent with the instantaneous WSS prediction. An increase in WSS_{mean} with increase in constriction ratios has been observed from the simulations. The peak WSS_{mean} at the two constrictions are rise four times with increase in each constriction subsequently. Figures 6.9(a) and (b) portray the variation of OSI at and around of the first and second constrictions respectively. Multiple peaks are observed for the severe constriction in contrast to medium constriction and mild constriction which are purely pulsating with no net flow. On the other hand, the mild stenosis behaves similar to the case of a steady flow with a relatively low value of OSI compared to the other two configurations. Our results indicate that the implications of constriction ratios of stenosis are more prominent than the different fluid models from the view point of hemodynamic parameters. This study however can only provide limited information and more realistic waveforms are necessary to shed light on the mechanics of atherosclerosis and

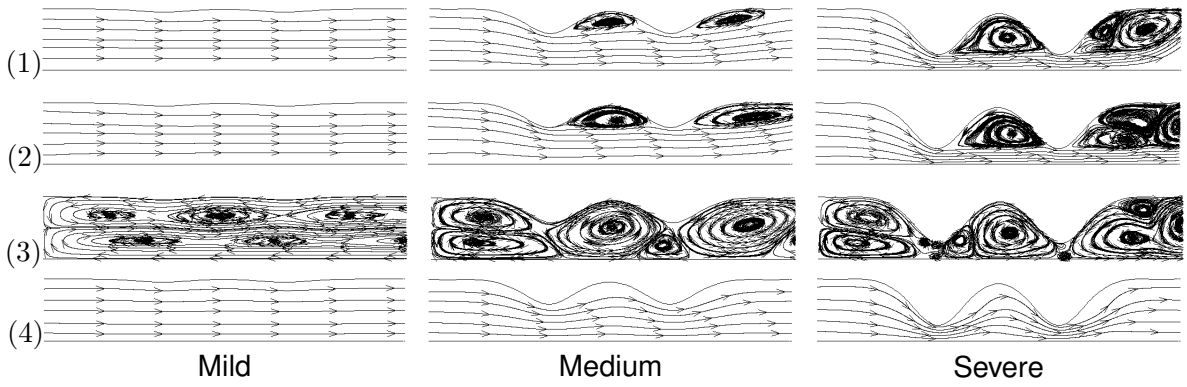

Figure 6.6: Streamline patterns for the three geometries of the double stenoses. Different instants $t = T/4$, $t = T/2$, $t = 3T/4$ and $t = T$ of a cycle are represented by the rows (1), (2), (3) and (4) respectively.

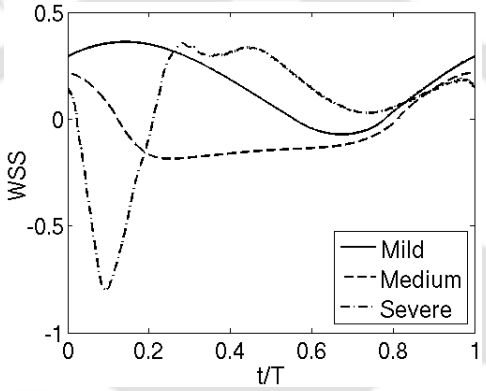

Figure 6.7: Instantaneous wall shear stress distributions within a cycle at $x = 5$.

thrombosis.

6.5 Effect of fluid models on intracranial aneurysm

In this section, we investigate the effect of two fluid models on the hemodynamics of an ideal intracranial aneurysm using the high pulsatility index velocity waveform. Newtonian and Carreau-Yasuda (non-Newtonian) fluid models are utilised for the simulations in the R_1 aneurysm geometry. Figure 6.17 (see rows (1) and (2)) shows the streamline patterns at four instants of a cycle using the Newtonian and non-Newtonian fluid models respectively. In case of Newtonian fluid model, a shift in the recirculation bubble core is observed as opposed to the non-Newtonian fluid model at the time instants $T/4$, $T/2$, and $3T/4$ of the cycle. The difference between the two fluid models could be

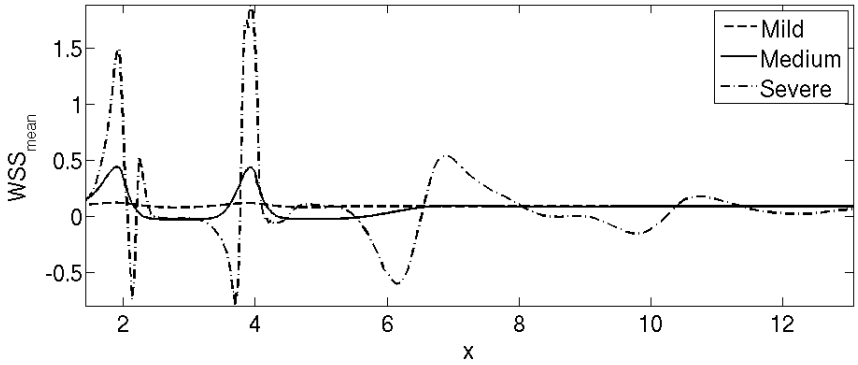

Figure 6.8: Average wall shear stress distributions on the top wall with doubly constricted channel of the three geometries.

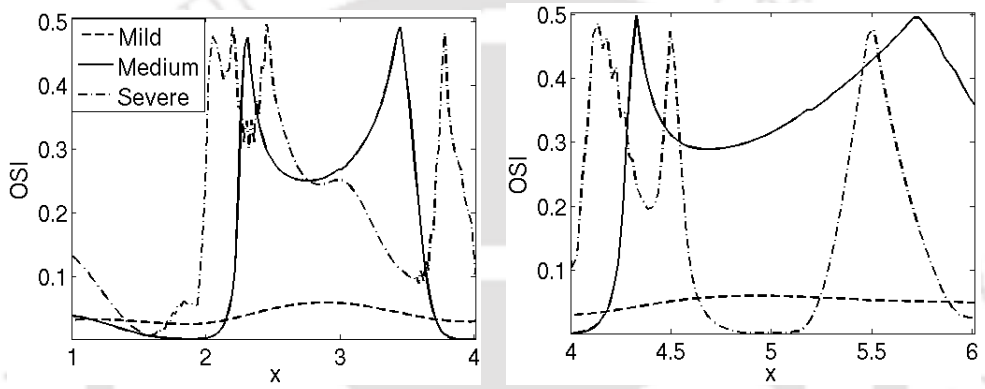

(a) First constriction region (b) Second constriction region

Figure 6.9: OSI distributions on the multiple constricted two-dimensional channel with different constriction ratios.

attributed to the shear-thinning nature of the latter in which apparent viscosity reduces with the increase in shear rate. Figure 6.11 depicts the distributions of instantaneous WSS at the middle of aneurysm wall (angle $= 90°$) over a cycle using the two fluid models. The distribution of WSS_{mean} on the aneurysm wall using the two fluid models are shown in Figure 6.12 and are consistent with the distributions of instantaneous WSS. The Newtonian model overpredicts the WSS_{mean} at the aneurysm dome and this flow behaviour has also been reported in [47]. Importantly, the non-Newtonian model computes higher WSS_{mean} at the aneurysm neck region compared to the Newtonian model. The OSI distributions on the surface of aneurysm wall using the two fluid models are shown in Figure 6.13 where the Newtonian model is associated with multiple peaks of OSI. Both fluid models compute high OSI at the aneurysm neck regions particularly

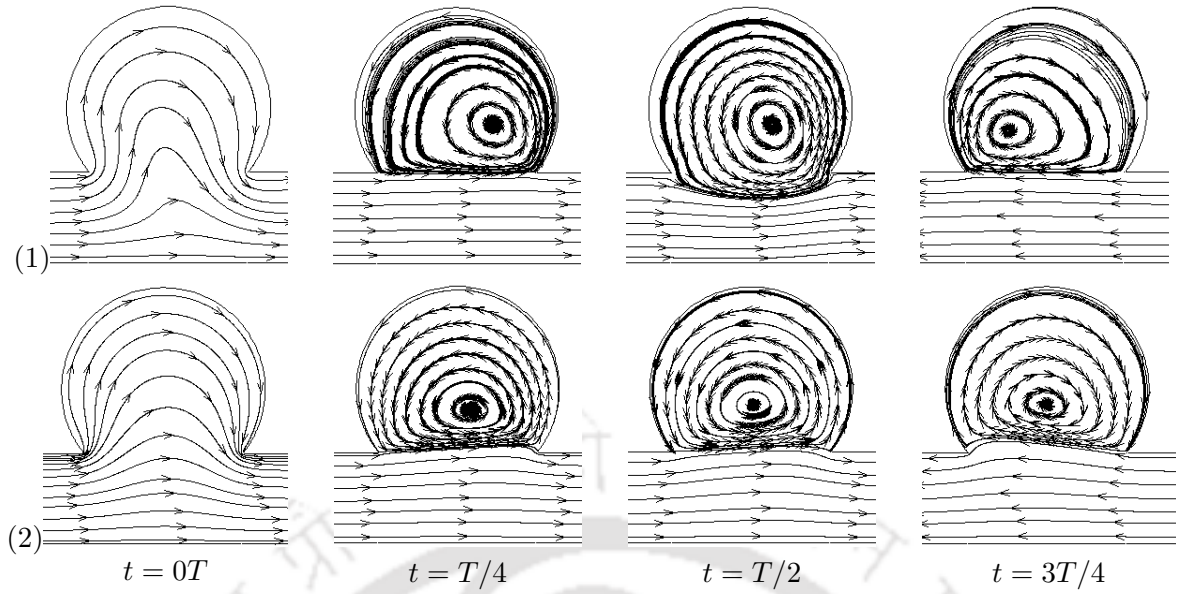

Figure 6.10: Streamline patterns using the two fluid models. First (1) and second (2) row respectively are for the Newtonian and non-Newtonian fluid models.

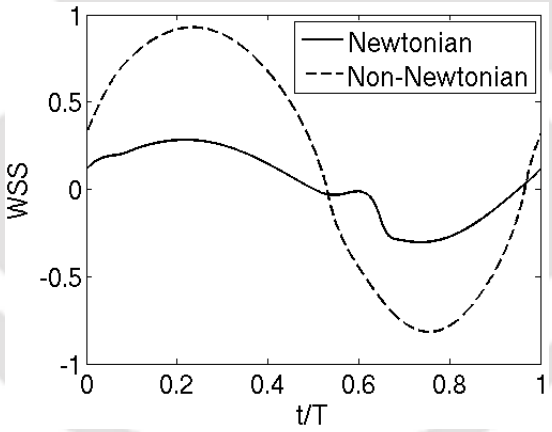

Figure 6.11: Wall shear stress distributions over a cycle at a point on the aneurysm dome using the two fluids.

the downstream of the aneurysm neck. It has been reported in the literature [56] that low wall shear stress is the predictive parameter for rupture of an intracranial aneurysm and we see it at the anterior aneurysm neck region of the aneurysm. We remark that our results support the fact that the modelling of blood using the Newtonian fluid would underestimate the low WSS_{mean} that can lead to wrong clinical interpretations.

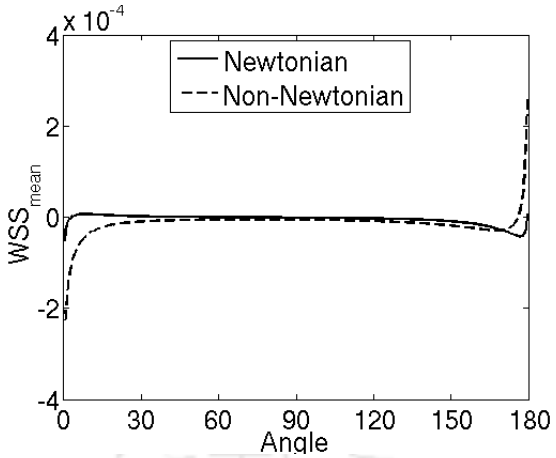

Figure 6.12: Distribution of mean wall shear stress inside the aneurysm dome wall using the two fluids.

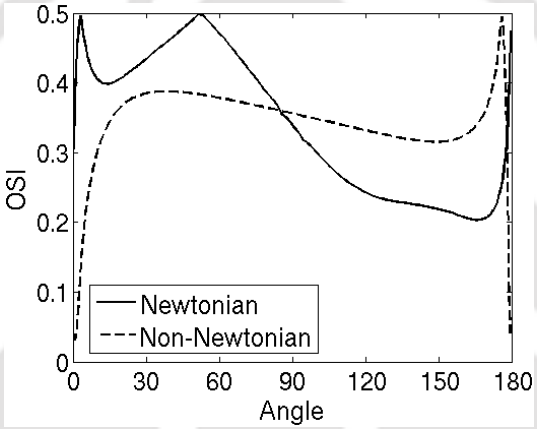

Figure 6.13: OSI distributions on the aneurysm wall using the two fluid models.

6.6 Effect of aneurysm size on hemodynamics

We attempt to gain insights into the hemodynamics in aneurysms with the increase (from R_1 to R_3) in aneurysm size and their implications on the clinically relevant parameters using the Carreau-Yasuda model and high pulsating index velocity waveform. The streamline patterns of the three aneurysms are depicted in Figure 6.14 at the four instants T, $T/4$, $T/2$, and $3T/4$ of a cycle. It is observed that the recirculation bubble cores come closer to the parent artery at $t = T/4$ in comparison to at $t = T/2$. The instantaneous WSS distributions over a cycle at a point (around 160°) is depicted in Figure 6.15(a). On the other hand, Figure 6.15(b) shows the distributions of WSS_{mean} in the aneurysm dome wall. The peak instantaneous WSS increases with the increase

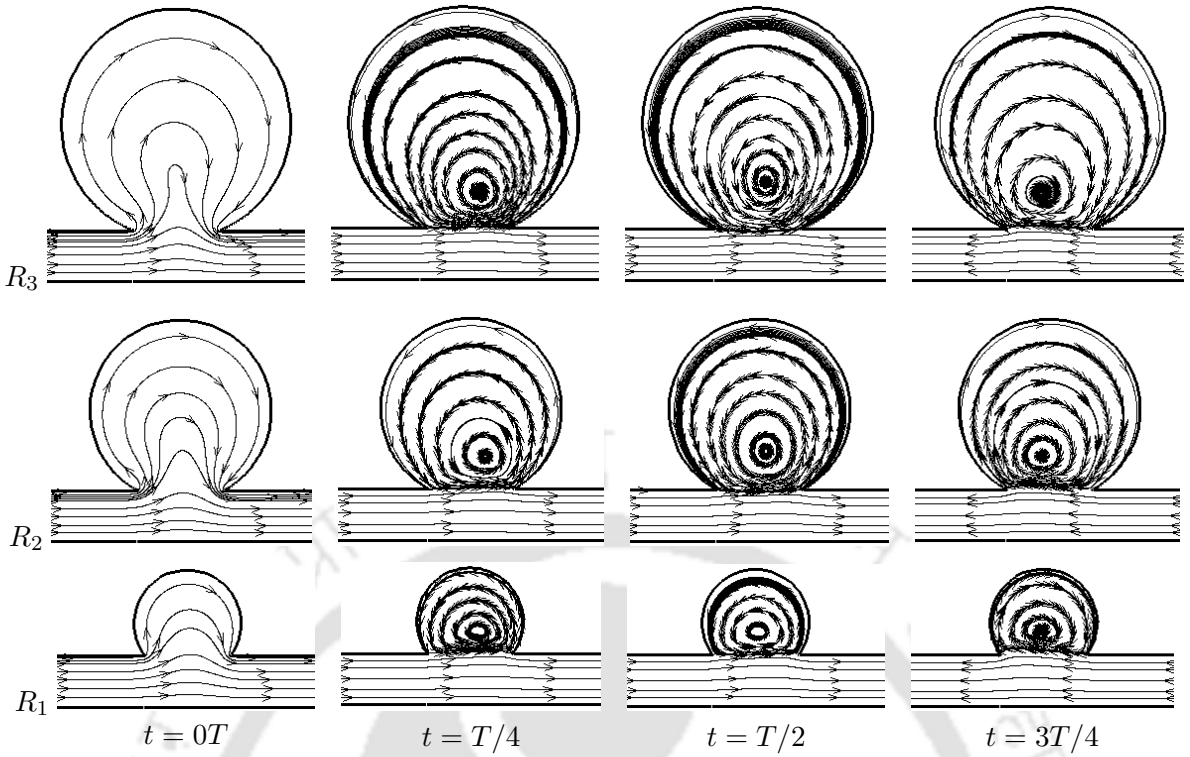

Figure 6.14: Streamline patterns for the different aneurysm sizes.

in the aneurysm size and this is also reflected in the distribution of WSS_{mean}. It can be easily observed that the aneurysm wall experiences non-uniform WSS_{mean} distributions for all the three aneurysms. There is a rise in peak WSS_{mean} of 25% and 45% at the anterior and posterior of the aneurysm neck region subsequently as R_1 to R_3. The

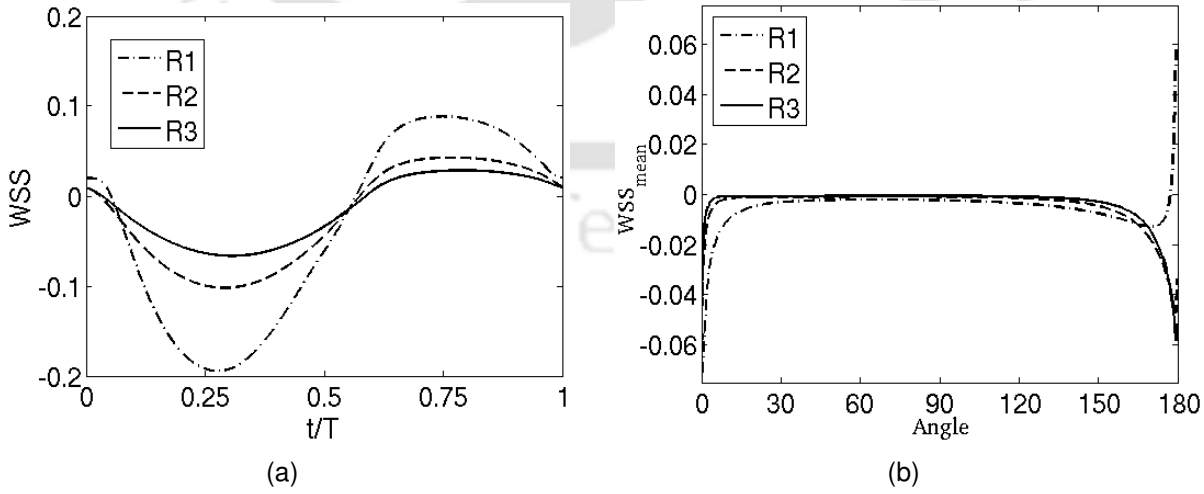

Figure 6.15: (a) Instantaneous and (b) mean wall shear stress distributions over a cycle at location 160° and aneurysm wall respectively.

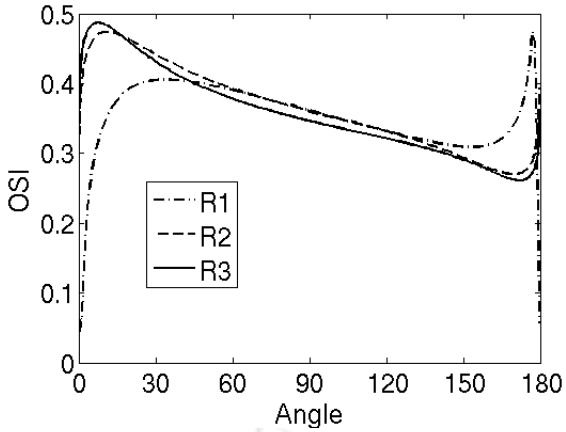

Figure 6.16: Oscillating shear stress distribution over the aneurysm wall.

reason is that owing to the high shear rates in the aneurysm neck site which results in increased hemodynamic stress. An analogous observation has been reported in [87] where an in-vitro experimental study was performed on an intracranial aneurysm. The OSI variation at the aneurysm wall is depicted in Figure 6.16, where regardless of the aneurysm sizes high unsteadiness is observed in the aneurysm neck region in contrast to dome.

Low WSS_{mean} in the aneurysm dome as opposed to the neck region can deposit thrombus that result in weakened and distended wall which may result in rupture of aneurysm [57]. Moreover, the high hemodynamic stress at the aneurysm neck site can also cause the neck to increase. Although the current problem is a simplified version (two-dimensional idealized geometry), present investigations are able to provide some information about the role of aneurysm size on the hemodynamics. Our results indicate higher value of WSS_{mean} at the aneurysm neck region which is congruent with the result in [87]. However, these are in contrast with the reports in [55] which states that low wall shear stress is the key parameter for the aneurysm growth (decrease with aneurysm size). It requires deeper investigations which is not in the scope of present work.

6.7 Effect of flow waveform on aneurysm

In this section, we investigate the role pulsatility index (flow waveforms) on the hemodynamics of intracranial aneurysm using the Newtonian and Carreau-Yasuda models. The two pulsatile flow conditions (see Table 6.1) mimic the low and high pulsatility index scenarios. The simulations have been performed in the idealized intracranial aneurysm geometry R_1. In addition to streamline, vorticity, arterial WSS_{mean}, instantaneous WSS and OSI are also examined to arrive at conclusions on how these parameters are affected by the different pulsatile waveforms. The streamline patterns for the high and low PI cases using the Newtonian fluid are depicted in Figures 6.17 (see rows (1) and (2)) at the four time instants of a cycle. The fluid flows in and out across the aneurysm neck in the high PI waveform while in the low PI case a single pattern of recirculation bubble is seen that delineates the aneurysm from the parent artery at all the time instants of a cycle. An intriguing difference is noticed at $t = 3T/4$ in the low PI case where no back flow is seen as opposed to the high PI case, despite a pulsatile velocity at the inlet. These flow patterns are also observed when the Carreau-Yasuda model (see Figures 6.17 rows (3) and (4)) is employed.

Dissimilarities in the vorticity contours (absolute values) and velocity vectors are observed in Figure 6.18 (see rows (1) and (2)) for the two pulsatile waveforms using the Newtonian model. The flow dynamics using the low PI case behaves similar to that of a cavity flow where the flow in parent artery rarely interact with the dome over the whole cycle. Shear layers emanating from the post aneurysm neck remain constant at all the time instants. This type of flow has been reported in the three-dimensional simulations of Le et al. [58] where they refer it to as “cavity mode”. Furthermore, for the high PI waveform they notice transport across the aneurysm neck, vortex ring formation and call it as “vortex ring mode”. However, in the present study (in two-dimension) we observe flow entrainment from parent artery into the aneurysm and no distinct vortex ring formation is seen. The use of Carreau-Yasuda model also reproduces these modes for the low and high PI which can be seen from Figure 6.18 (see rows (3) and (4)).

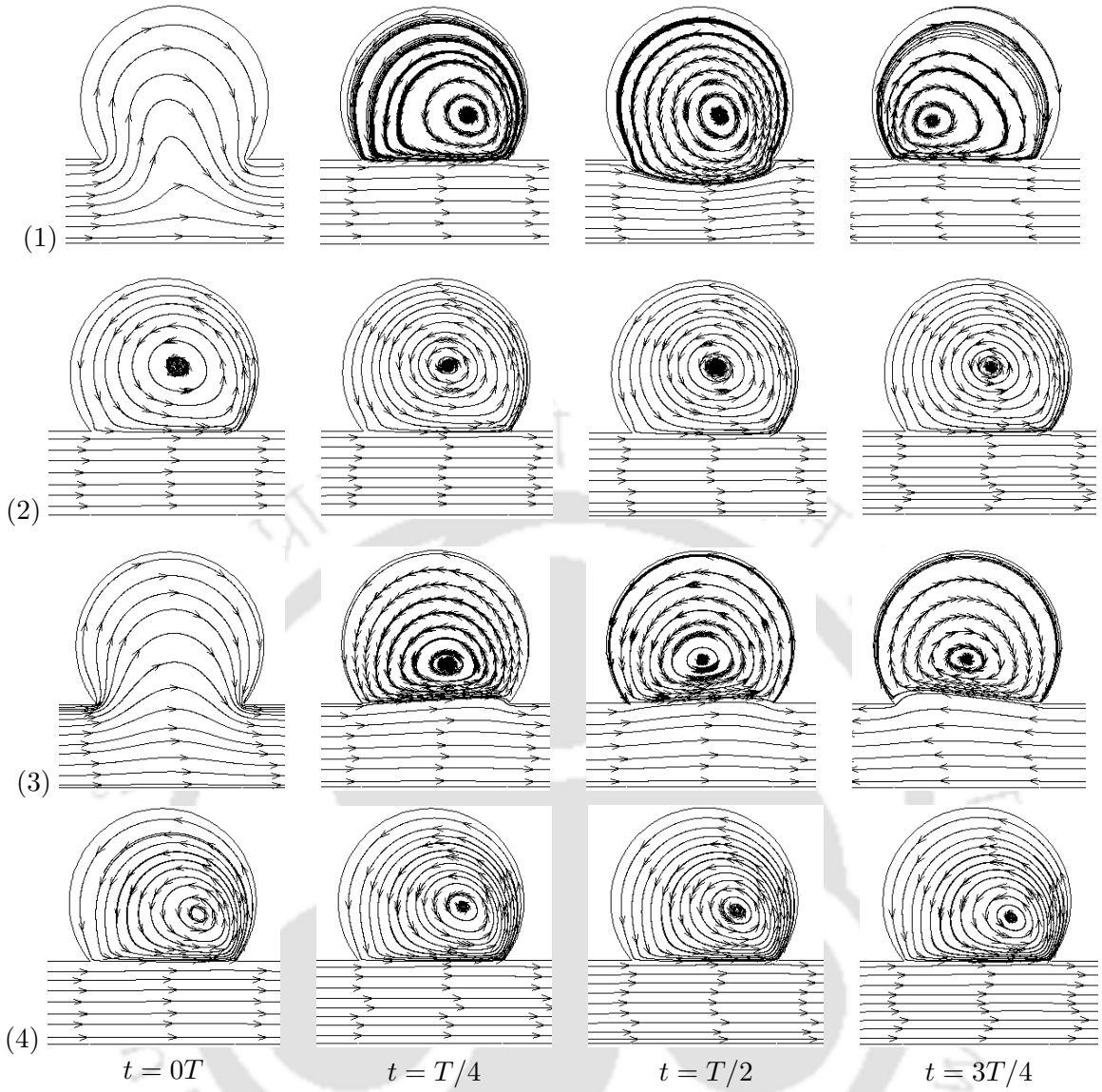

Figure 6.17: Streamline patterns using the two PI waveforms for the given fluid models. First (1) and second (2) row respectively represent for the high and low PI case using the Newtonian model. Third (3) and fourth (4) row indicate for the high and low PI case respectively using the non-Newtonian model.

Figures 6.19(a) and (b) depict the distributions of instantaneous WSS at the middle of aneurysm wall over a cardiac cycle using the two waveforms for both fluid models. Figures 6.19(c) and (d) show non-uniform distributions of the WSS_{mean} over the aneurysm wall using the two PIs for the Newtonian and non-Newtonian models respectively which are consistent with the distributions of instantaneous WSS. The instantaneous WSS variations with time remain constant in the entire cycle in low PI case whereas it fluctuates with time for the high PI case. Analogous distributions of WSS_{mean} are observed using the two PIs for the non-Newtonian fluid model as well.

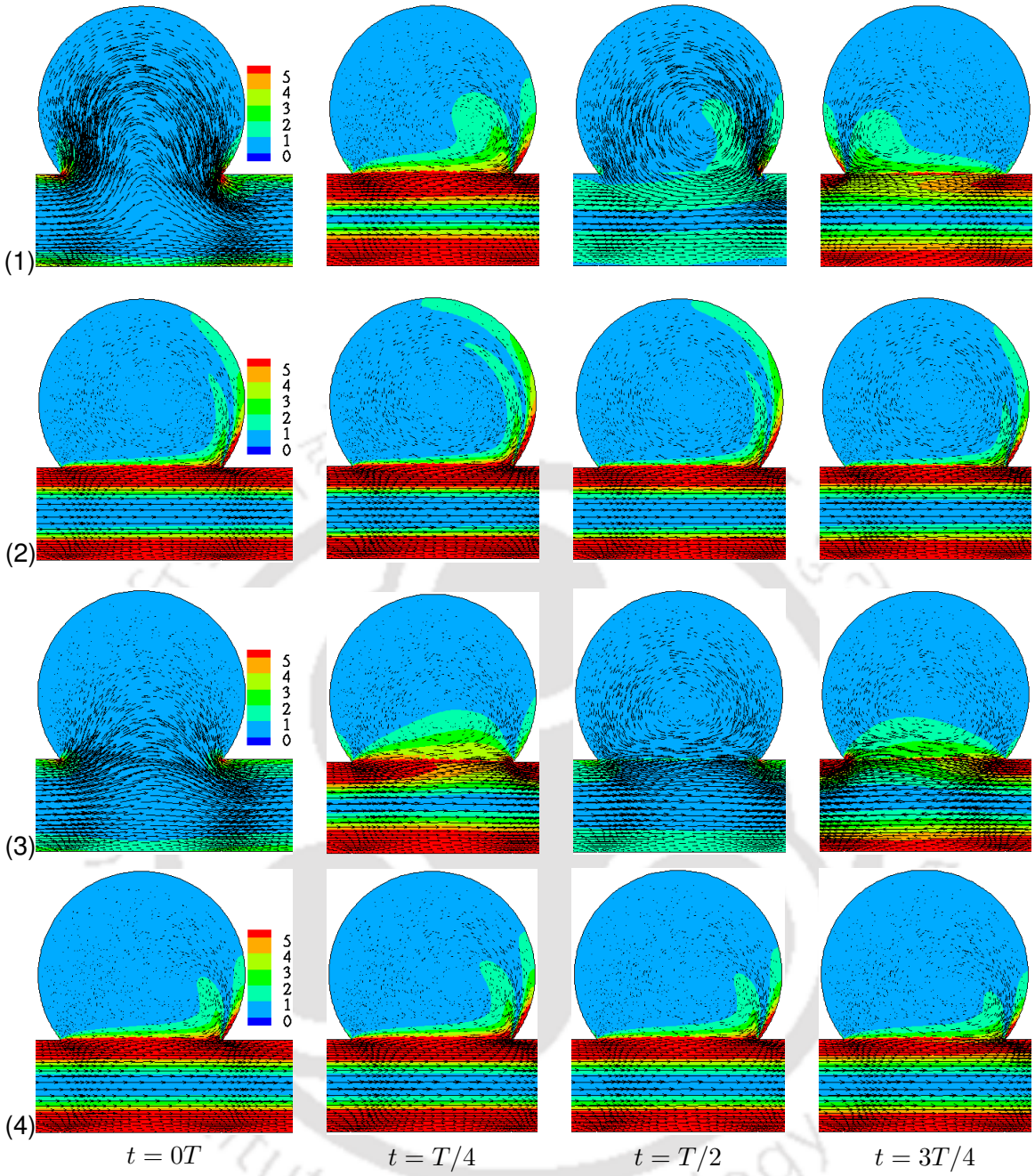

Figure 6.18: Vorticity contours and velocity vector plots for the two PI waveforms. First (1) and second (2) row respectively represent for the high and low PI cases using the Newtonian model. Third (3) and fourth (4) row indicate for the high and low PI cases respectively using the non-Newtonian model.

The OSI distributions over the surface of aneurysm wall using the two waveforms are shown in Figures 6.20(a) and (b) for the given fluid models. The high PI waveform flows are associated with multiple peaks of OSI on the aneurysm wall that indicate dome flows opposing that in the parent artery flow direction. On the other hand, the OSI distributions remain constant along the entire aneurysm wall for low PI case which

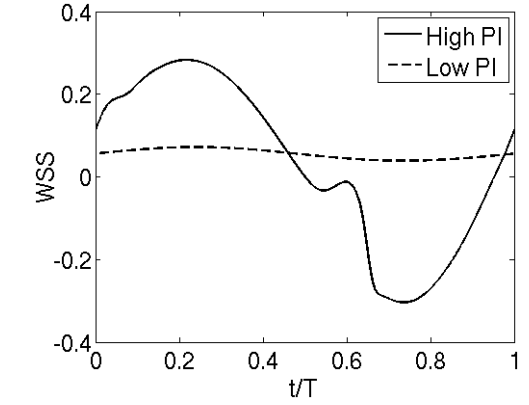

(a) Using Newtonian model

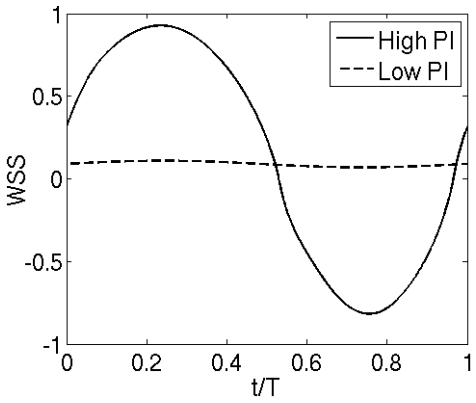

(b) Using non-Newtonian model

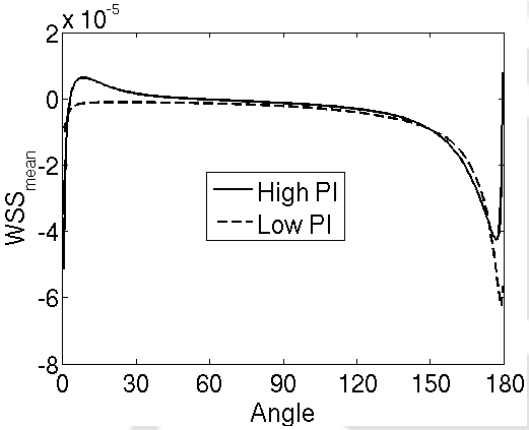

(c) Using Newtonian model

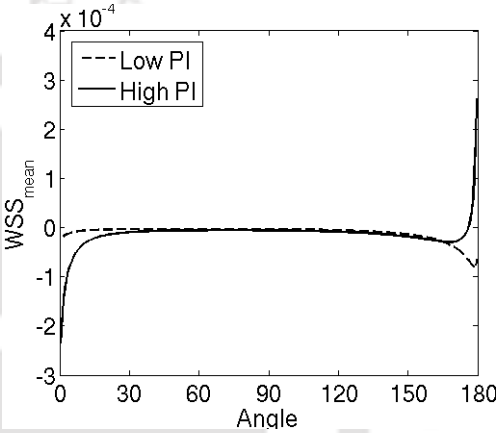

(d) Using non-Newtonian model

Figure 6.19: Instantaneous and mean wall shear stress alternations over a cycle at a point on the aneurysm dome using the two velocity waveforms for the given fluid models.

mean the flow is in phase with the parent artery flow. It has been already mentioned in

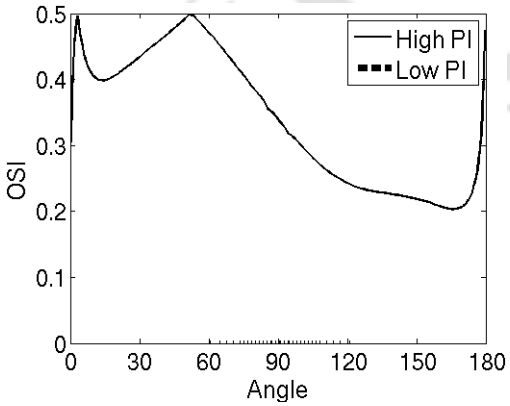

(a) Using Newtonian model

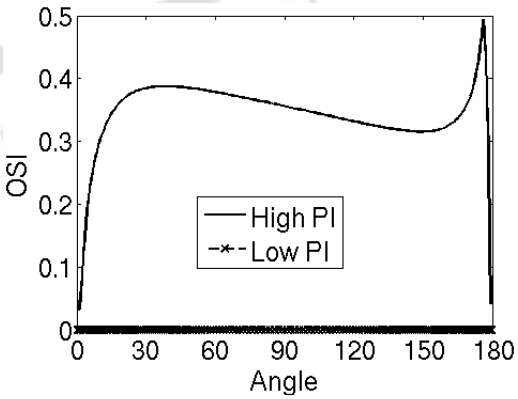

(b) Using non-Newtonian model

Figure 6.20: OSI distributions on the aneurysm wall using the two PI and two fluid models.

the above section that both the low and high PI waveforms correspond to the diseased condition of an artery. The present study demonstrates that the significance of the different fluid models is lesser compared to the pulsatile velocity conditions and these are quantitatively reflected in the analysis of WSS, WSS_{mean} and OSI.

6.8 Summary

The novel computational framework has been successfully applied to simulate the hemodynamics of multiple stenosed artery and intracranial aneurysm when the blood is modelled with the fluids: Newtonian, power-law and Carreau-Yasuda models. Unsteady blood flow studies with the different fluids in the medium stenosed artery have shown that the trend of distributions of the WSS_{mean} on the stenosed wall are consistent with the steady simulations. In addition, for a given fluid model the increase in constriction ratio increase the peak WSS_{mean} by around four times. The hemodynamic parameters in an intracranial aneurysm is assessed with the high and low pulsatility index (PI) waveforms using the two fluid models, Newtonian and Carreau-Yasuda. The results of the present investigations indicate that the flow waveforms have a significant role to play on the hemodynamics of the intracranial aneurysm in contrast to the rheology of the blood. High PI waveform quantifies high value of instantaneous WSS, WSS_{mean} and OSI the clinically relevant flow parameters in comparison to the low PI waveform. The flow dynamics of high PI waveform depends strongly on the fluid models as compared to the low PI. Newtonian fluid model undermine the importance of low mean wall shear stress at the anterior of aneurysm neck region as opposed to the non-Newtonian fluid model. Moreover, the implications of aneurysm size (aspect ratio: height to neck) is more significant than the different fluid models on the hemodynamics of the intracranial aneurysm.

Chapter 7

Conclusions and Future Scope

This chapter highlights the key contributions of the thesis work and imparts the directions for future research.

7.1 Conclusions

This thesis is devoted to the development and application of a novel and robust computational framework for incompressible non-Newtonian flows. The overall contribution of the thesis may be divided into two halves - the first being the development and validation of a new flow solver on unstructured meshes and the second its application for understanding hemodynamics of idealised stenoses and aneurysms. The salient conclusions from our studies on solver development may be summarised as follows.

1. A new hybrid staggered/non-staggered framework for solving incompressible flows using the finite volume method has been proposed. This framework solves for the normal momentum at the faces while the pressure is computed at the cell centers. It allows for a natural extension of the staggered framework to non-structured grids but effects the flux computations using ideas from collocated finite volume method.

2. This novel approach solves only one momentum equation independent of the number of spatial dimensions and is second-order accurate in space and time.

The spatial and temporal orders of accuracy are preserved even on unstructured meshes and has been verified through numerical experiments.

3. The overall second-order accuracy of the flow solver is also dependent on the order of accuracy of the velocity reconstruction approach. The velocity reconstruction is a vector interpolation strategy to obtain the centroidal velocity vector from the scalar normal momentum. A velocity reconstruction approach based on Green-Gauss methodology has been proposed to obtain the cell-center velocities that are necessary to calculate the convective and viscous fluxes.

4. A lower-order accurate velocity reconstruction is shown to result in spurious numerical solutions despite satisfying the divergence constraint. This has been found to be related to the inconsistency in the viscous flux computations and the errors due to this inaccuracy translates as non-physical solutions on arbitrary polygonal meshes. Interestingly, these inaccuracies do not diminish with grid refinement.

5. A defect-correction based approach has been implemented to ensure second-order accurate velocities and atleast first-order accurate gradients on any mesh topology. This leads to consistent viscous fluxes and accurately computes the flow field on unstructured meshes while also ensuring that the incompressibility constraint is satisfied.

6. The flow solver is found to ensure both mass and momentum conservation at the discrete level even though the control volumes are overlapping. Several test problems using power-law models and those in the Carreau family have been computed to highlight the accuracy and robustness of the proposed framework.

This novel computational framework has been employed to investigate steady as well as unsteady hemodynamics in stenoses and aneurysms. We report below the major findings from these studies.

1. The Carreau-Bird model shows near-identical behaviour as the Newtonian fluid

model, in terms of the peak WSS in the study of double stenoses while Carreau-Yasuda model predicts slightly higher peak WSS.

2. The results of the different constriction ratio stenoses indicate that the WSS increases as the constriction ratio increases and consequently the pressure drop for the given fluid. The impact of constriction ratios on the hemodynamics are more prominent than the different fluid models.

3. Among the different fluid models, Newtonian model predicts a higher WSS than the two non-Newtonian models at the aneurysm dome region.The shear-thinning power-law fluid model however exhibits the highest WSS in the neighbourhood of aneurysm neck.

4. Increase in aneurysm size is found to result with higher WSS at the aneurysm neck while it is seen to decrease in the aneurysm dome and this trend is reflected in unsteady model as well. In addition, the implications of aneurysm size (aspect ratio: height to neck) is more significant than the different fluid models on the hemodynamics of the intracranial aneurysm.

5. Unsteady simulations show that Newtonian fluid model undermine the importance of low mean wall shear stress at the anterior of aneurysm neck region as opposed to the non-Newtonian fluid model.

6. The results of the present simulations indicate that the flow waveform have a significant role to play on the hemodynamics of the intracranial aneurysm in contrast to the rheology of the blood.

In conclusion the present research endeavours to develop a novel computational framework that can simulate accurately non-Newtonian flows on complex geometries with an emphasis to study hemodynamics in aneurysm and stenosis.

7.2 Future directions of research

In this section, we stress on the limitations of the present investigations and outline probable future directions of research.

1. The unsteady simulations utilise ideal sinusoidal velocity profile therefore studies using realistic pulsatile waveforms with non-Newtonian fluid models can provide more information for better understanding of the hemodynamics of aneurysms and stenoses.

2. Present work has not considered the axisymmetric aspect of the problem of hemodynamics. Therefore, axisymmetric studies of stenosis and aneurysm can give insight about the hemodynamics of these ideal geometries.

3. The present study, assumes the arterial wall as rigid while it is distensible in reality. The arterial wall compliance interact with the pulsatile blood flow therefore it is necessary to develop fluid-structure coupling algorithm in conjunction with possibly immersed boundary methods.

4. A major shortcoming of the present studies are that they are in two-dimensional laminar regime and can only provide limited insight of the problem. Practical hemodynamic flows in the aneurysm and stenosis are three-dimensional and possibly turbulent. It is thus imperative to extend the methodology introduced in this thesis first for three-dimensional flows and later incorporate turbulence models in order to carry out realistic hemodynamics simulations in patient-specific configurations.

5. Patient-specific simulations would require that three-dimensional effects be considered in addition to the complex geometry. Furthermore, such studies would need to take into account the elastic nature of the walls making the problem a truly fluid-structure interaction problem which is of direct interest from a clinical perspective.

References

[1] Shibeshi Shewaferaw S and Collins William E. The rheology of blood flow in a branched arterial system. *Applied rheology (Lappersdorf, Germany: Online)*, 15 (6):398, 2005.

[2] Bird Robert Byron, Armstrong Robert Calvin, Hassager Ole, and Curtiss Charles F. *Dynamics of polymeric liquids*, volume 1. Wiley New York, 1977.

[3] Yasuda KY, Armstrong RC, and Cohen RE. Shear flow properties of concentrated solutions of linear and star branched polystyrenes. *Rheologica Acta*, 20(2):163–178, 1981.

[4] Gijsen F. J. H., Vosse van de F. N., and Janssen J.D. Wall shear stress in backward-facing step flow of a red blood cell suspension. *Biorheology*, 35:263–279, 1998.

[5] Wei G., Ru-xun L., and Ya-li D. Numerical investigation on non-Newtonian flows through double constrictions by an unstructured finite volume method. *Journal of Hydrodynamics*, 21:622–632, 2009.

[6] Bernsdorf Jörg and Wang Dinan. Non-newtonian blood flow simulation in cerebral aneurysms. *Computers & Mathematics with Applications*, 58(5):1024–1029, 2009.

[7] Jalali Alireza, Sharbatdar Mahkame, and Ollivier-Gooch Carl. An efficient implicit unstructured finite volume solver for generalised newtonian fluids. *International Journal of Computational Fluid Dynamics*, pages 1–17, 2016.

[8] Darwish MS, Whiteman JR, and Bevis MJ. Numerical modelling of viscoelastic liquids using a finite-volume method. *Journal of non-newtonian fluid mechanics*, 45(3):311–337, 1992.

[9] Oliveira P J, Pinho Fernando Tavares de, and Pinto G A. Numerical simulation of non-linear elastic flows with a general collocated finite-volume method. *Journal of Non-Newtonian Fluid Mechanics*, 79(1):1–43, 1998.

[10] Oliveira Paulo J. Method for time-dependent simulations of viscoelastic flows: vortex shedding behind cylinder. *Journal of non-newtonian fluid mechanics*, 101 (1):113–137, 2001.

[11] Miranda Amílcar IP, Oliveira PJ, and Pinho Fernando Tavares de. Steady and unsteady laminar flows of newtonian and generalized newtonian fluids in a planar t-junction. *International journal for numerical methods in fluids*, 57(3):295–328, 2008.

[12] Neofytou P. A 3rd order upwind finite volume method for generalized Newtonian fluid flows. *Advances in Engineering Software*, 36:664–680, 2005.

[13] Choi H. W. and Barakat A. I. Numerical study of the impact of non-Newtonian blood behavior on flow over a two-dimensional backward facing step. *Biorheology*, 42:493–509, 2005.

[14] Chhabra R.P., Soares A.A., and Ferreira J.M. Steady non-Newtonian flow past a circular cylinder: a numerical study. *Acta Mechanica*, 172:1–16, 2009.

[15] Sivakumar P., Bharti R. P., and Chhabra R.P. Steady flow of power-law fluids across an unconfined elliptical cylinder. *Chemical Engineering Science*, 62:1682–1702, 2007.

[16] Prhashanna A., Sahu A.K., and Chabbra R.P. Flow of power-law fluids past an equilateral triangular cylinder: Momentum and heat transfer characteristics. *International Journal of Thermal Science*, 50:2027–2041, 2011.

[17] Dhiman A.K., Chhabra R.P., and Eswaran V. Steady flow across a confined square cylinder: Effects of power-law index and blockage ratio. *Journal of Non-Newtonian Fluid Mechanics*, 148:141–150, 2008.

[18] Nejat Amir, Jalali Alireza, and Sharbatdar Mahkame. A newton-krylov finite volume algorithm for the power-law non-newtonian fluid flow using pseudo-compressibility technique. *Journal of Non-Newtonian Fluid Mechanics*, 166(19): 1158–1172, 2011.

[19] Kim Dongjoo and Choi Haecheon. A second-order time-accurate finite volume method for unsteady incompressible flow on hybrid unstructured grids. *Journal of computational physics*, 162(2):411–428, 2000.

[20] Perron S., Boivin S., and Herard G.M. A finite volume method to solve 3D Navier-Stokes equations on unstructured collocated meshes. *Computers and Fluids*, 33:1305–1333, 2004.

[21] Dalal A., Eswaran V., and Biswas G. A finite-volume method for Navier-Stokes equations on unstructured meshes. *Numerical Heat Transfer, Part B*, 54:238–259, 2008.

[22] Wei G., Ya-li D., and Ru-xun L. The finite volume projection method with hybrid unstructured triangular collocated grids for incompressible flows. *Journal of Hydrodynamics*, 21:201–211, 2009.

[23] Rhie C. M. and Chow W. L. Numerical study of the turbulent flow past an airfoil with trailing edge separation. *American Institute of Aeronautics and Astronautics*, 21:1525–1532, 1983.

[24] Johnston Barbara M, Johnston Peter R, Corney Stuart, and Kilpatrick David. Non-Newtonian blood flow in human right coronary arteries: steady state simulations. *Journal of biomechanics*, 37(5):709–720, 2004.

[25] Chen J., Lu X., and Wang W. Non-Newtonian effects of blood flow on hemodynamics in distal vascular graft anastomoses. *Journal of Biomechanics*, 39:1983–1995, 2006.

[26] Boyd Joshua, Buick James M, and Green Simon. Analysis of the Casson and Carreau-Yasuda non-Newtonian blood models in steady and oscillatory flows using the lattice Boltzmann method. *Physics of Fluids*, 19(9):093103, 2007.

[27] Harlow F.H. and Welch J.E. Numerical calculation of time-dependent viscous incompressible flow with free surface. *Physics of Fluids*, 8:2182–2189, 1982.

[28] Sheu Tony WH and Lee SHI-MIN. A segregated solution algorithm for incompressible flows in general co-ordinates. *International Journal for numerical methods in fluids*, 22(6):515–548, 1996.

[29] Segal A, Wesseling P., Kan J. Van, Oosterlee C.W., and Kassels K. Invariant discretization of the incompressible Navier-Stokes equations in boundary fitted co-ordinates. *International Journal for Numerical Methods in Fluids*, 15:411–426, 1992.

[30] Rida S, McKenty F, Meng FL, and Reggio M. A staggered control volume scheme for unstructured triangular grids. *International Journal for Numerical Methods in Fluids*, 25(6):697–717, 1997.

[31] Perot B. Conservation properties of unstructured staggered mesh schemes. *Journal of Computational Physics*, 159:58–59, 2000.

[32] Zhang X., Schmidt D., and Perot B. Accuracy and conservation properties of three-dimensional unstructured staggered mesh scheme for fluid dynamics. *Journal of Computational Physics*, 175:764–791, 2002.

[33] Perot B. and Nallapati R. A moving unstructured staggered mesh method for the simulation of incompressible free-surface flows. *Journal of Computational Physics*, 184:192–214, 2003.

[34] Wenneker I, Segal A, and Wesseling P. A mach-uniform unstructured staggered grid method. *International Journal for Numerical Methods in Fluids*, 40(9):1209–1235, 2002.

[35] Wenneker I, Segal A, and Wesseling P. Conservation properties of a new unstructured staggered scheme. *Computers and Fluids*, 32(1):139–147, 2003.

[36] Shashkov M., Swartz B., and Wendroff B. Local reconstruction of a vector field from its normal components on the faces of grid cells. *Journal of Computational Physics*, 139:406–409, 1998.

[37] Vidovic D., Segal A., and Wesseling P. A superlinearly convergent finite volume method for the incompressible Navier-Stokes equations on staggered unstructured grids. *Journal of Computational Physics*, 198:159–177, 2004.

[38] Vidovic D., Segal A., and Wesseling P. A superlinearly convergent Mach-uniform finite volume method for the Euler equations on staggered unstructured grids. *Journal of Computational Physics*, 217:277–294, 2006.

[39] Vidovic D. Polynomial reconstruction of staggered unstructured vector fields. *Theoretical and Applied Mechanics*, 36:85–99, 2009.

[40] Gilmanov A. and Sotiropoulos F. A hybrid Cartesian/immersed boundary method for simulating flows with 3D, geometrically complex, moving bodies. *Journal of Computational Physics*, 207:457–492, 2005.

[41] Natarajan G. and Sotiropoulos F. IDeC(k): A new velocity reconstruction algorithm on arbitrary polygonal staggered meshes. *Journal of Computational Physics*, 230: 6583–6604, 2011.

[42] Patel J K and Natarajan N. A consistent and well-balanced algorithm for multiphase flow simulations on unstructured meshes. *Journal of Computational Physics*, under review, 2016.

[43] Ge L. and Sotiropoulos F. A numerical method for solving the 3D unsteady incompressible Navier-Stokes equations in curvilinear domains with complex immersed boundaries. *Journal of Computational Physics*, 225:1782–1809, 2007.

[44] Angelidis D., Chawdhary S., and Sotiropoulos F. Unstructured Cartesian refinement with sharp interface immersed boundary method for 3D unsteady incompressible flows. *Journal of Computational Physics*, 325:272–300, 2016.

[45] Papathanasopoulou Panorea, Zhao Shunzhi, Köhler Uwe, Robertson Malcolm B, Long Quan, Hoskins Peter, Yun Xu X, and Marshall Ian. Mri measurement of time-resolved wall shear stress vectors in a carotid bifurcation model, and comparison with cfd predictions. *Journal of Magnetic Resonance Imaging*, 17(2):153–162, 2003.

[46] Steinman David A, Milner Jaques S, Norley Chris J, Lownie Stephen P, and Holdsworth David W. Image-based computational simulation of flow dynamics in a giant intracranial aneurysm. *American Journal of Neuroradiology*, 24(4):559–566, 2003.

[47] Xiang Jianping, Tremmel Markus, Kolega John, Levy Elad I, Natarajan Sabareesh K, and Meng Hui. Newtonian viscosity model could overestimate wall shear stress in intracranial aneurysm domes and underestimate rupture risk. *Journal of neurointerventional surgery*, pages neurintsurg–2011, 2011.

[48] He X. and Ku D.N. Pulsatile flow in the human left coronary artery bifurcation: average conditions. *Journal of Biomechanical Engineering*, 118:74–82, 1996.

[49] Ku D.N. Blood flow in arteries. *Annual Review of Fluid Mechanics*, 29:399–434, 1997.

[50] Wang Dinan and Bernsdorf Jörg. Lattice boltzmann simulation of steady non-newtonian blood flow in a 3d generic stenosis case. *Computers & Mathematics with Applications*, 58(5):1030–1034, 2009.

[51] Ang K.C. and Mazumdar J.N. Mathematical modelling of three-dimensional flow through an asymmetric arterial stenosis. *Mathematics and Computer Modelling*, 25:19–29, 1997.

[52] Nandakumar N., Sahu K.C., and Anand M. Pulsatile flow of a shear-thinning model for blood through a two-dimensional stenosed channel. *European Journal of Mechanics-B/Fluids*, 49:29–35, 2015.

[53] Nandakumar N. and Anand M. Pulsatile flow of blood through a 2D double-stenosed channel: effect of stenosis and pulsatility on wall shear stress. *Journal of Advances in Engineering Sciences and Applied Mathematics*, 81:61–69, 2016.

[54] Shojima Masaaki, Oshima Marie, Takagi Kiyoshi, Torii Ryo, Hayakawa Motoharu, Katada Kazuhiro, Morita Akio, and Kirino Takaaki. Magnitude and role of wall shear stress on cerebral aneurysm. *Stroke*, 35(11):2500–2505, 2004.

[55] Boussel Loic, Rayz Vitaliy, McCulloch Charles, Martin Alastair, Acevedo-Bolton Gabriel, Lawton Michael, Higashida Randall, Smith Wade S, Young William L, and Saloner David. Aneurysm growth occurs at region of low wall shear stress. *Stroke*, 39(11):2997–3002, 2008.

[56] Zhou Geng, Zhu Yueqi, Yin Yanling, Su Ming, and Li Minghua. Association of wall shear stress with intracranial aneurysm rupture: systematic review and meta-analysis. *Scientific Reports*, 7(1):5331, 2017.

[57] Foutrakis George N, Yonas Howard, and Sclabassi Robert J. Saccular aneurysm formation in curved and bifurcating arteries. *American Journal of Neuroradiology*, 20(7):1309–1317, 1999.

[58] Le Trung B, Borazjani Iman, and Sotiropoulos Fotis. Pulsatile flow effects on the hemodynamics of intracranial aneurysms. *Journal of biomechanical engineering*, 132(11):111009, 2010.

[59] Buchanan J.R., Kleinstreuer C., and Comer J.K. Rheological effects on pulsatile hemodynamics in a stenosed tube. *Computers and Fluids*, 29:695–724, 2000.

[60] Cho Y. I. and Kensey K. R. Effects of the non-Newtonian viscosity of blood on hemodynamics of diseased arterial flows: part 1, steady flows. *Biorheology*, 28: 241–262, 1991.

[61] Blazek J. *Computational Fluid Dynamics: Principles and Applications*, volume 1. Eslevier, Switzerland, first edition edition, 2001.

[62] Moin P and Kim J. On the numerical solution of time-dependent viscous incompressible fluid flows involving solid boundaries. *Journal of computational physics*, 35(3):381–392, 1980.

[63] Fan X-J, Tanner RI, and Zheng R. Smoothed particle hydrodynamics simulation of non-newtonian moulding flow. *Journal of Non-Newtonian Fluid Mechanics*, 165 (5):219–226, 2010.

[64] Balay S, Abhyankar S, Adams M, Brown J, Brune P, Buschelman K, Eijkhout V, Gropp W, Kaushik D, Knepley M, and others . Petsc users manual revision 3.5. *Argonne National Laboratory (ANL)*, 2014.

[65] http://www.ssisc.org/lis/, 2013. Accessed: 20-02-2013.

[66] Rausch R. D., Batina J. T., and Yang H. T. Y. Spatial adaption procedures on unstructured meshes for accurate unsteady aerodynamic flow computation. *American Institute of Aeronautics and Astronautics*, 91:1091–1106, 1991.

[67] Bell B.C. and Surana K.S. p-version least squares finite element formulation for two-dimensional incompressible Newtonian and non-Newtonian non-isothermal fluid flow. *International Journal for Numerical Methods in Fluids*, 18:127–162, 1994.

[68] Kim J. and Moin P. Application of a fractional-step method to incompressible Navier-Stokes equations. *Journal of Computational Physics*, 59:308–323, 1985.

[69] Lashckarbolok M., Jabbari E., and Vuik K. A node enrichment strategy in collocated discrete least squares meshless method for the solution of generalized newtonian fluid flow. *Scientia Iranica*, 21:1–10, 2014.

[70] Wang B., Zhao G., and Fringer O.B. Reconstruction of vector fields for semi-Lagrangian advection on unstructured, staggered grids. *Ocean Modelling*, 40: 52–71, 2011.

[71] Ternik P. Symmetry breaking phenomena of purely viscous shear-thinning fluid flow in a locally constricted channel. *International Journal of Simulation Modelling*, 4:186–197, 2008.

[72] Armaly B. F., Durst F., Pereira J. C. F., and Schonung B. Experimental and theoretical investigation of backward-facing flow. *Journal of Fluid Mechanics*, 127: 473–496, 1983.

[73] Basumatary M., Natarajan G., and Mishra S.C. Defect correction based velocity reconstruction for physically consistent simulations of non-Newtonian flows on unstructured grids. *Journal of Computational Physics*, 272:227–244, 2014.

[74] Bharti R. P., Chhabra R.P., and Eswaran V. Steady flow of power law fluids across a circular cylinder. *The Canadian Journal of Chemical Engineering*, 84:406–421, 2006.

[75] Ding H., Shu C., Yeo K.S., and Xu D. Simulation of incompressible viscous flows past a circular cylinder by hybrid FD scheme meshless least square-based finite difference method. *Computer Methods in Applied Mechanics and Engineering*, 193:727–744, 2004.

[76] Panda S.K. and Chhabra R.P. Laminar flow of power-law fluids past a rotating cylinder. *Journal of Non-Newtonian Fluid Mechanics*, 165:1442–1461, 2010.

[77] Paramane S.B. and Sharma A. Numerical investigation of heat and fluid flow across a rotating circular cylinder maintained at constant temperature in 2-D lam-

inar flow regime. *International Journal of Heat and Mass Transfer*, 52:3205–3216, 2009.

[78] Fallah K., Khayat M., Borghei M.H., Ghaderi A., and Fattahi E. Multiple-relaxation-time lattice Boltzmann simulation of non-Newtonian flows past a rotating circular cylinder. *Journal of Non-Newtonian Fluid Mechanics*, 177-178:1–14, 2012.

[79] Patel Jitendra Kumar and Natarajan Ganesh. A generic framework for design of interface capturing schemes for multi-fluid flows. *Computers & Fluids*, 106:108–118, 2015.

[80] Zhang X., Ni S., and He G. A pressure-correction method and its applications on an unstructured Chemera grid. *Computers and Fluids*, 37:993–1010, 2008.

[81] Lee T. S., Wei L., and Low H. T. Numerical simulation of turbulent flow through series stenoses. *International Journal of Numerical Methods in Fluids*, 42:717–740, 2003.

[82] Rouleau L., Farcas M., Tardif J. C., Mongrain R., and Leask R. L. Endothelial cell morphologic response to asymmetric stenosis hemodynamics: effects of spatial wall shear stress gradients. *Journal of Biomechanical Engineering*, 132: 081013:1–10, 2010.

[83] Fry D.L. Acute vascular endothelial changes associated with increased blood velocity gradients. *Circulation Research*, 22:165–197, 1968.

[84] Giddens D.P., Zarins C.K., and Glagov S. The role of fluid mechanics in the localization and detection of atherosclerosis. *Journal of Biomechanical Engineering*, 115:588–594, 1993.

[85] Lindegaard Karl-Fredrik, Grolimund Peter, Aaslid Rune, and Nornes Helge. Evaluation of cerebral avm's using transcranial doppler ultrasound. *Journal of neurosurgery*, 65(3):335–344, 1986.

[86] Bellner Johan, Romner Bertil, Reinstrup Peter, Kristiansson Karl-Axel, Ryding Erik, and Brandt Lennart. Transcranial doppler sonography pulsatility index (pi) reflects intracranial pressure (icp). *Surgical neurology*, 62(1):45–51, 2004.

[87] Tateshima Satoshi, Murayama Yuichi, Villablanca J Pablo, Morino Taku, Nomura Kiyoe, Tanishita Kazuo, and Viñuela Fernando. In vitro measurement of fluid-induced wall shear stress in unruptured cerebral aneurysms harboring blebs. *Stroke*, 34(1):187–192, 2003.

List of publications

Journals

1. M. Basumatary, G. Natarajan, S.C. Mishra, Defect correction based velocity reconstruction for physically consistent simulations of non-Newtonian flows on unstructured grids, *Journal of Computational Physics*, 272, 227 - 244, 2014.

2. M. Basumatary, G. Natarajan, V. Kulkarni, An unstructured hybrid staggered/non-staggered finite volume framework for the simulations of non-Newtonian flows (*under preparation*).

Conferences

1. Basumatary M., Natarajan G., Mishra S.C., Assessment of pulsatile waveforms on the blood flow dynamics in intracranial aneurysm, *ICCMS2016, IIT Bombay, Mumbai India*, June 27-July 1, 2016.

2. M. Basumatary, G. Natarajan and S.C. Mishra, Role of intracranial aneurysm size on the hemodynamics: a computational investigation, *Sustainable Mechanical Engineering: Today and Beyond (SMETB), Tezpur University, India*, March 24-25, 2017.